Superconducting Current Leads under Pulsed Current Conditions

by

Tyler Hanzlik

A thesis submitted in partial fulfillment of

the requirements for the degree of:

Master of Science

(Mechanical Engineering)

at the

UNIVERSITY OF WISCONSIN – MADISON

2019

Approved by:

_____

Professor John Pfotenhauer Date

_____

Professor Gregory F. Nellis Date

_____

Professor Franklin Miller Date

ACKNOWLEDGEMENTS

I would like to thank Professor John Pfotenhauer, my primary advisor and committee chair for this opportunity. His guidance and confidence in me has helped make my two years here at Madison a rewarding experience. I would like to thank Professor Franklin Miller for his involvement in my project and willingness to help whenever I needed it. I would like to Professor Nellis for the opportunity to be involved in the Solar Energy Lab while serving as a teaching assistant. I would also like to thank these three professors for their aid in my learning these past two years as I have had classes with all three of them and it was a truly rewarding experience.

I would like to thank my Graduate student mentor Evan Sheehan for his hours spent working with me answering my questions and helping me set up lab equipment. I would like to thank all the students of the Solar Energy Lab for the collaboration we have shared and friendships we have developed over the past two years.

I would also like to thank my family and Kara for their love and support of my time and efforts here at the University of Wisconsin.

Contents

FIGURES

TABLES

ABSTRACT

The focus of the present report is to observe the electrical and thermal behavior of conduction-cooled superconducting current leads under pulsed-current conditions. The study will be used to develop a better understanding of normal zone propagation when pulsed currents are applied, and to design appropriate current leads for such applications.

In order to reduce the overall heat generation in the current leads, copper tubing was soldered in parallel to the superconducting side of a single layer of 2G HTS tape. Current travels through the 2G HTS tape for portions of the leads that are below the critical temperature. The leads are contained in an evacuated vessel with one end of the leads connected through a vacuum feed-thru, to a power source while the other end is connected to a copper plate attached to the cold finger of a cryo-cooler operating below 30K. The temperature distribution before power is applied is measured with an array of type E thermocouples, and compared to a calculated distribution via a numerical model. Compressed spring-contact voltage taps are installed along both current leads in 2.5 cm increments to measure voltage along the leads and maintain electrical contact under cryogenic temperatures.

Once the lead temperature distribution reaches steady state, pulsed DC current signals are supplied to the apparatus consisting of a rapid ramp up, hold, and ramp-down sequence followed by a zero-current relaxation time. The study explores the lead response as a function of ramp rates, current level, hold time, and relaxation time. Typical ramp rates and hold times are on the order of 100 A/s, and 2 seconds respectively. In all cases, normal zone development and

temperature profiles are measured as a function of time. Limits are identified based on thermal or voltage runaway conditions.

A transient 1-D numerical model was also developed to calculate the current lead temperature in space and time. The current lead is modeled using 30 nodes. The chosen parameters for cross sectional area, length, current profile, and boundary conditions are based on the experimental setup of an HTS SMES device at the University of Wisconsin - Madison, but can easily be altered to examine the performance under various conditions. Results of both the numerical model and the current lead experiment are analyzed and compared to develop a better understanding of the thermal and electrical properties of superconducting current leads under pulsed conditions. Finally, conclusions of pulsed mode compared to direct current mode are made. This project has been conducted because research looking at superconducting current leads under pulsed current conditions and operating parameters similar to the UW Madison SMES project architecture has not been found.

1. Introduction

1.1 Background

Electricity consumption in the United States is expected to continue to grow year over year through the year 2050. In 2017 17% of United States electricity generation came from renewables. State and federal government requirements and incentives are expected to continue to drive U.S. renewable energy consumption up through 2050 in an effort to reduce the use of fossil fuels. However, renewable energy sources such as solar and wind are time of day dependent and require load leveling which has resulted in a demand for reliable and efficient energy storage devices. Additionally, trends in expanding the use of electricity in all forms of transportation to reduce carbon emissions has further amplified the need for reliable energy storage solutions. Lithium-ion batteries have been a viable solution but have limitations that require them to be used in parallel with large capacitors to ensure power quality. For some energy storage applications requiring high charge and discharge rates along with high energy density, this is not the best solution [1].

1.2 SMES

The energy storage method known as SMES (Superconducting Magnetic Energy Storage) utilizes the enhanced properties of superconducting wire to store energy in the magnetic field of a coil. The storage concept exists based on the fact that current will continue to flow in a SMES magnet even after the voltage applied across it has been removed. The magnetic energy stored in a SMES device is defined by:

$$\mathrm{E} = \frac{1}{2} L I^2 \tag{1}$$

The Superconducting technology utilized in SMES allows for very high round trip efficiency, high cycling capability, rapid charge discharge rates, and high energy density. Cost and complexity have limited the use of SMES to research and development projects mostly, but as the cost and manufacturing process of 2G HTS (second generation high temperature superconducting) tapes continues to improve, and methods for minimizing cooling consumption progress, SMES devices of large scale may become economically practical while maintaining notable performance advantages in comparison to other energy storage devices. One prime candidate for large scale underground SMES storage is to provide power grid stability as the shift to renewables introduces more source variance and complexity. For the time being, SMES devices are still a strong candidate for applications where performance, reliability, and energy density are more critical than cost of manufacturing and are commercially available on small scale [2] [3].

1.3 Superconducting Wire

The SMES performance capabilities are attributed to the phenomena of superconductivity along with advancements in cryogenics. Superconductivity is achieved when the electrical resistivity of a material is zero while direct current is applied. This unique trait for a select group of materials is only achieved below a specific temperature. This temperature is known as the critical temperature or Tc and it varies depending on material, applied current, and the presence of external magnetic fields. The critical current density or Jc is the maximum amount of current a material can carry at the Tc. The critical field or Hc is the highest magnetic field a material can sustain for a given temperature and remain superconducting. These coupled superconducting parameters define the capabilities of any superconducting apparatus. The phenomenon of superconductivity only holds true for direct current. Alternating current applied to

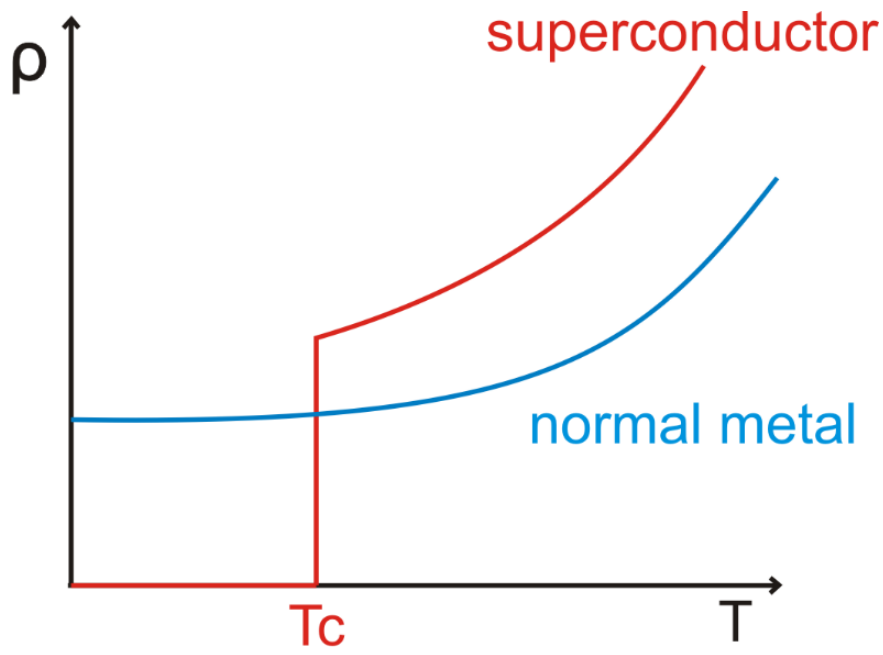

Figure 1: Diagram to represent the difference in electrical resistivity in a normal metal compared to the electric resistivity of a superconducting metal [54]

superconducting material produces AC loss which is comprised of eddy current and hysteresis losses, and these losses increase with increased frequency. Rose-Innes [4] explains that higher frequency causes photons of the electromagnetic field to have higher energy and excite some of the superconducting electrons into a higher energy state and behave as normal electrons. Low temperature superconductivity theory known as BCS theory explains that below the Tc, superconductor electrons form pairs known as cooper pairs. Electron interaction with the lattice results in opposite spin electrons to form pairs and resist interaction with the lattice allowing the pairs to follow each other resistance-less through the lattice. The theoretical basis for High Temperature superconductivity is still in progress and much of the associated understanding is defined primarily from experimental data. This has allowed HTS materials to be implemented in a variety of commercial and research applications. Manufacturing capabilities used in 2G HTS tapes such as flux pinning have helped superconductors become a more efficient method for transporting current and creating magnetic fields [5] [4].

1.4 Cooling

Superconductivity has been both a product and innovation driver for cryogenics since it was first discovered in 1911 [6]. If it was not for the discovery of liquid helium in 1908, superconductivity may never have been discovered. Similarly, without the discovery and development of high temperature superconductivity that began in 1986, the use of cryogenics and cryogenic equipment for transformers, motors, energy storage, and transportation cables would not be needed [6]. Sustaining temperatures for superconductors to operate reliably and effectively has been a driving force for cryogenic advancements including the effective use of cryogens and cryocoolers. To minimize the energy consumption of cooling methods, effective insulation from convection, conduction, and radiation are a top priority when operating superconducting devices. To insulate from convection, the superconducting component of the device is often contained in a vacuum container reducing the convection heat leak and limiting the heat transfer to that by the residual gas conduction associated with the given pressure and thermal radiation. MLI or multi-layer insulation sheets are used to minimize radiation heat transfer, and that amount is reduced by the factor of $1/(n+1)$ where n is the number of layers. Implementing a blanket of many sheets of MLI effectively reduces the radiation heat leak to a negligible value. The biggest obstacle for cooling that remains is the conduction of heat from the ambient region into the cryogenic region through the cables that are used to transmit power to the device. For most devices these are commonly known as the current leads [5] [7].

1.5 Current Leads

In most applications that require power to be transmitted from ambient temperature to a cryogenic environment containing a superconducting device, specifically designed current leads

are used. These current leads provide an electrical and mechanical connection across a large temperature gradient. They must be able to withstand the large stress due to the contraction and expansion associated with the large temperature changes during operation while conducting very little heat flux over the entire temperature range. For this reason, even when optimized, they can be a significant source of conductive heat leak into the cryogenic device. Current lead design and optimization can be very challenging and is critical to minimize the joule heating and conduction that occurs in the leads to prevent further heat leak into the cryogenic device. To minimize the joule heating, high current density 2G HTS tapes are electrically configured in parallel with traditional normal conductor current leads. Significant heat leak reductions can be made when HTS wire is used in the regions of the lead below the superconductor's critical temperature. As a result, the leads will not generate any joule heating in the portions of the lead that are below the Tc and thus superconducting. An example of incorporating HTS technology in leads can be found in CERN where over 1000 HTS leads supplying current ranging from 600 A to 13,000 A have been implemented [8]. The same current lead concept that utilizes 2G HTS capability can be implemented in powering devices such as a SMES, but it is critical that the leads be designed correctly given the device operating conditions to minimize the cooling costs of the device [5].

1.6 SMES at Madison

Research on Superconducting Magnetic Energy storage first began at the University of Wisconsin in the 1970's in the form of utility usage studies, component development, and system designs [9]. In a review of the 20 Year SMES program in 1990, Boom highlights the progress and describes the potential impact of a small scale SMES Unit [10]. The most recent SMES research at UW-Madison over the past decade has been focused on a high energy density SMES

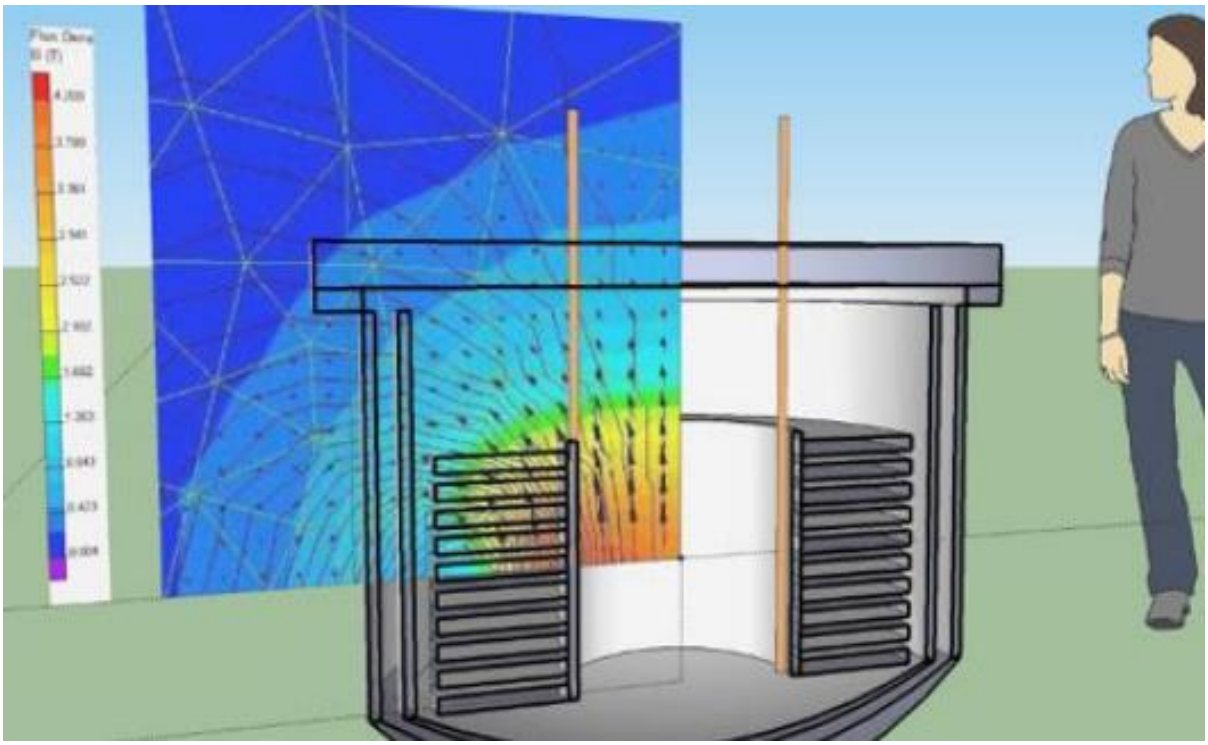

Figure: 2 Simulation and Scale of a 3 MJ SMES prototype for the UW SMES Research project [11] [12]

device prototype capable of rapid charge and discharge currents up to 600 A. The project goal is to produce a 3 MJ 1 MW device with a charge time of 1 second and discharge time of 5 seconds [11]. A magnet of this capacity requires a large quantity of commercially available 2G HTS tape assembled in multiple modular double-stacked pancake coils. The scale of this magnet can be seen in figure 2. [12] Given that each layer of the magnet requires hundreds of meters of 2G HTS tape, the anticipated cost of the device demands the highest level of protection from damage. The storage device itself involves no moving parts, but damages sustained from the loss of temperature control could be catastrophic. Additionally, the full scale device would operate for long periods of time resulting in a significant incentive to optimize the current leads to save on cooling costs over time.

1.7 Work in Current lead Design

1.7.1 Normal Conductor Current Leads

Current lead design began as soon as current transmission to cryogenic devices was first needed. Work on current lead design to minimize the heat influx using theoretical derivations was done by Richard McFee in 1957. McFee found that for copper leads, being sized off from the optimal wire diameter by a factor of two can result in a heat loss increase of over 100 percent [13]. Efferson introduced a novel concept for constructing optimized metal power leads utilizing the heat capacitance of Helium boil off in 1967 [14]. Work by Buyanov and Shebalin highlights design optimization for normal conductor current leads that operate under short term load conditions. They consider both demountable leads and leads where the ratio of length to cross sectional area is optimized keeping in mind the time duration of applied currents [15]. A review of current leads for cryogenic devices was done by Buyanov in which he highlighted the progress of lead optimization and construction of normal conductor current leads made up to 1975 [16]. A list of seven types of normal current leads was put together by Tada in 1984 [17]. Further fundamental descriptions of the optimization of normal conductor current leads can be found in Wilsons's "Superconducting Magnets" [18].

1.7.2 Superconducting Current Leads

Studies for implementing superconducting wire in current leads to minimize heat leak to a superconducting device are prevalent for constant load direct current scenarios and utilize different cooling methods and operating conditions. Ballarino mentions over a thousand Bi-2223 tape HTS leads being investigated for the Large Hadron Collider, under dc conditions using liquid and gaseous helium heat exchanger cooling, and Perin writes that during the

commissioning of the LHC system, more than 1300 current leads were implemented [19] [20] [21] [22]. James Hull discusses various lead design concepts for liquid helium temperatures and describes self-cooled HTS leads for constant current conditions and under different cooling circumstances [23]. Chang and Van Sciver write about the theoretical optimization of conduction cooled Binary superconducting current leads to minimize refrigerator power to the thermodynamic minimum [24]. A comprehensive summary on current leads suitable for high temperature superconducting devices done by Chen concluded with a need for more optimization work in increasing current density and reducing current lead thermal leakage for practical large scale HTS applications [25]. Bromberg, Michael, Minervini, and Miles discuss current lead design for DC distribution to minimize refrigeration power using multi-stage refrigeration methods. The paper highlights that refrigeration power consumption could potentially be reduced by ½ by optimizing a two stage current lead cooling method due to the fact that electrical power distribution is dominated by current lead losses [26]. A binary current lead design by Choi, Kim, and Yang consisting of a resistive and superconducting regions cooled by a two stage cryocooler was fabricated and tested revealing significant temperature rises and contact resistance at the joints which was decreased after shape modifications [27]. An optimization analysis of heat leak interception at the joint of helium cooled binary current leads was done by Yang and Pfotenhauer and reviled that the competing influence of cryocooler efficiencies and HTS material properties on helium requirements determined an optimum interception point between 70 and 80 K [28]. Hall writes that HTS current leads optimized in the normal state and then operated in the superconducting state can reduce the boil off by a factor of two according in comparison to normal operation. In an analysis of YBCO leads cooled by both conduction and liquid helium boil off, he goes on to explain that thermophysical data suggests

that the performance of Superconducting leads in the normal state is nearly as good as that of pure metals, generating only about 1.3 times the heat that the best normal conductor would [29]. Wu and Dederer designed and tested binary superconducting current leads that validated a 40% reduction in heat leak in comparison to conventionally designed current leads [30]. Binary current leads with varying cross sectional area along their length were numerically analyzed and designed to minimize heat leak to a SMES device by Wang and Jeong. The design was carried out and the leads were fabricated and tested effectively minimizing heat leak but requiring a complex fabrication process [31]. Gavrilin and Keilin found in their investigation of HTS leads with varying cross sectional area that heat removal at the joint between the HTS portion and normal conductor portion is only necessary during charging and discharging cycles as there is minimal boil off increase with the absence of intercept cooling [32]. In an HTS current lead design for Fusion applications, Isono and Kawano were able to reduce the required refrigeration power by 1/3 compared to a traditional lead design by using a binary HTS lead design [33]. Iwasa and Lee describe a method to design Superconducting Current leads that are purposefully operating in the current sharing mode in order to save on the required quantity of HTS materials compared to that needed for fully superconducting leads. It is found that leads designed in this configuration can provide savings in both material cost and cooling power requirements if the leads are properly optimized [34]. A novel current lead cooling method using the Peltier effect was investigated by Fujii who found that optimizing the current leads using this cooling method reduced the heat leak by over 50% and reduced the overall electric power consumption [35]. Additional details regarding both the CSV (Current Sharing Version) and FSV (fully Superconducting version) design methods can be found in Iwasa's book on superconducting magnets [5]. Iwasa also includes case studies on optimized copper and brass leads, as well as

various cooling methods including dry conduction cooled leads and helium vapor cooled leads. Iwasa also discusses binary leads with two stages of cooling and thermal anchoring highlighting the associated optimization, but provides no discussion of lead design for pulsed current conditions [5].

1.7.3 Current leads under pulsed conditions

Ballarino describes a method for sizing leads used in pulsed conditions in order to prevent them from overcooling. He explains that overcooling leads can result in ice development at the warm end along with wasted cooling energy. The pulsed mode analysis was carried out using a temperature dependent numerical simulation under various boundary conditions but with current values orders of magnitude larger than the research done on this project, and an experimental comparison to the model is not presented [20]. In another paper, Ballarino describes the optimization process used for both DC and pulsed leads cooled by helium gas. He explains that the operating conditions such as percent of current up time and down time of HTS leads play a factor in the optimization and that it is important to address the full range of excitation cycles when establishing final lead designs [36]. Park, Lee, and Kim describe an experiment on YBCO current leads operating at constant current with the use of a pulsed external heater to create a pulsed environment rather than pulsed current heat generation as used in this research [37]. Glowacki and Gilewski [38] describe their method and results for using pulsed current and pulsed fields to characterize critical parameters of HTS materials but not current leads specifically. Jeong and In [39] describe an investigation of helium gas cooled current leads operating in a pulsed mode of 30 second pulses of current. It was found that the transient numerical model analysis under pulsed conditions was more accurate than the model assuming steady state and perfect heat transfer. The work by Jeong and In is distinctively different from this paper because it deals with vapor-cooled normal leads rather than conduction cooled superconducting leads. In the Fusion project ITER, Wesche writes about an optimized binary current lead design that is both conduction and gas cooled and is intended to work under 70 kA pulsed operation [40] This work differs from the present research as it looks at binary

superconducting current leads rather than parallel, it looks at current pulses nearly 500 times larger, utilizes a different cooling method, and focuses on optimization.

In summary, extensive work has done on the design and optimization of current leads dating back to the early use of superconducting devices, and evidence for cooling power reduction from normal conductor lead optimization is prevalent. Research on current leads has also extended to designs utilizing 2G HTS tapes to further minimize generation in the operating regions of HTS leads as well as reduce the conduction using multi-stage cooling. Such leads have been generally constructed using the binary method where the superconducting region is thermally anchored to a cooling source at the junction with the normal conductor, and a design of the current sharing method using a normal and superconducting wire in parallel was also found. Optimizing current leads for specific pulsed operating conditions is less prevalent and in most cases leads are designed for steady state maximum DC current carrying scenarios. None have the uniqueness to investigate both Nodal and Temperature measurements the way this project has.

This research focuses on a model design to simulate unique SMES operating conditions and develops an experiment to validate the model. At the expense of slightly more conduction leak, the unique superconducting parallel design (instead of binary) allows a wider range of operating conditions while still maximizing the superconducting region of the lead rather than having a fixed location junction temperature. This method is a less complex with only 1 stage conduction cooling and is safer for protection of the superconducting portion of the lead to have a normal conductor alongside it. Additionally the research looks at the unique SMES operating conditions of rapid pulses of high current on the scale of seconds with longer down time.

1.8 Project Summary

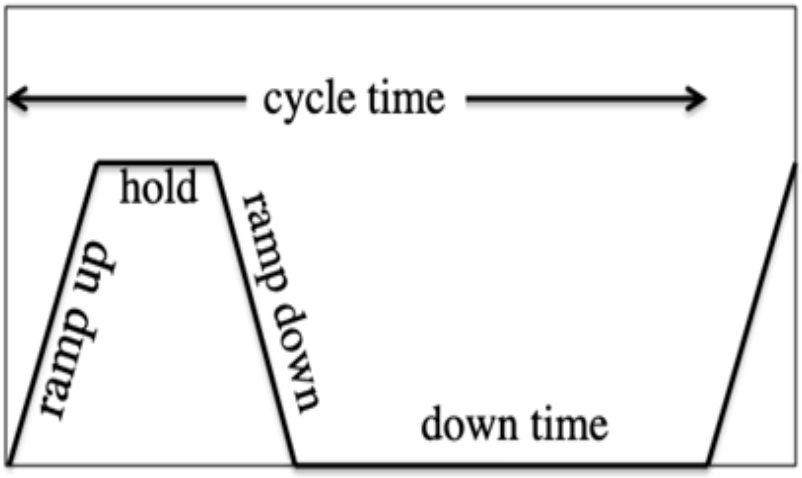

Figure 3: Depiction of pulsed current applied to current leads

The present research takes the approach of observing the thermal and electrical behavior of conduction cooled superconducting YBCO current leads under pulsed current conditions. The study experimentally analyzes the time dependent and spatially distributed temperatures and voltages of the current leads under pulsed conditions and compares these to a transient 1-D numerical model. Both experimental and modeling portions of the work were designed to simulate the parameterized behavior of the UW Madison HTS-SMES device. These parameters defined the testing conditions as well as the variables used in the numerical model. The SMES device requires pulsed current magnitudes between 100 and 500 A and charge-discharge rates between 1 and 5 seconds [11] [12]. In the experiment, a thermal steady state was first achieved before any current was applied. After reaching steady state, the ramp cycle displayed in Figure 3 was repeatedly applied until the temperatures approached a quasi-steady state condition or an unsafe limit. During the current cycle, joule heating occurs in the region of the lead where the temperature exceeds the current sharing temperature. The heat conducts along the lead raising the temperature and thus lowering the critical current across all locations of the lead and causing

the superconducting-to-normal transition zone to propagate towards the cold head. Such a phenomenon was observed for current values between 40 and 210 A and with different ramp duty cycles ranging from 10 to 30 seconds in duration. The ramp duty cycle is the sum of a ramp up duration, hold up duration, ramp down duration, and hold down duration. The scenarios were carried out experimentally in order to improve and validate the numerical model.

2. Computer Model

2.1 Overview

To simulate the current lead experiment, a 1-D transient numerical model was developed in EES (Engineering Equation Solver, F-chart Software). The model includes energy storage, left and right hand side conduction, radiation, and generation terms calculated using temperature dependent properties solved using the built in property function data stored in the EES property libraries [41]. Current lead geometries used in the model were the same as the dimensions used experimentally and will be defined for the model, and visually represented in the next chapter. Figures 30, 42, and 43 from chapter 3 may be helpful to visualize experiment components but are not included in this chapter in order to focus on the model itself.

2.2 Geometry and Boundary Conditions

The copper tubing used is 8 gauge conductor with a 3.2 mm outer diameter and 0.75 mm tube wall thickness. The designed lead length calculated to maximize the measurable superconducting region of the lead was 0.765 m. The heat capacitance of the superconducting

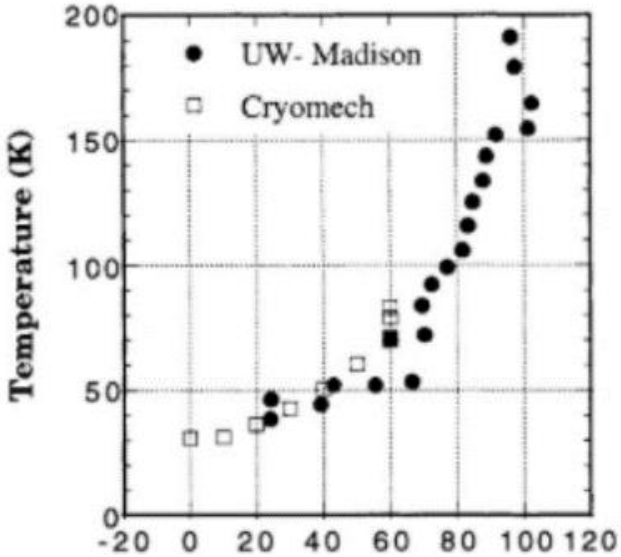

Figure 4: Cryocooler Cooling Power Curve of Refrigeration performance data from UW-Madison and Cryomech twin finger cryocooler [42]

wire is assumed negligible when compared to the copper portion of the lead. The most accurate boundary condition for the ambient side is found to be a finite conduction path of approximately 10 m through the 1/0 gauge insulated welding cables that connected to the terminals of the dewar rather than an infinite fin condition of the terminals (power cable connectors outside the vacuum vessel) exposed to natural convection. The cold end temperature boundary condition is defined by the cooling power curve of the cryocooler which was measured by both UW Madison and Cryomech and can be seen in Figure 4 [42]. The curve provides a corresponding cooling power with respect to temperature for approximately 30 different temperatures of the lower temperature operating range. The data was extrapolated to create a polynomial that served as the cold end boundary condition [42].

2.3 Model Functions

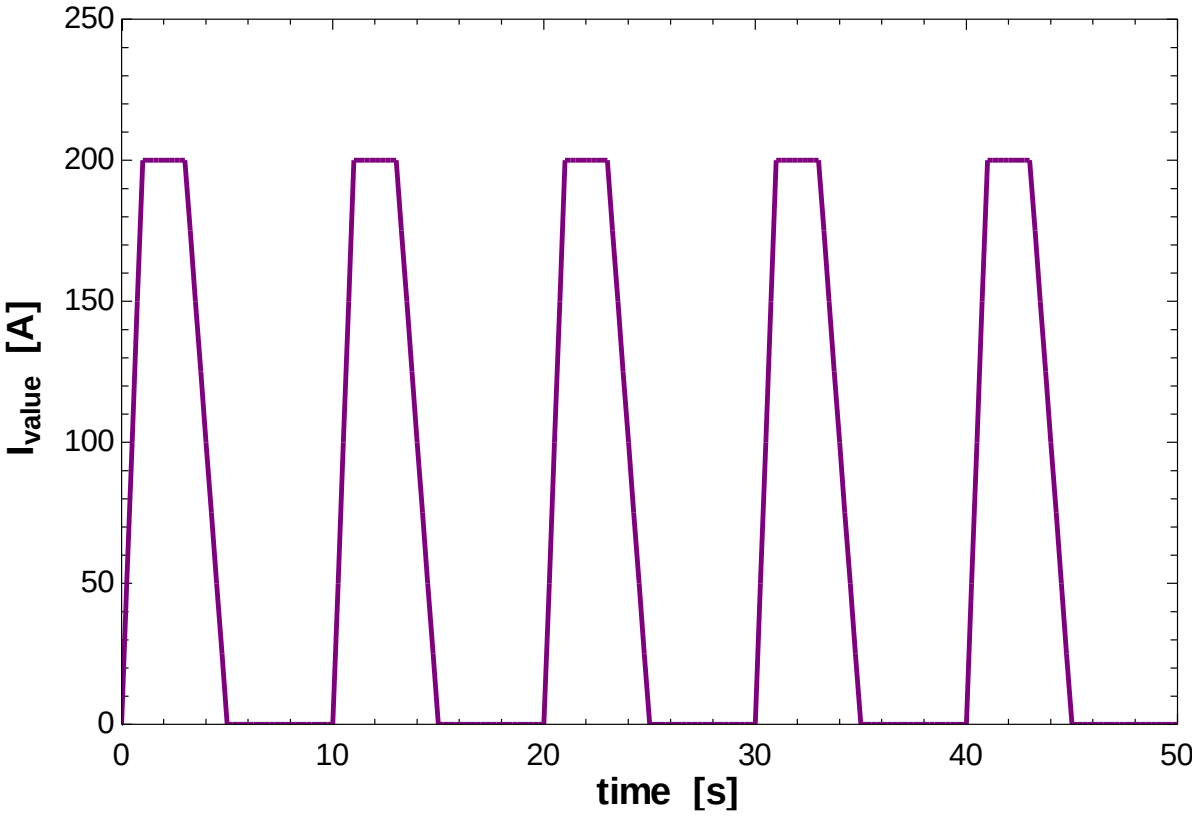

Figure 5: Current pulse signal for the transient numerical model

The computer model uses an “if” “else” function to generate the effective resistance of each node taking into account the superconducting region and the transition zone. The transition zone is graphically explain in figures 63 and 64 of chapter 4 and is the region of the lead where the temperature causes the critically current of the superconductor to be lower than the supplied current resulting in some current to travel in the superconductor, and some in the normal conductor. Another “if” “else” function is used to generate the adjustable current duty cycle similar to the one seen in Figure 5. The duty cycle can be altered in current amplitude, ramp up time, hold-on time, ramp down time, and hold-off time. The function outputs a current value dependent on the cycle time parameters. The current is equal to the minimum value during hold

off times, maximum value during hold on times, and the current is defined by equations 2 and 3 during ramp up and ramp down times:

$$\mathrm{I_{total}} = I_{min} + \left(\frac{cycleLocation}{rampUpTime}\right) * I_{max} \quad (2)$$

$$\mathrm{I_{total}} = I_{min} - \left(\frac{cycleLocation}{rampUpTime}\right) * I_{max} \quad (3)$$

The resistance function represented by equation 4 provides an effective resistance that is dependent on temperature and is used to determine the voltage at each node given the applied current.

The resistance of any nodes within the current sharing region is defined by Equation 4:

$$\mathrm{R} = \left(\frac{\rho_e \Delta x}{A_c}\right)\left(\frac{I_{total} - I_c}{I_{total}}\right) \quad (4)$$

Where the current traveling through the copper part of the lead in the current sharing temperature region is determined by I_{total} which is the current being supplied and I_c which is the critical current of the superconductor for the given position. The critical current is a temperature dependent value defined by a logarithmic function that is fit to data from the superconducting wire manufacturer which can be seen in Figure 6 and defined by [43]:

$$\mathrm{I_c} = -967.4 * \ln(T) + 4328.3 \quad (5)$$

The resistance of the lead nodes below the critical temperature is zero, and the resistance above the temperature of the current sharing region is defined by the temperature dependent resistivity of copper.

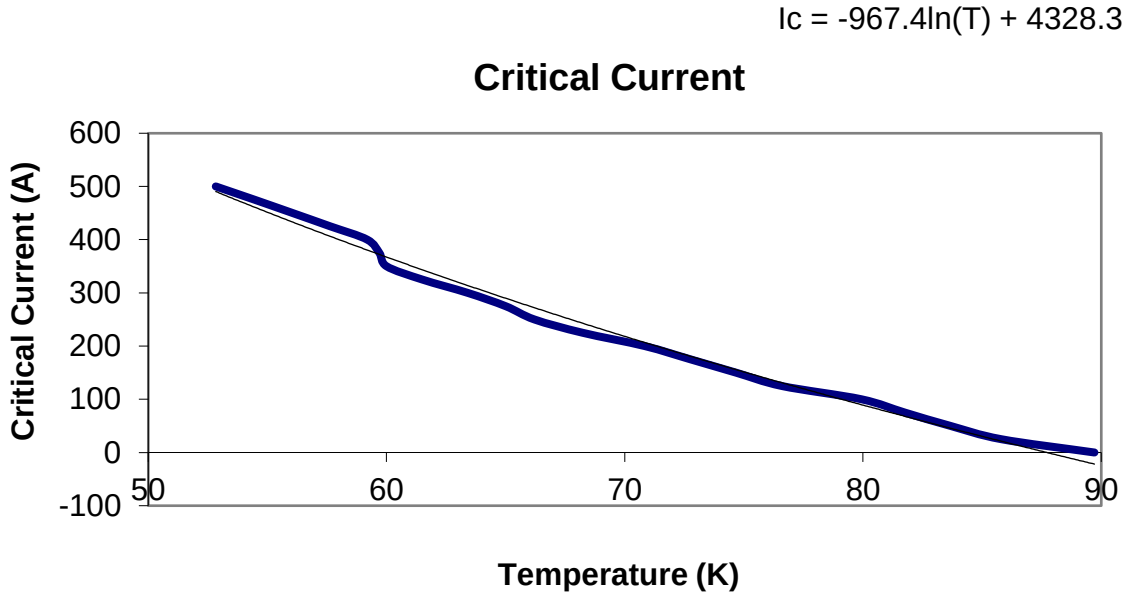

Figure 6: Logarithmic function fit (black) to 2G HTS Critical Current Data (blue)

Equation 4 reflects the fact that the superconductor carries the amount of current equal to its critical current at the given temperature, and any excess supplied current beyond the critical current is carried in the normal copper in parallel with the superconducting wire. Equation 4 scales the electrical resistant to make an effective electrical resistance based on the fraction of the total supplied current carried in the normal conductor. Any current traveling in the regions where the lead has turned completely normal has the normal resistance of copper for the given temperature, and any current traveling in a region of the lead that is fully superconducting contains zero electrical resistance and generates no heat.

These determined resistances are used in the model to then define the generation term (defined below) that is used in the equation of state to determine the temperature of any nodal position

during any point in time. A plot of the effective resistance as a function of position for the initial temperature distribution can be seen in **Error! Reference source not found.**.

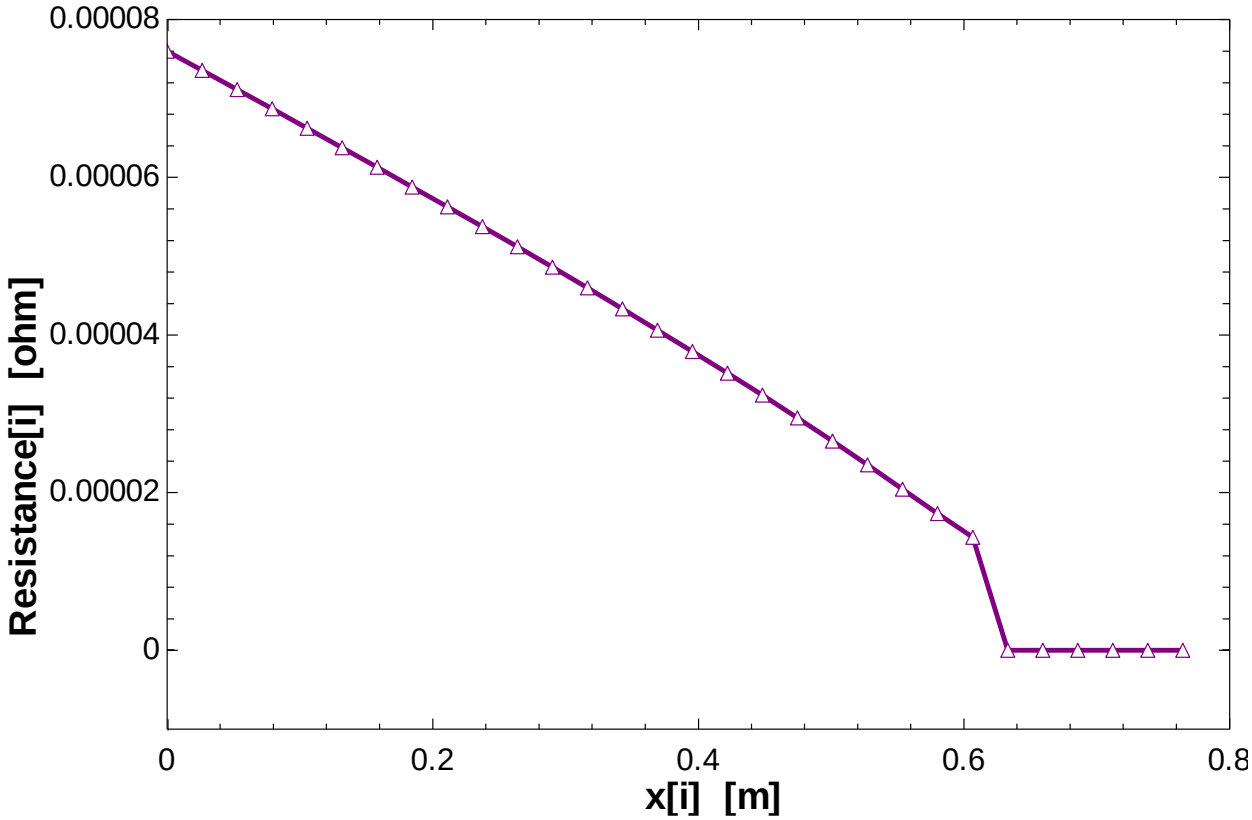

Figure 7: Plot of the temperature dependent resistance of the current leads with respect to position at initial temperature

2.4 Thermal Model

The thermal portion of the model begins with an energy balance of the selected control volume [44]. In order to have a reasonable computation time, the leads were split up into 30 of these control volumes. The energy balance for each control volume is coupled to the energy balance equations for the adjacent control volumes, and the boundary conditions that define the ends of the lead.

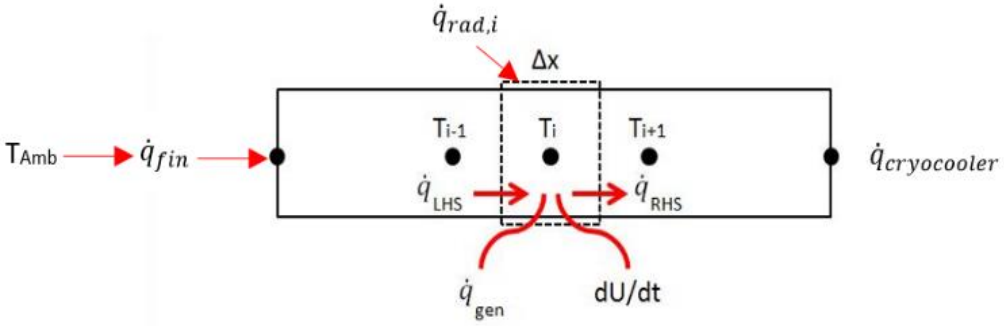

Figure 8: Schematic of the terms included in the nodal energy balance for an internal node

For each control volume, the terms considered are conduction, storage, generation, and radiation. A control volume is visually represented in Figure 8. The left and right-hand-side heat transfer terms are due to conduction from one node to the next and can be defined as equations 6 and 7:

$$\dot{q}_{LHS_i} = k_i A_c \frac{(T_{i-1} - T_i)}{\Delta x} \tag{6}$$

$$\dot{q}_{RHS_i} = k_i A_c \frac{(T_i - T_{i+1})}{\Delta x} \tag{7}$$

To calculate the radiation heat loss, an effective value was calculated to accommodate for the surface area of MLI (multi-layer insulation) sheets which provide insulation against radiation, and the surface area not covered by MLI. The term for effective radiation is defined by:

$$\dot{q}_{rad,i} = \sigma({T_{amb}}^4 - {T_i}^4)\left[\frac{A_{s,noMLI}\, e_4}{A_{s,Total}} + \frac{\frac{A_{s,MLI}}{A_{s,Total}}}{\frac{1}{e_1} + \frac{1}{e_2} - 1 + N_{Layers}\left(\frac{2}{e_3} - 1\right)}\right] \quad (8)$$

Where σ is the Stefan-Boltzmann constant and the effective emissivity is determined by the ratio of MLI to non-MLI surface area and corresponding emissivity values. The emissivity of the MLI surface area by the second term in the brackets of equation 8 where e_1 and e_2 are the emissivity of the outer and inner surface and e_3 is the effective emissivity of the MLI sheets. The value e_4 is the emissivity of the dewar wall, and the corresponding surface area is represented by $A_{s,no\ MLI}$.

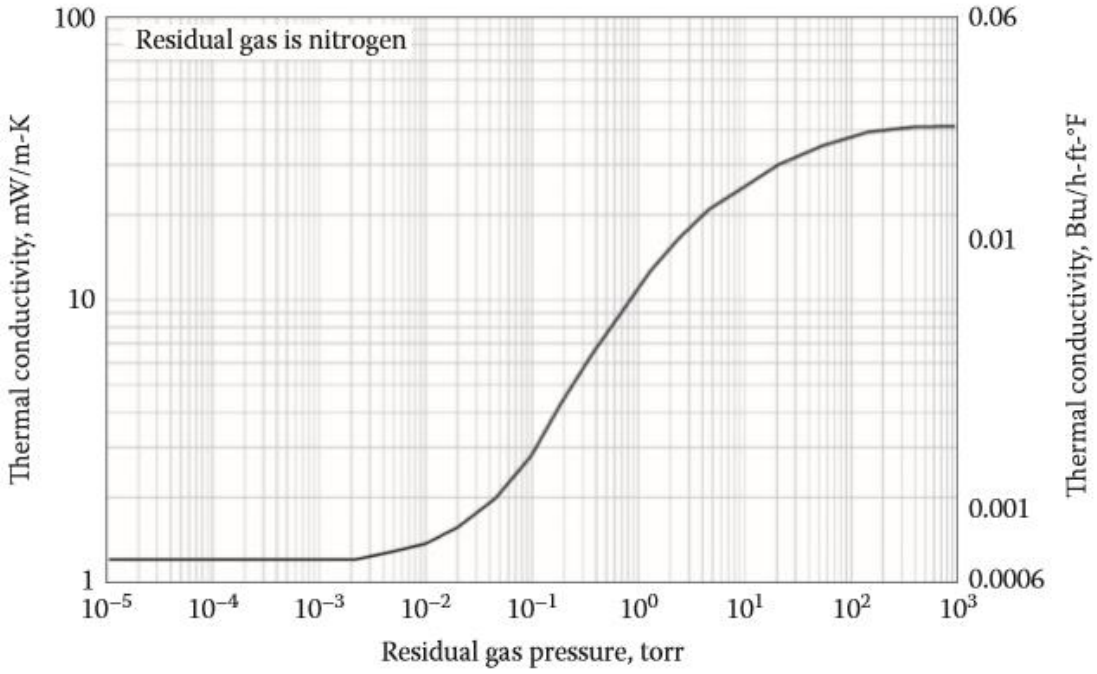

Figure 9: Mean apparent thermal conductivity with residual gas pressure for a typical MLI blanket. Layer density of 24 layers/cm and boundary temperatures of 300 K and 90.5 K [7]

This method was used rather than the effective thermal conductivity of MLI insulation for two reasons. The pressure sustained in the experiment of $1.4e^{-5}$ torr is at a value below the desired pressure resulting in the radiation to be the dominating mode of heat transfer in comparison to

conduction through the path and residual gas. Evidence of the apparent thermal conductivity with respect to residual gas pressure can be seen in figure 9. Additionally, because there are portions of the dewar not insulated with MLI, a model with some radiation leak due to these openings better represents the experiment and also agrees with the experimental data which will be shown later. A calculation was carried out as a second check using the MLI mean apparent thermal conductivity at 10^{-5} torr N_2 residual gas pressure to confirm that the values are negligible when compared to the lead conduction and the radiation through the openings. This calculation was done based on the mean apparent thermal conductivity associated with an MLI layer density of 20 layers per centimeter and a residual gas pressure of 10^{-5} torr.

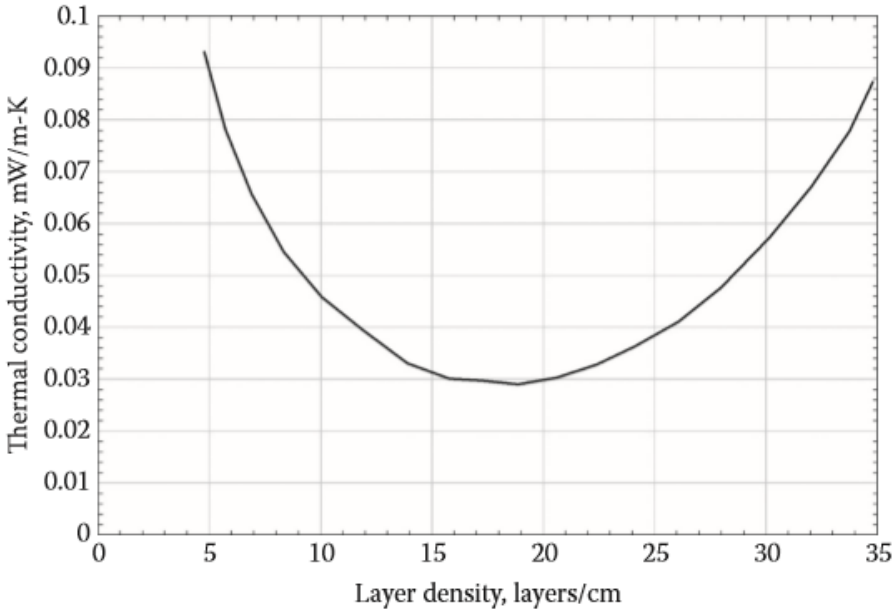

Figure 10: Variation of the mean apparent thermal conductivity of MLI layer density with boundary temperatures of 294 K and 78 K [7]

The optimal layer density is considered to be between 15 and 20/cm. A visual representation of this can be seen in figure 10 from Barron and Nellis [7]. The model agrees better with the measurements when it explicitly includes the portion of the cold surface not shielded by the MLI, as shown in equation 8.

The initial temperatures of the current lead nodes are defined by a balance between the boundary conditions and equations 6, 7, and 8 which leads to equation 9 for the middle nodes, and equations 10 representing the cold end boundary and 11 representing the warm end boundary:

$$0 = \frac{k_i A_c}{\Delta x}\left(T_{ini,i-1} - 2T_{ini,i} + T_{ini,i+1}\right) + \dot{q}_{rad,i} \qquad i = 2 \ldots (N-1) \tag{9}$$

$$\dot{q} = 2\left(\frac{\frac{(k_{30} + k_{29})}{2} 2A_c}{\Delta x}\left(T_{ini,29} - T_{ini,30}\right) + \dot{q}_{rad,30}\right) \tag{10}$$

$$0 = \frac{k_1 A_c}{\Delta x}\left(T_{c,ini,j} - 2T_{ini,1} + T_{ini,2}\right) + \dot{q}_{rad,1} + \dot{q}_{conv} \tag{11}$$

$T_{c,ini,i}$ connects the first node of the lead to the last node of a second series of nodes containing a finite conduction path to represent conduction through the power cables outside of the vacuum vessel. The nodes for the cable are exposed to natural convection and the first node of the cable was set to ambient temperature. The length of this power cable conduction path and its associated heat capacity was adjusted to match the behavior of the measured temperature at the warm end of the leads. Heat generated in the cables was ignored in the model because of their large cross-sectional area and to simplify the boundary as the cables were being used as a tuning parameter. Equations for the power cable can be found in the appendix.

The initial steady state temperature distribution without generation is calculated using equations 9, 10, and 11 along with the boundary conditions and can be seen in Figure 11:

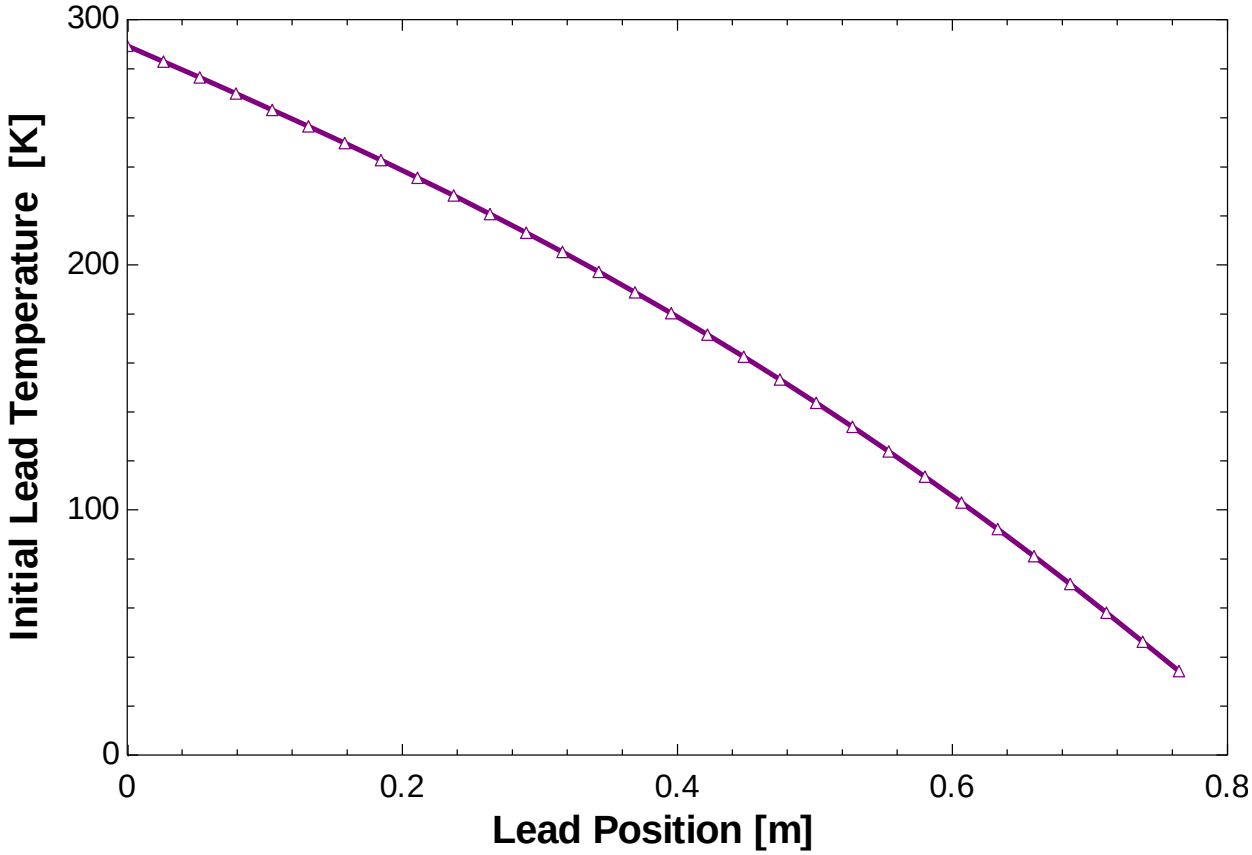

Figure 11: Initial Lead Temperature distribution vs Position

2.5 Terms for Transient conditions

The generation term for the control volume is defined simply by the magnitude of normal current squared traveling through the control volume multiplied by the temperature dependent resistance associated with equation 4. For $T > T_c$ the generated heat is represented as:

$$\dot{q}_{gen_i} = \frac{{I_{normal}}^2 \rho_{e_i} \Delta x}{A_c} \tag{12}$$

Where:

$$I_{normal} = I_{total} - I_c \tag{13}$$

Where $\rho_{e_i}$is the temperature dependent resistivity of copper at node i, Δx is the length of the control volume, Ac is the cross sectional area of the copper in the control volume, and I_{normal} is the magnitude of normal current passing through the copper.

The energy storage term is required for transient conditions because the thermal capacitance of the current leads as well as other components in the system effects the rate of change of the nodal temperatures with respect to time. The transient energy storage term $\frac{dU_i}{dt}$ is defined according to equation 14, where ρ_i is density, c_i is specific heat, and A_c is the lead cross sectional area.

$$\frac{dU_i}{dt} = A_c \Delta x \rho_i c_i \frac{dT_i}{dt} \tag{14}$$

Following the conservation of energy under transient conditions, the time rate of change of the stored energy equals the net heat flow into and out of the control volume plus the heat generation in the control volume. The energy balance equation in turn produces an equation for the nodal temperatures as a function of time. Equation 15 displays the energy balance for the middle nodes of the lead and is a result of combining equations 9, 12, and 14:

$$\frac{dT_i}{dt} = \left(\frac{1}{\rho_i c_i}\right)\left[\frac{k_i}{(\Delta x)^2}(T_{i-1} - 2T_i + T_{i+1}) + \frac{{I_{normal}}^2 \rho_{e_i}}{(A_c)^2}\right] + \frac{\dot{q}_{rad,i}}{A_c \Delta x \rho_i c_i} \qquad i = 2 \ldots (N-1) \tag{15}$$

Here k_i is thermal conductivity, I_{normal} is the normal zone current traveling through the lead, and ρ_e is the electrical resistivity. Similar equations balance the end nodes with the finite conduction model of the power supply cables at one end and the cold head cooling power at the other. These equations are defined in simplified form below as equations 16 and 17 which are a result of combining equations 9, 10, 11, and 12:

$$\frac{dT_1}{dt} = \left(\frac{1}{\Delta x(\rho_1 c_1 A_c + \rho_{steel} c_{steel} A_{c,steel})}\right) \frac{k_1 A_c}{\Delta x}(T_2 - 2T_1 + T_{c5}) + \frac{{I_{normal}}^2 \rho_{e_i}}{(A_c)^2} \quad (16)$$

The radiation term is left out of equation 16 because the change in temperature from the warm end to ambient is so small. The additional storage term identified with the subscript 'steel' is included in equation 16 to account for the electrically isolated thermal connection of the terminal interface to the dewar walls. The $-\dot{q}/2$ term is the cryocooler cooling power curve which is divided by 2 because only one of the cold fingers is used.

$$\frac{dT_N}{dt} = \left(\frac{1}{\Delta x \rho_N c_N A_c}\right)\left[\frac{-\dot{q}}{2} + \frac{\frac{(k_{30} + k_{29})}{2} 2A_c\left(T_{lead,29} - T_{lead,30}\right)}{\Delta x} + \frac{{I_{normal}}^2 \rho_{e_i}}{(A_c)^2} + \dot{q}_{rad,N}\right] \quad (17)$$

The full equations used in the numerical model can be found in the appendix.

In the transient model, the time dependent temperatures at each node are determined by integrating the temperature state equation through time and adding it to the initial temperature already calculated as seen in equation 18.

$$T_i = T_{ini_i} + \int_0^{t_{sim}} \frac{dT_i}{dt} \quad (18)$$

The EES model iterates until it converges on a consistent set of temperatures for all the nodes and does this for each time step. The result is an integral table providing temperatures and voltages for any of the nodal positions at any given time during the cycle. The current ramp cycle is generated and nodal temperatures are calculate which can be seen in Figure 12.

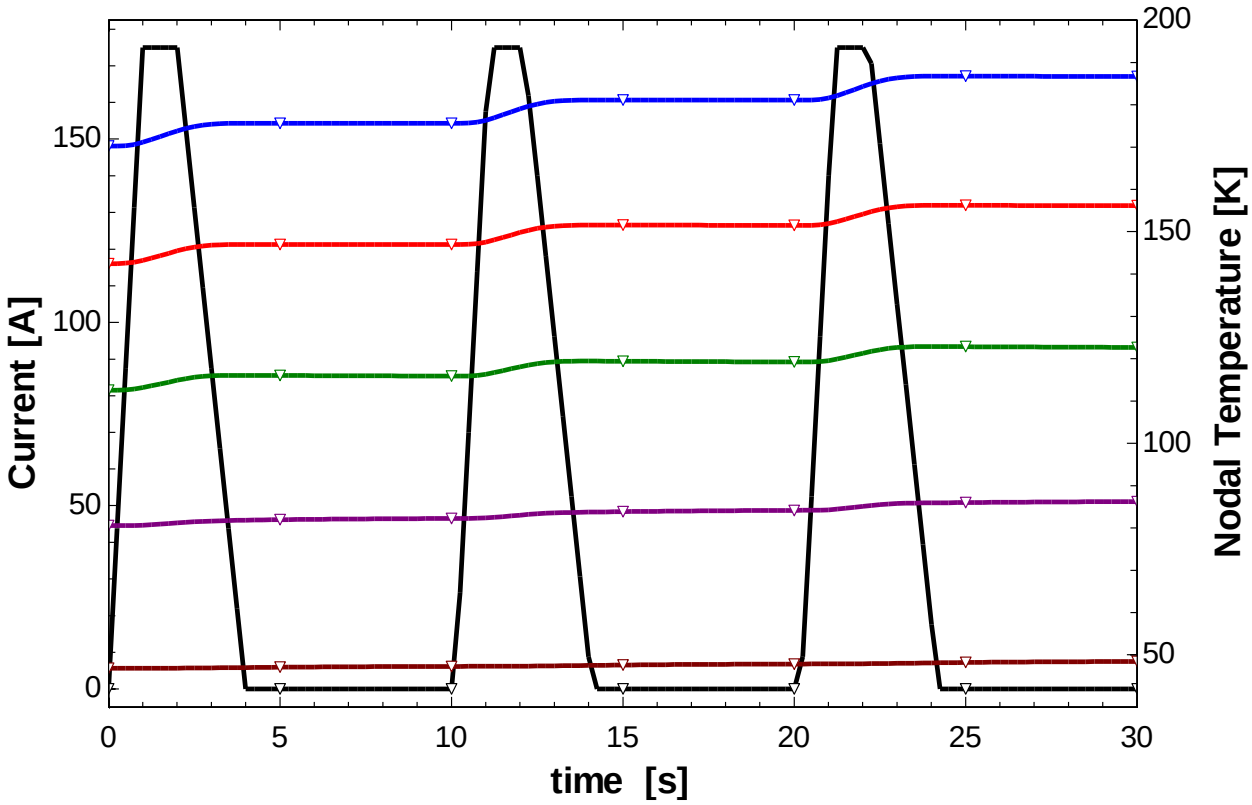

Figure 12: Nodal Temperatures of nodes 29, 27, 25, 23, and 21 for three 175 A current cycles consisting of 1 second ramp up, 1 second hold, 2 second ramp down, and 6 second hold off

2.6 RMS Current

The RMS current value of a pulse is calculated for comparison as current leads are most often designed based on a constant current value. RMS Current is calculated using trapezoidal waveform RMS method which breaks one trapezoidal pulse signal into two triangles and a

rectangle. Each portion is integrated and then the square-root of the sum of squares is calculated to find the RMS value of the trapezoidal waveform.

$$I_{RMS} = \sqrt{\frac{1}{T}\int_0^T I(t)^2 dt} \tag{19}$$

The trapezoidal wave form is split into 3 signals, for the duration of the ramp up:

$$I_1(t) = \frac{t}{t_1} * I_p \tag{20}$$

For the peak hold:

$$I_2(t) = I_p \tag{21}$$

And for the ramp down:

$$I_3(t) = I_p * \frac{t - t_3}{t_2 - t_3} \tag{22}$$

Where I_p is the peak current, t_1 is the time of ramp up, t_2 is the end of the peak hold, t_3 is the end of the ramp down, and t is the time before the next ramp up. The three portions of the signal are each then integrated and the square root of the sum of squares is applied to give the equation:

$$I_{RMS} = I_p sqrt\left(\frac{1}{t} * (t_2 - t_1 + \frac{t_3 - t_2 + t_1}{3}\right) \tag{23}$$

The results of this RMS method is later used for comparing pulsed current to constant current conditions.

2.7 Heat Leak

Additional heat transfer calculations were made independent of the transient model to confirm simplifications of the model. Included in these were calculations of residual gas conduction to confirm the heat leak is not significant. The leak for residual gas conduction was compared to that of radiation and confirmed that the radiation method selected for the model was adequate. Another series of calculations was carried out to determine the estimated conduction heat leak flowing through the instrumentation wire. The path of the wires is long and the cross sectional area extremely small, but with over 70 wires traveling into the cryogenic environment, this calculation was required to confirm that the associated heat transfer would be negligible. The leak of instrumentation wire was compared to the conducting of one control volume and was also found to be negligible.

Using the model, initial observations can be made to better predict the behavior of the leads under experimental conditions.

2.8 Model Insight

Prior to running the experiment, the model provided useful expectations for the experimental measurement. Looking at the thermal properties of the material we can see that towards the cryogenic region of the leads, the heat capacitence goes way down and the thermal conductivity goes way up. This observation suggetst that thermal disterbances will have a more significent impact in the cryogenic regions of the lead.

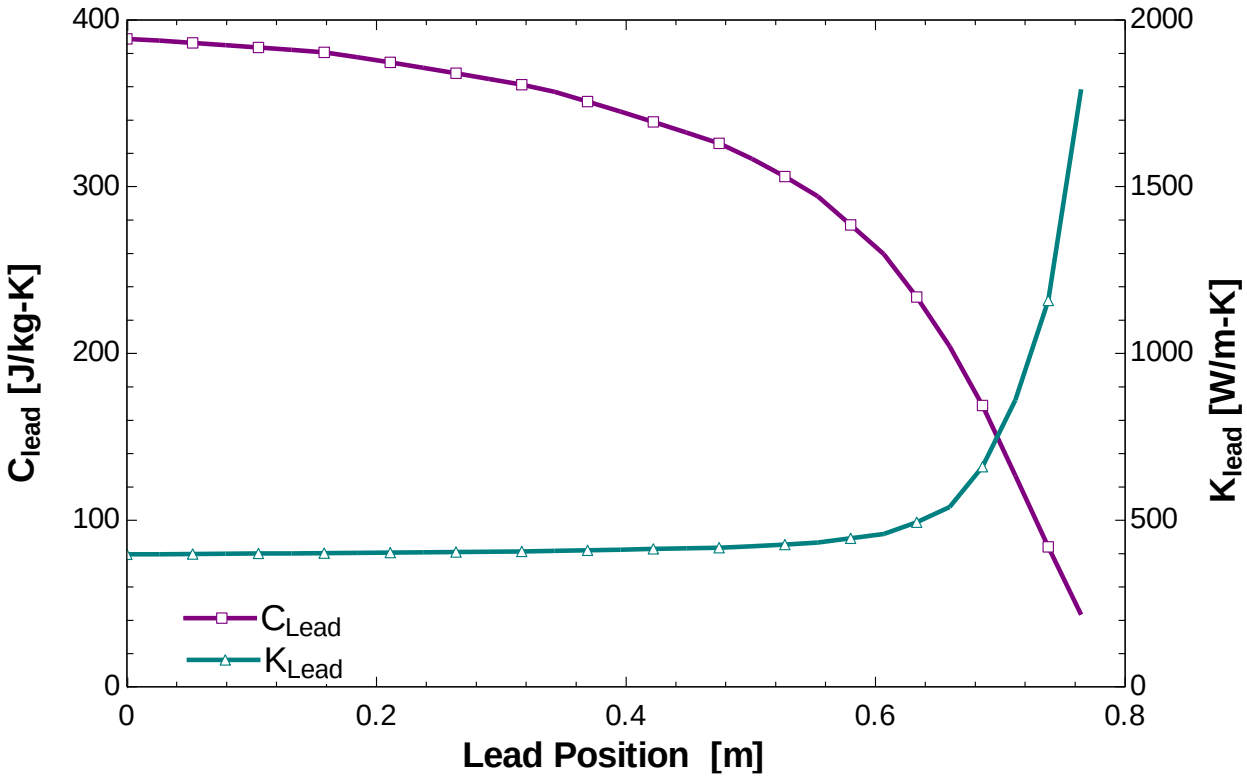

Figure 13 Temperature dependent properties of the current lead with respect to position.

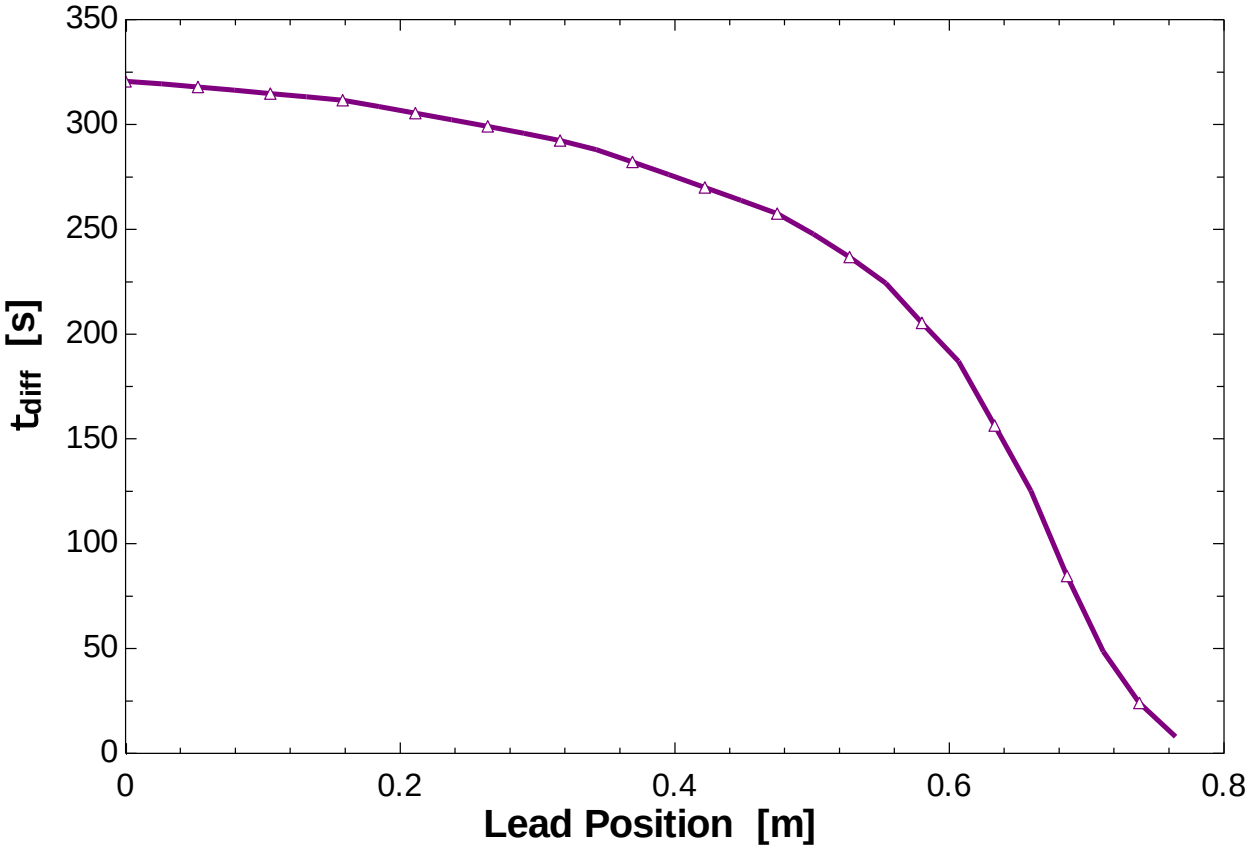

Figure 14: Diffuse time constant of the current lead as a function of position

The diffusive time constant was also estimated based on the associated temperatures for each node and the half the length of the lead as the body distance. Results can be seen in figure 14. This is an important observation from the model because it allows one to predict how long it takes the thermal wave from the heat generation to move along the lead. For example, figure 14 suggests that heat generated at the midpoint of the lead will take about 300 seconds to reach the cold finger of the cryocooler and raise its cooling power. A heat wave generated at the warm end of the lead moves more slowly. The thermal diffusion time constant may be estimated as:

$$\tau_{diffuse} = \frac{L^2}{4\alpha} \tag{24}$$

Where alpha is defined by:

$$\alpha = \frac{k}{\rho c} \tag{25}$$

It is often estimated that 90% of the heat thermal wave will have covered the distance after 3τ. The observation is important because it provides an idea of how much the delayed response by the cryocooler to the heat generated from one current pulse. The observation also provides an estimate of how long it might take before steady state temperatures are achieved – that is, when the cooling capacity of the cryocooler is equal to the heat generated from each pulse. This observation was very useful in determining the duration of time a given experiment should run for a given current cycle.

The model is also useful in being able to look at the transients of many different conditions. The model was used to estimate how long it would take for the current lead to reach quasi-steady state operating temperatures under various pulsed current conditions. It was used to get an idea of the temperatures the current lead would experience at the warm end as the experimental setup only provided temperatures measurements in the superconducting region of the lead and at the ambient boundary. This insight also help avoid running test conditions where the current leads might see dangerous temperature levels that could cause the indium solder connecting the superconducting wire to the copper tube to melt.

2.9 Transient Model

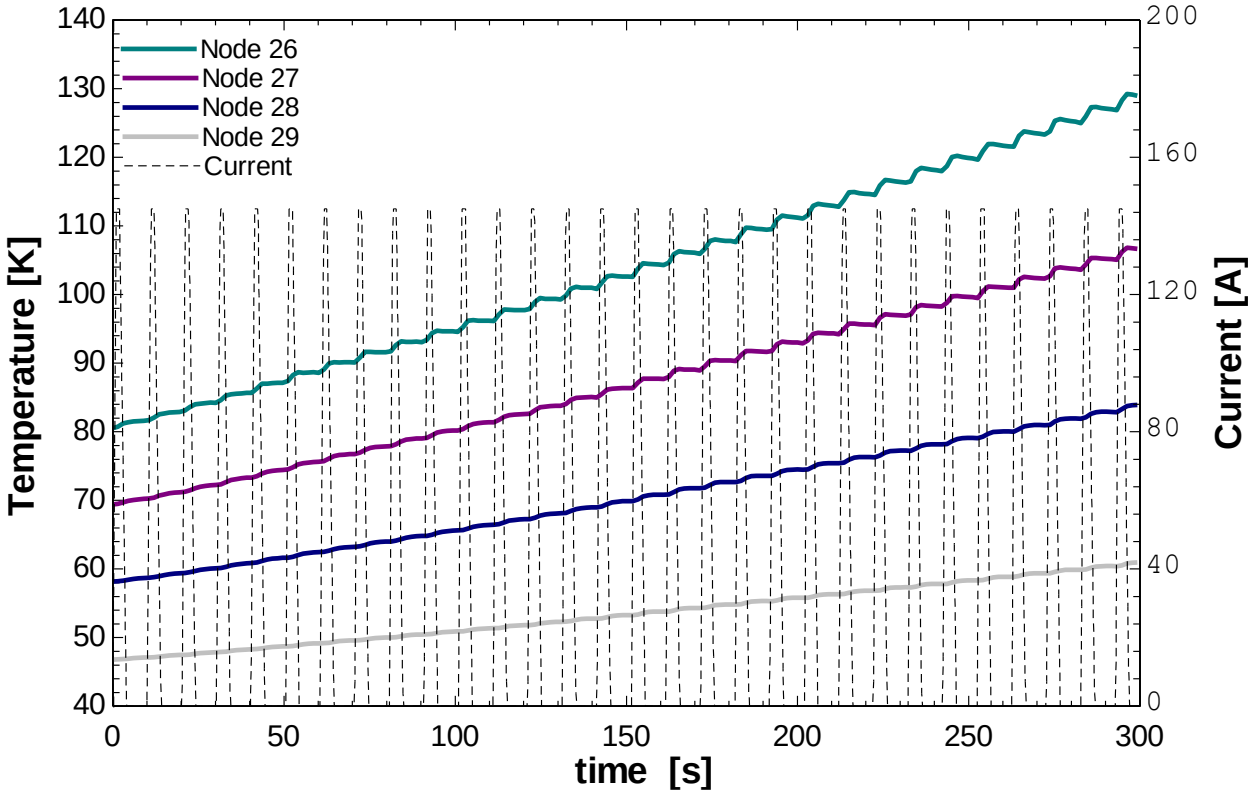

Figure 15: Cold end nodal temperatures of the superconducting current lead under 10 second current pulses of 145 A with a 1second ramp up, 1 second hold, 1 second ramp down, and 6 second no current hold

Looking at the temperatures of multiple nodes near the cold region of the leads under pulsed current conditions which can be seen in figure 15 reveals a steeper temperature increase for warmer nodes. Increased electrical resistance of Copper with increase in temperature results in the generation of more heat in the warmer region. Also notice that the bottom two nodes that are clearly in the superconducting region of the lead still increase in temperature. The warming is due to the thermal propagation of heat towards the cold finger of the cryocooler and is the primary reason that colder superconducting regions of the lead become warmer and turn normal.

The same feature can be observed from the voltages at a node that transitions from the superconducting to normal states. Figure 16 shows that a voltage does not appear at node 27

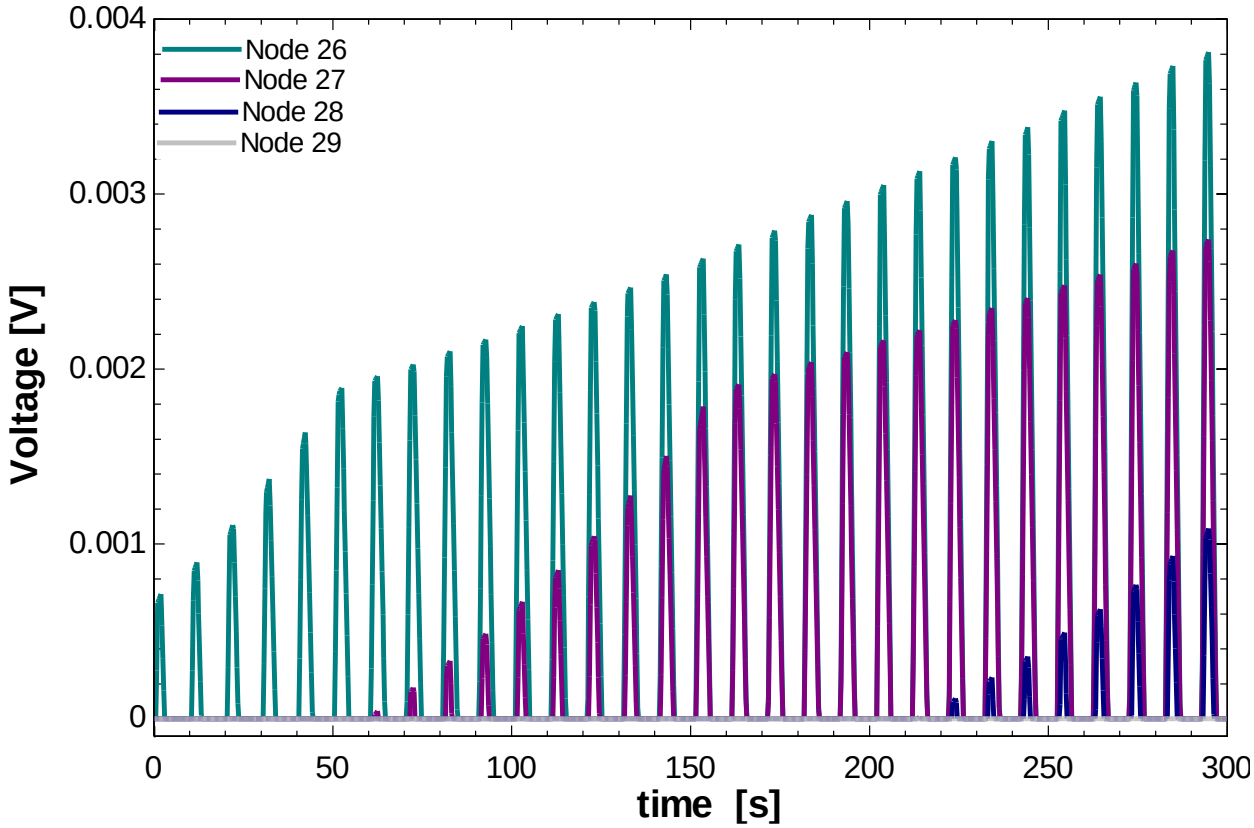

Figure 16: Nodal voltage values for the current lead near the superconducting region for a current cycle of 1 second ramp up, 1 second hold, 2 second ramp down, and 6 second hold off at 145 A

until around 60 seconds. Figure 15 displays the associated temperature data and reveals that the temperature at node 27 at 60 seconds is approximately 75 K. Not surprisingly, figure 6 reveals that the critical current at 75 K is 145 A. The pulse value of this simulation is 145 A, so it makes sense that this location would start turning normal at approximately 60 s. Figure 16 also displays the superconducting to normal transition for node 28 at around 225 s into the simulation. Revisiting figure 15 we can see that node 28 is approximately 75 K at 225 s.

Another interesting observation is the temperature distribution with respect to position at several different moments in time as seen in figure 17. Notice that nearly half of the temperature rise

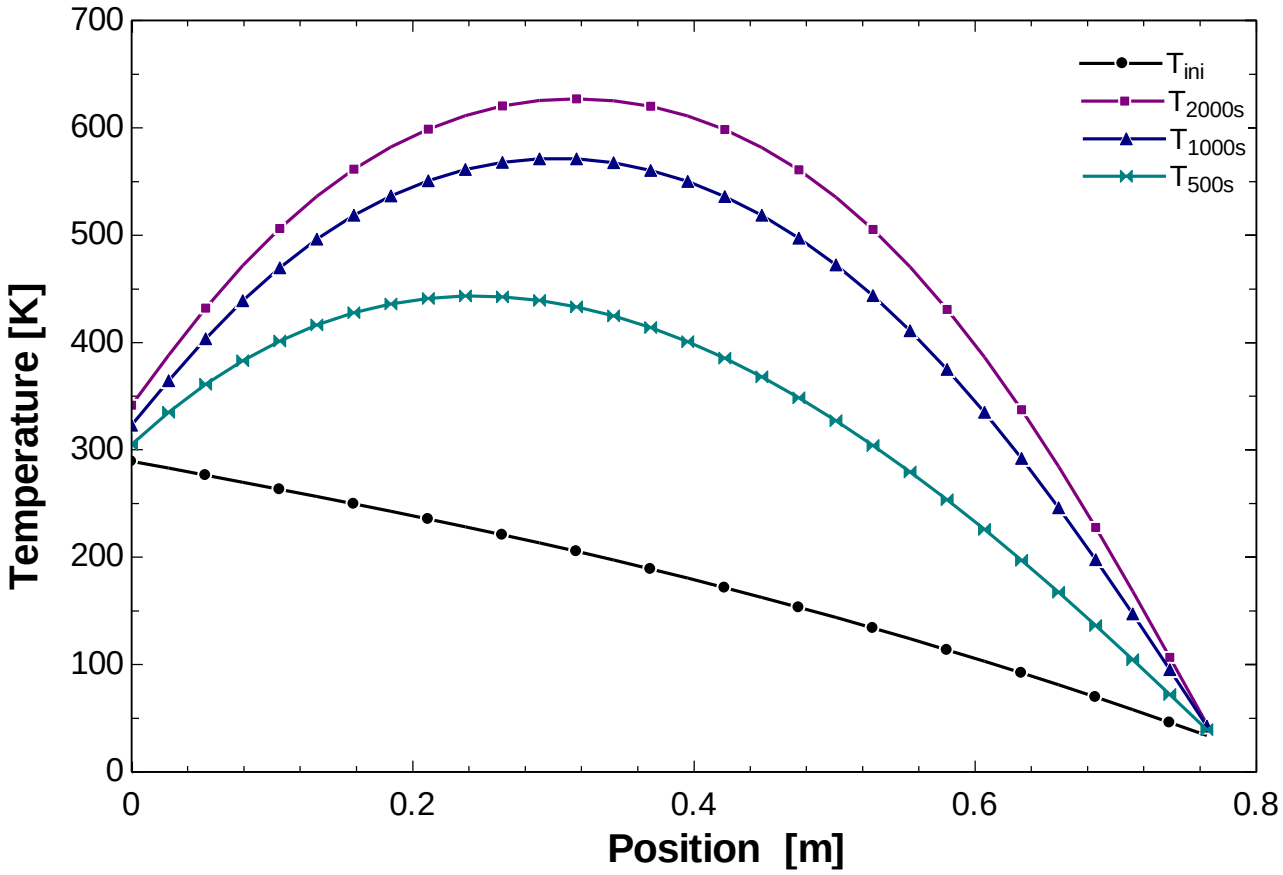

Figure 17: Temperature distribution of the lead for different moments in time under the same 145 A current pulse used in figures 15 and 16

generated in the warm end to move all the way to the cold end as discussed above. It can also be observed that the temperatures closest to the boundaries don't appear to move as much.

A close look at the temperature of the warm end and the cooling power of the cryocooler reveal that both boundaries of the current lead are rejecting heat. Additionally, thermal energy is being stored in the leads as evidenced by their increased temperature. A summary of these features is shown in figure 18. Notice both values appear to approach a plateau as the pulsed current simulation begins to approach a quasi-steady state operating condition, a result of the balance between the heat being rejected out both boundaries and the heat being generated due to ohmic losses in the leads.

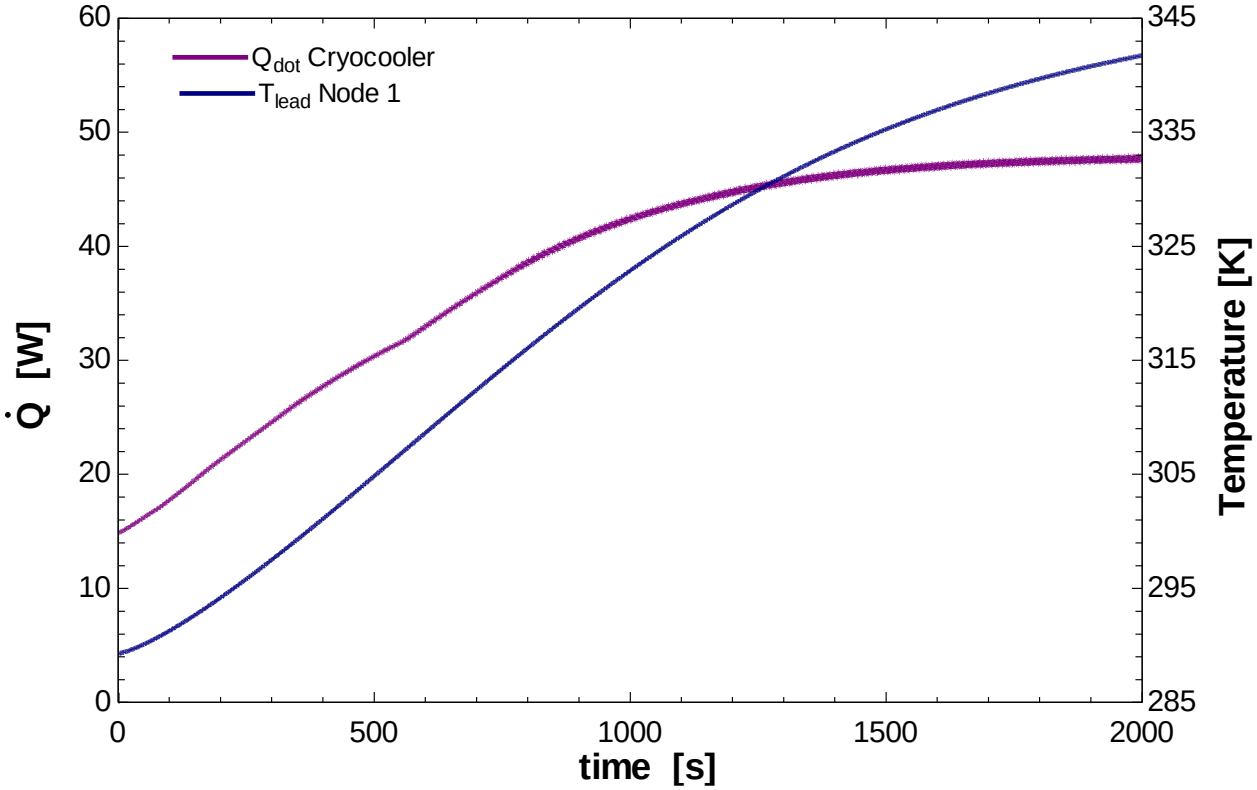

Figure 18: Heat rejection of the cryocooler and temperature at the warm end of the lead under the same 145 A pulsed conditions.

The Model can be used to determine the time it takes to reach thermal quasi steady state under various operating conditions. Although the diffusive time constant analysis using lumped material properties provides an order of magnitude description, a more accurate estimate of the time it takes to reach quasi-steady state operation can be determined using the full model.

Figure 19 presents a distribution of the nodal temperatures associated with the 145 A pulsed signal used in the previous figures. It would appear that the current leads reach quasi-steady state some time shortly after 2000 seconds of run time. Further investigations reveal that the 2000 second time frame is primarily dependent on the diffusive time constant and less on the operating conditions since it is consistent regardless of current magnitude and pulse type. This feature is due to the fact that the pulse cycle is on the scale of seconds while the time it takes for

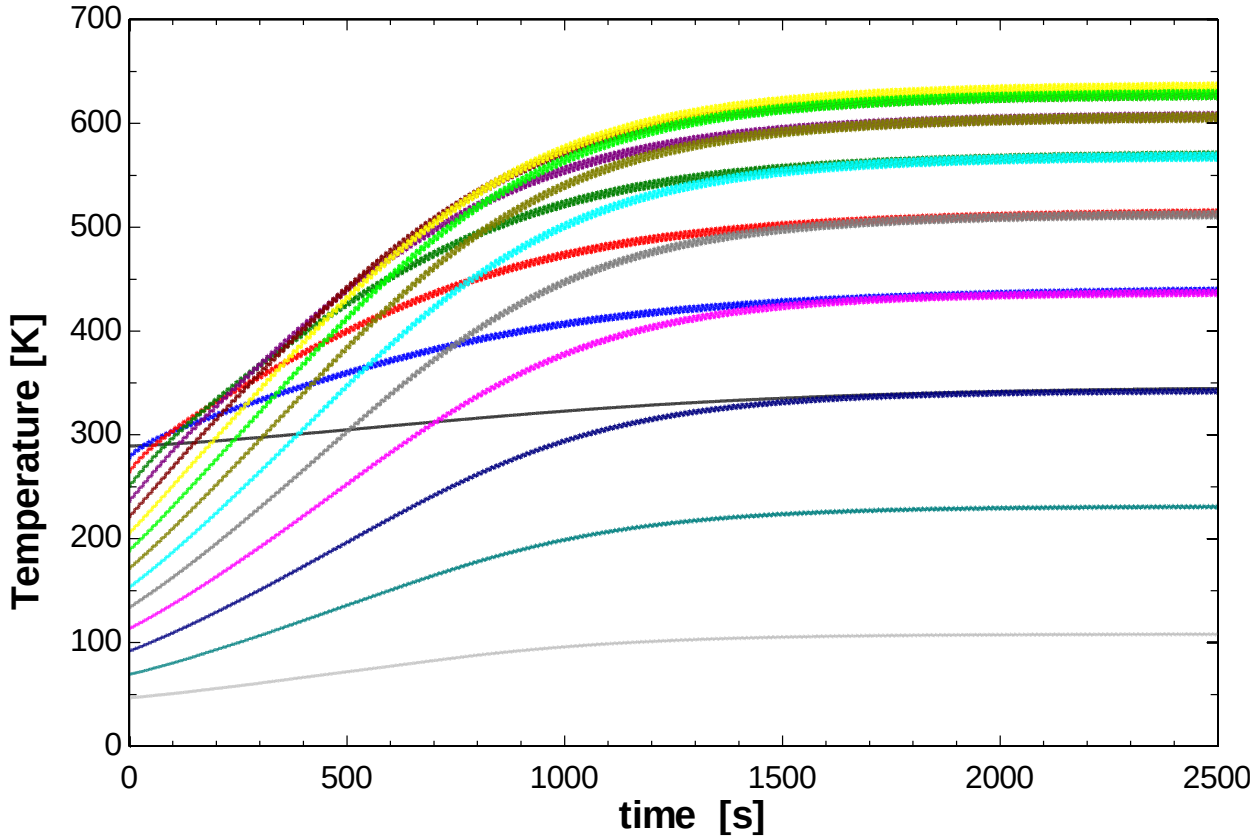

Figure 19: Nodal Temperatures of the current lead simulation under the same operating conditions as the previous figures

heat wave to cover half the distance of the lead is on the scale of 100's of seconds. For this reason it is suspected that the current leads under pulsed conditions might more easily be modeled as an RMS equivalent current.

A comparison of the current leads' response to a pulsed current mode is compared to their response to an equivalent RMS constant current mode in figure 20. Here 6 nodal positions are plotted for both a 200 A pulsed current cycle (1 second ramp up, 1 second hold time, 2 second ramp down, and 20 seconds at zero current) and the 63.25 A RMS equivalent value. From figure 20 it can be seen that the RMS equivalent current accurately captures the thermal behavior of the lead over the entirety of the simulation. However we can also see that each pulse produces slightly higher spikes in temperature that should be accounted for if attempting to simplify the

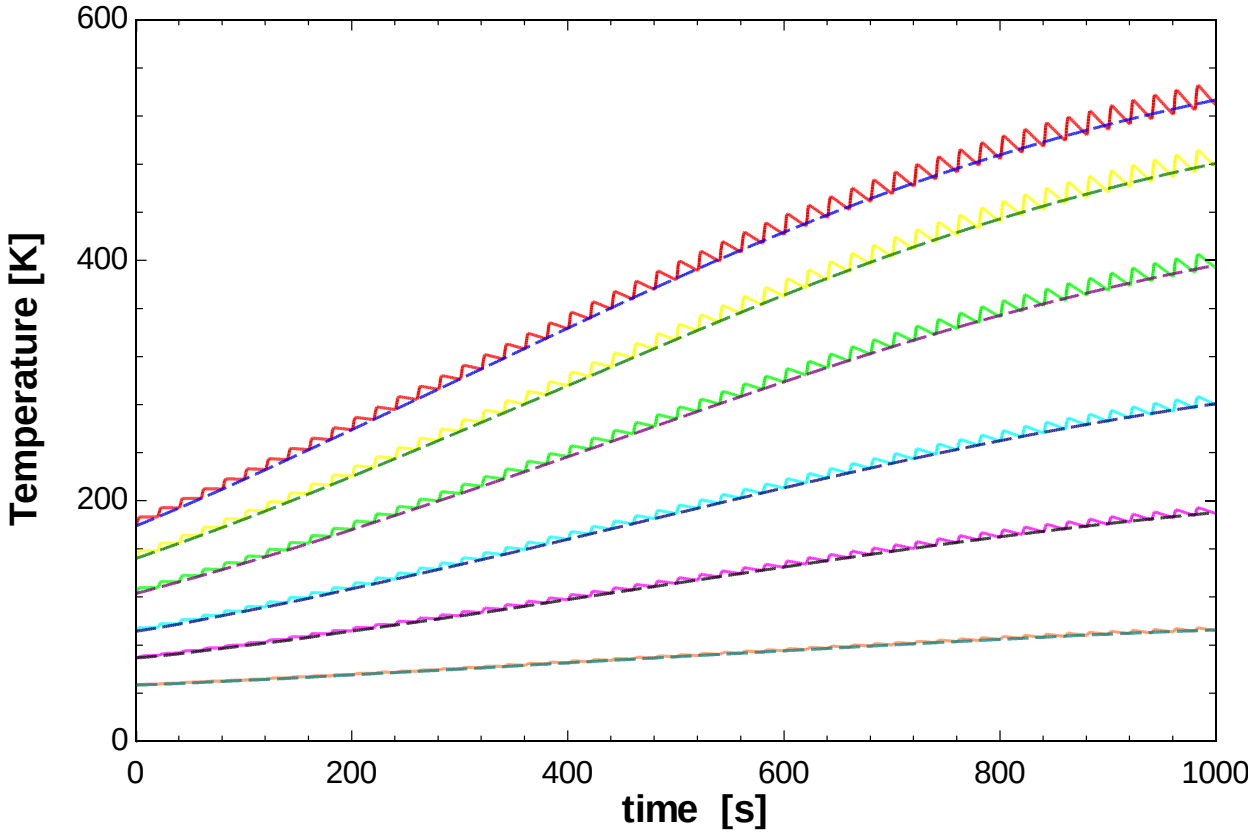

Figure 20: Multiple cold end nodes of 200 A pulsed current with a 10 second relaxation time and the RMS equivalent of 63.25 A overplayed for each node

current lead calculation. The RMS model would only be under-predicting the pulsed model by a few degrees in this operating condition, but when considering a condition with significantly more down time, the problem is amplified due to the fact that the heat generation is proportional to I^2 .

Figure 21 displays a current cycle where a 500 A pulse of current has a 1 second ramp up, one second hold, 2 second ramp down, and 100 seconds of down time between pulses. The figure clearly demonstrates that the model associated with an equivalent RMS current under-predicts the current lead temperatures by more than 100 K. This is a very important observation to

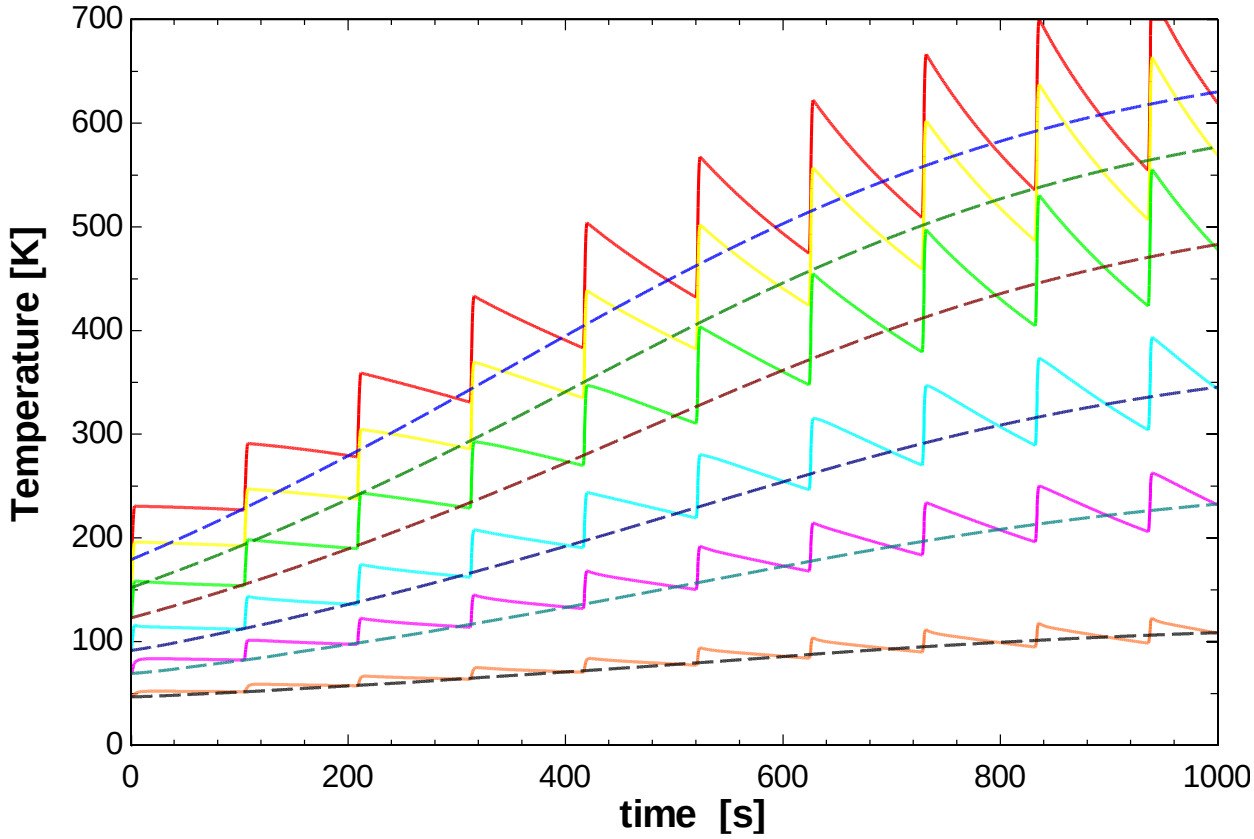

Figure 21: Multiple cold end nodes of 500 A pulsed current with a 1 with a 100 second relaxation time and the RMS equivalent of 69.34 A overplayed for each node

consider when designing current leads. In addition to minimizing the heat leak to the cryogenic environment, one must accurately predict the peak operating temperatures of the current leads in order to protect the cryogenic device.

Insight gained from the model provides a broad understanding of expected thermal behavior under pulsed current conditions. Hypothesis can also be made about the relationship between pulsed current and RMS equivalent constant current operating conditions. These observations were useful in designing the experiment that was used to simulate current leads operating on the UW-Madison SMES device, and that ultimately validated the transient numerical model.

Further details on the pulsed superconducting thermal model are provided in the appendix.

3. Experimental Setup

The present chapter covers details regarding the equipment used for data acquisition, instrumentation, cooling, evacuation, and supplying power to the experiment.

3.1 Data acquisition equipment

The experiments' data acquisition and power supply control was executed using National Instruments LabVIEW equipment. Figure 22 displays the National Instruments multi-module chassis configuration used to connect the sensor signals to the computer.

Figure 22: National Instruments SCXI Chassis

Slot	Module Number	Type
2	SCXI1100-SCXI1300 Terminal	12 Channel, 0-12mV Analog in, chassis ground
4	SCXI1100-SCXI1300 Terminal	20 Channel, 0-25mV Analog in, floating
7	SCXI1100-SCXI1300 Terminal	2 Channel, 0-1.5 V, 1 channel, 0-.3 V, 1 Channel, 0-1.8 V, Analog in, Chassis ground
Ext	NI USB-6008	1 channel, 0-2.5V Analog out

Table 1: Data Acquisition Module Information

A SCXI-1001 (Signal Conditioning Extension for Instrumentation) 12-module chassis was used to provide a low-noise environment for data acquisition of all the analog data inputs [45]. The SCXI-1001 can be seen in figure 22. Three SCXI-1100, 32-channel differential input multiplexer modules were interfaced with the SCXI chassis. The multiplexer module is designed specifically for signal conditioning of thermocouples, volt sources, and millivolt sources. Each module multiplexes the 32 input channels to a single channel for the data acquisition board. Separate modules were each used for thermocouples, voltage tap measurements, and silicon diode measurements. The temperature sensor for cold-junction compensation of thermocouples was used for thermocouple referencing. Jumper W3 was connected in the modules to implement a 10 kHz low-pass filter for signal conditioning of the high number of channels needed [46]. SCXI-1300 terminal blocks were used to interface with the SCXI 1100 modules. SCXI terminal

Figure 23: 32 Screw terminal SCXI1300 Terminal block used for nodal voltage measurements

blocks equipped with 32 screw terminal pairs to interact with module differential inputs allowed connection of all instrumentation wires for data acquisition.

The terminal blocks also provide a connection to ground and a temperature sensor used for thermocouple cold junction compensation [47]. An image of the 32 screw terminal SCXI 1300 Terminal block used for voltage measurements can be seen in figure 23.

3.2 Sensors

For data acquisition, 12 type E thermocouples, 20 copper wire voltage taps, two silicon diodes, and insulated copper wires for current sensing and control were used.

3.2.1 Thermocouples

Temperature measurements were critical for this experiment as it required high signal levels, high sensitivity, fast response times, minimal magnetic field effects, reasonable cost, ease of use, and small sensor size. For these reasons, type E thermocouples were chosen to measure the temperature profile on the leads. Thermocouples are smaller in size adding minimal thermal capacitances, and they also have rapid response times. They are also considered a logical choice when many sensors are required. Type E thermocouples have a magnetic field sensitivity of only 2% at 20 K. They are effective for capturing change in temperature across all temperature ranges down to about 20 K. Up to 5 % uncertainty in temperatures occurs between

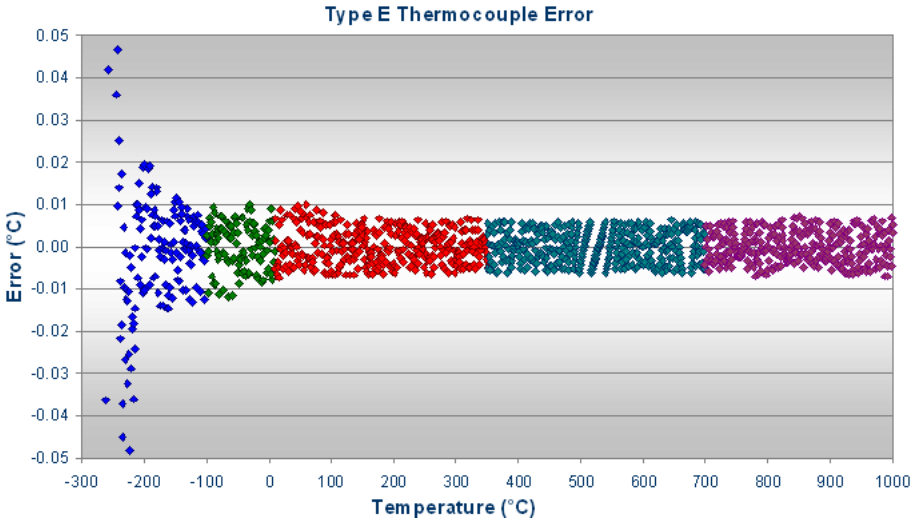

Figure 24: Type E Thermocouple error with respect to temperature [55]

approximately 20 K 60 K. . Evidence of this can be seen in figure 24. Fortunately the higher error region occurs below the critical temperature of the 2G HTS tape being used. Type E thermocouples were chosen in particular because they are the best suited thermocouple for low

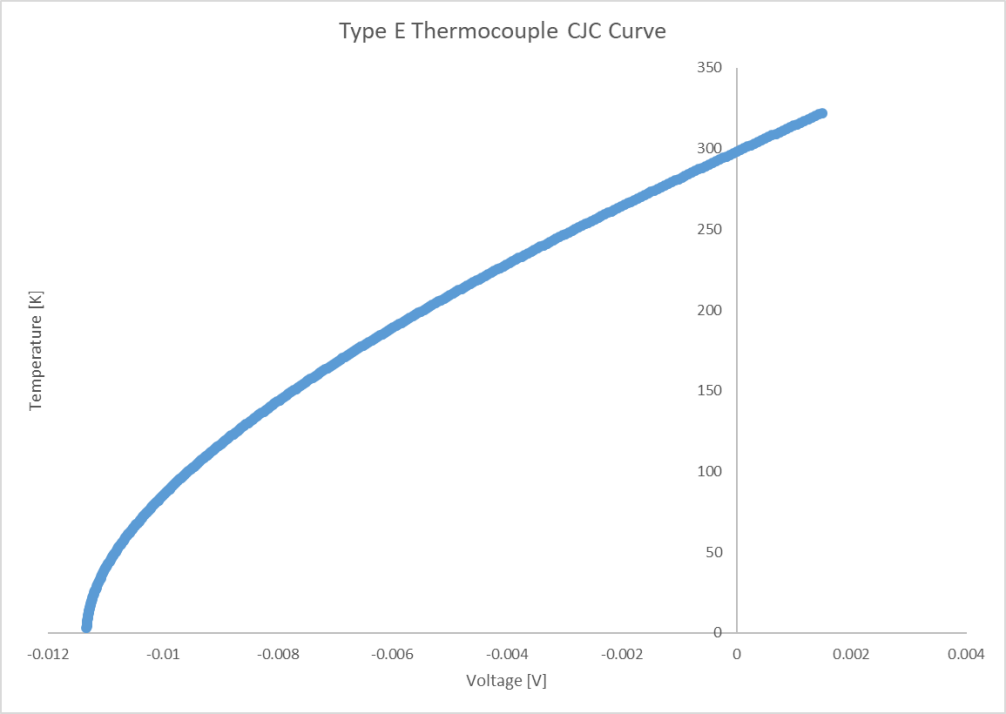

Figure 25: Type E Thermocouple reference table plot used to provide temperatures for corresponding voltage measurements

temperatures given they possess the greatest change in voltage per change in temperature of all the thermocouple types. The thermocouples were integrated with the SCXI1100-1300 terminal block and the voltage data was fit to an interpolated table from the type E omega thermocouple data sheet and then adjusted by the cold junction compensation reference temperature of 25 degrees C [48]. The resulting reference table plotted in figure 25 was entered in NIMAX and used as a reference source in LabVIEW. The thermocouples positive and negative leads were connected to CH+ and CH-, and CH- was then connected to CHSGND in a daisy-chain fashion with the other thermocouples per the user manual. The temperature nodes were approximately 2 inches apart.

Error Type	Magnitude
Human error from position measurement	+- 0.1 [in]
Instrumentation error due to CJC delta T between sensor and Chassis (sensor to terminal + chassis)	+- 1.3 [K] @ 25C 0.9 + 0.4 [K]
Field Sensitivity	2%
Measurement error	1-5%

Table 2: Factors considered in thermocouple error

3.2.2 Voltage Taps and other Instrumentation

To measure the spatially distributed voltage of the current leads, coated copper wires were bundled, twisted, and connected to specially fabricated twist-in spring-loaded voltage taps, described in detail below. Positive and negative voltage node leads were connected to CH+ and CH- locations on the SCXI-1300 respectively. The lines were not grounded but were floating to prevent any ground loop. Uncertainties in the voltage measurements are primarily due to the NI equipment resolution and uncertainties in position measurements. All the wires are insulated and shielded. The voltage nodes were approximately 2.54 cm apart.

Silicon diodes possess high measurement sensitivity but require an external current source. They are also not suitable for magnetic fields in low temperatures and are not as small as thermocouples therefore adding some heat capacitance effects to the temperature measurement. For these reasons a Lake Shore DT-470 silicon diode was only used to measure the temperature at the power terminal entrance of the vacuum vessel. A linear fit was created from the DT400 Series Expanded Temperature Response table found on the Lake Shore website for the anticipated temperature range of the terminals at the warm end [49]. A Lake Shore model 120

current source was used to provide an external current of 10 micro amps to the diode and the forward-bias voltage measured with separate voltage taps was used to determine the temperature.

Measuring the current applied to the current leads was accomplished by measuring the voltage across a 1 milliohm resistor located at room temperature and electrically connected in series with the current leads. The voltage leads across the resistor were connected to one of the SCXI modules with insulated instrumentation wire. A secondary current measurement for calibration was outputted on the power supply front panel using the current monitoring input analog connector that came standard with the power supply.

Count	Manufacturer	Type
12	Omega	Type E Thermocouples
20	Smith's Interconnects/In-house	Special Voltage Taps
1	Lake Shore	Silicon Diode

Table 3: Sensor Types, count, and Manufacture source

All instrumentation wiring was insulated, wound, or soldered and heat shrunk when necessary. Individual wire pairs were labeled and evaluated for continuity and proper ground connections

Figure 26: Rear view of the National Instruments SCXI Chassis with modules inserted and Instrumentation connected

were evaluated separately. All wires from the instrumentation inside the vacuum enclosure including the silicon diode, voltage probes, and type E thermocouple wires were routed via a hermetic feed-thru out of the vacuum enclosure and connected to the SCXI chassis as seen in figure 26. More images of the measurment instrumentation used in the experiment can be found in the appendix.

3.3 LabVIEW

National Instruments LabVIEW programming was used for controlling and recording all temperatures, voltages, and currents. A front panel was used to give real time data charts and values while the program also stored and auto saved all instrumentation data to be accessed for subsequent data processing with Matlab. The front panel for control and data storage can be seen in figure 27.

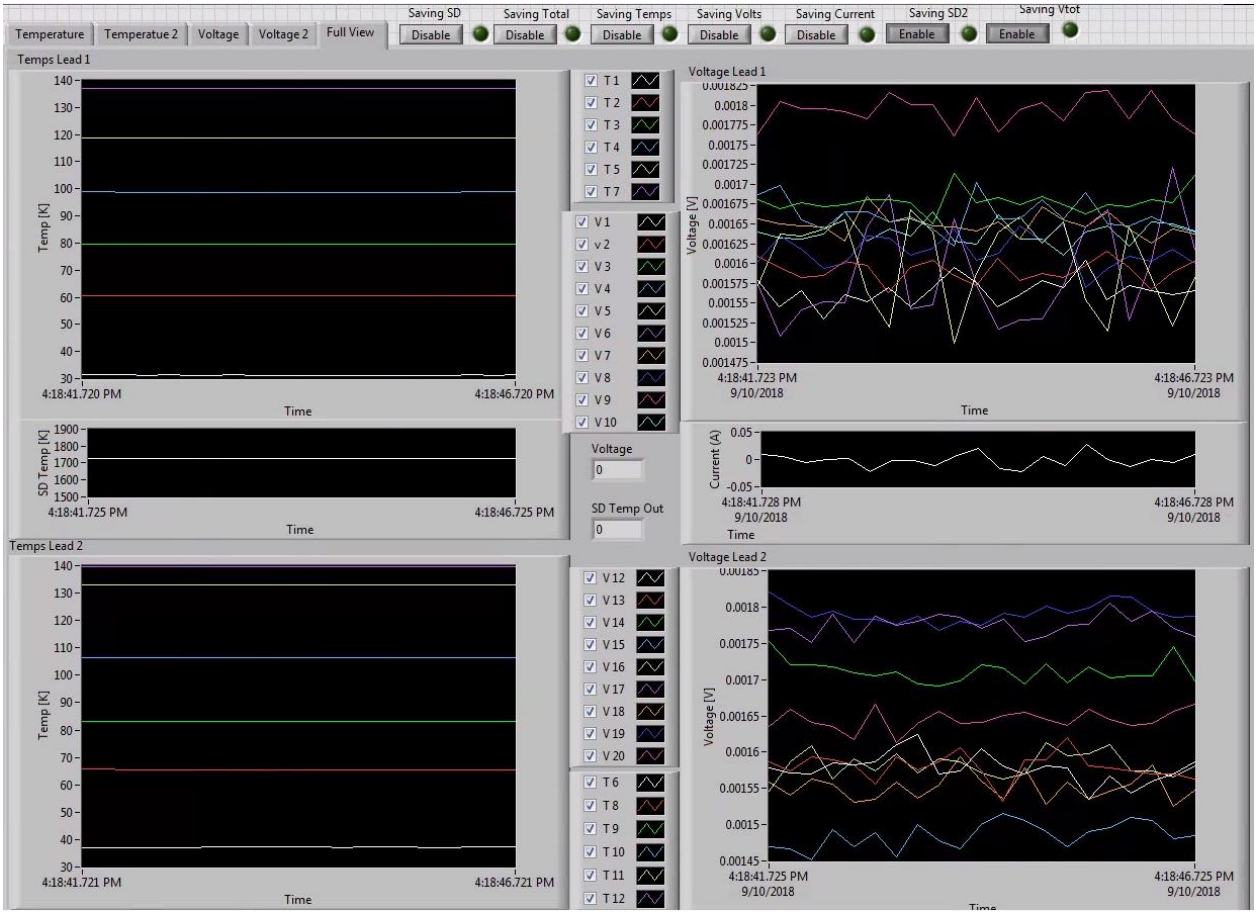

Figure 27: Image of the National Instruments LabVIEW instrumentation panel for real time measurement observation

The block diagrams for the data collection, storage, and control can be seen in figures 28 and 29. These were both built in National Instruments LabVIEW.

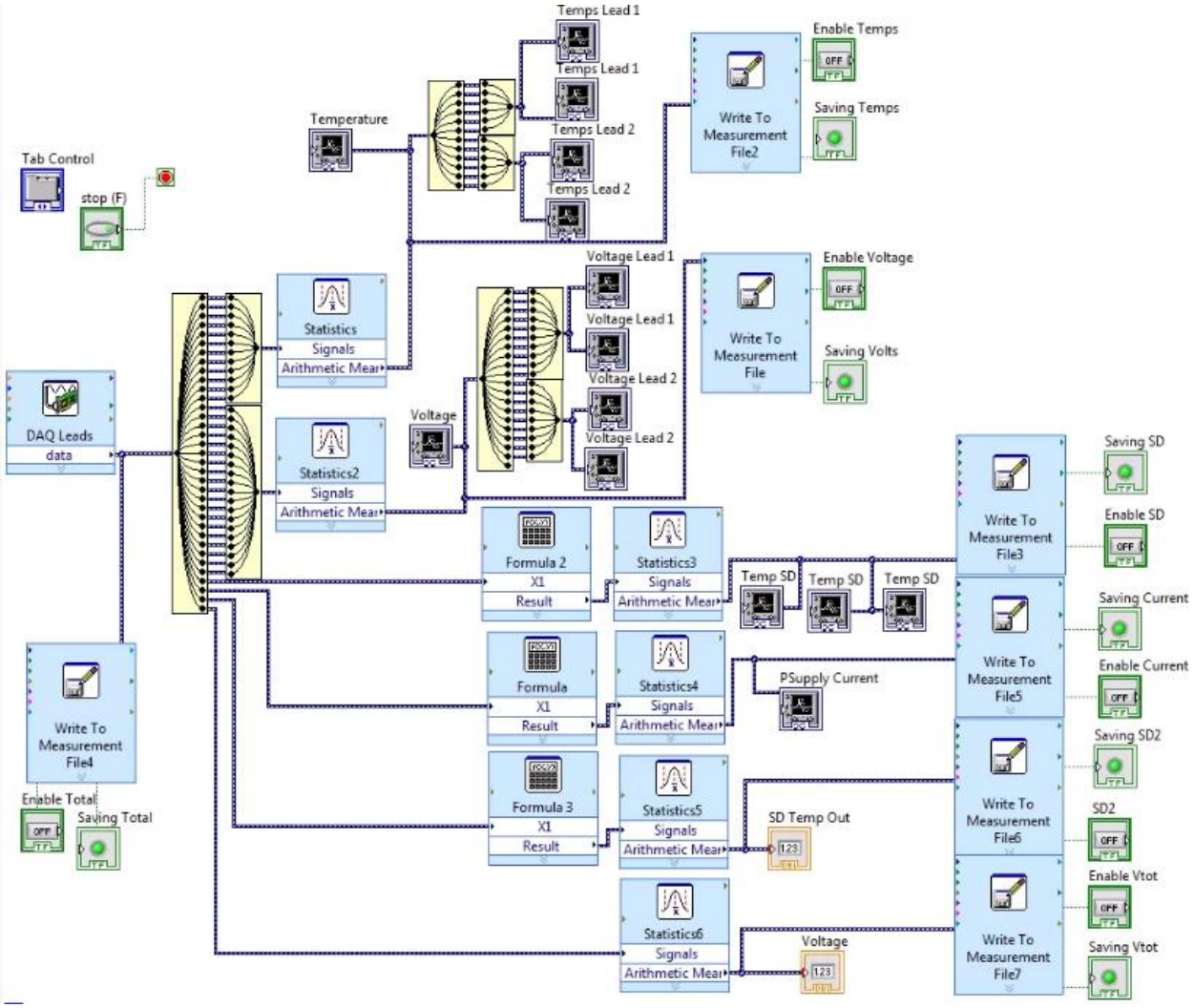

Figure 28: Block Diagram of National Instruments LabVIEW data acquisition and storage program

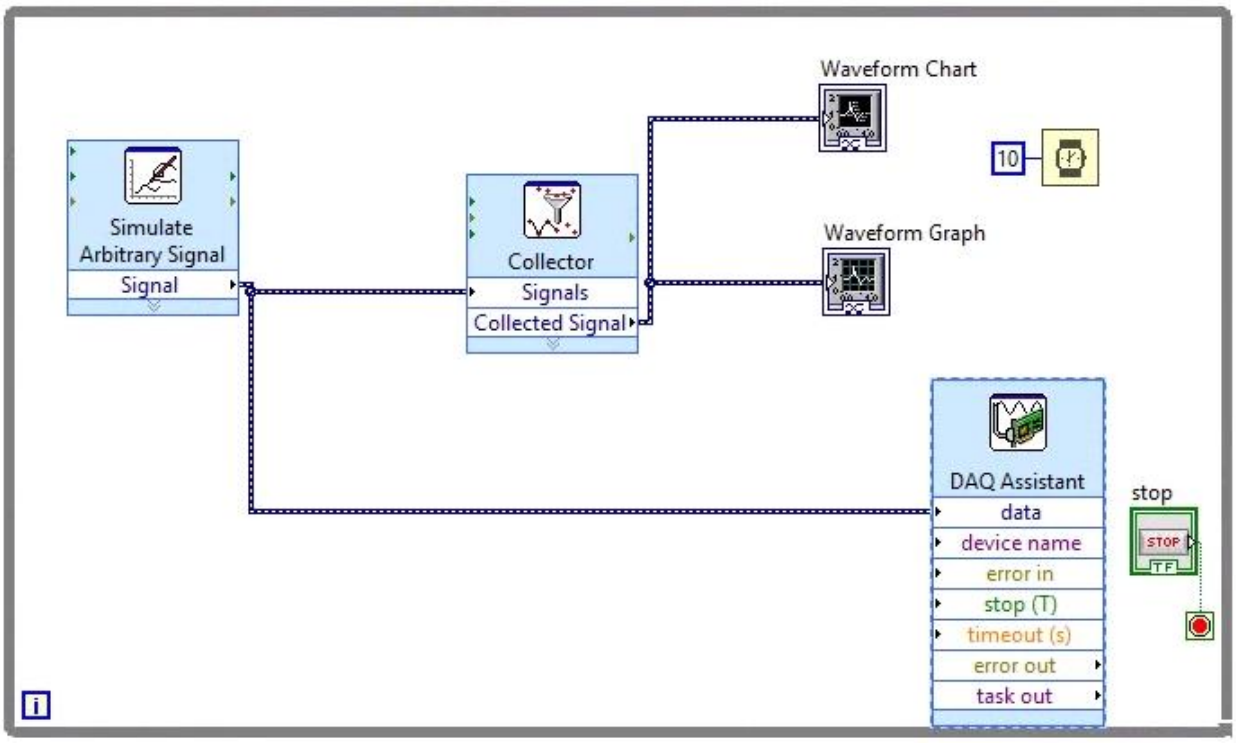

Figure 29: Block Diagram of National Instruments LabVIEW current control

3.4 Experimental Equipment

To replicate the conduction cooled current leads used in the UW Madison SMES device, a test fixture was fabricated and attached to the cold finger of an electrically isolated single stage Gifford McMahon cryocooler. The test fixture was positioned in a vacuum dewar which was pumped to $\leq 10^{-4}$ torr with a turbo pump to minimize residual gas conduction heat leak. The leads were connected to a Hewlett Packard 6681A 8V/580A programmable DC power supply capable of 580 A DC via a terminal feed into the dewar. The test equipment interactions can be seen in the diagram in figure 30.

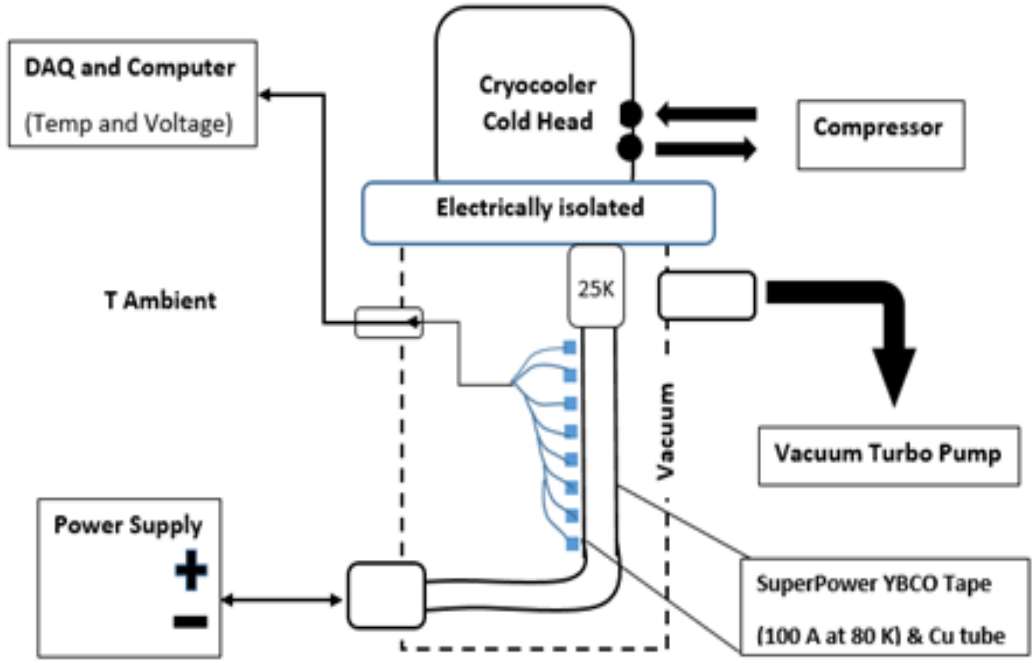

Figure 30: Diagram of major experimental equipment used in the current lead test setup

3.4.1 Cryocooler and compressor

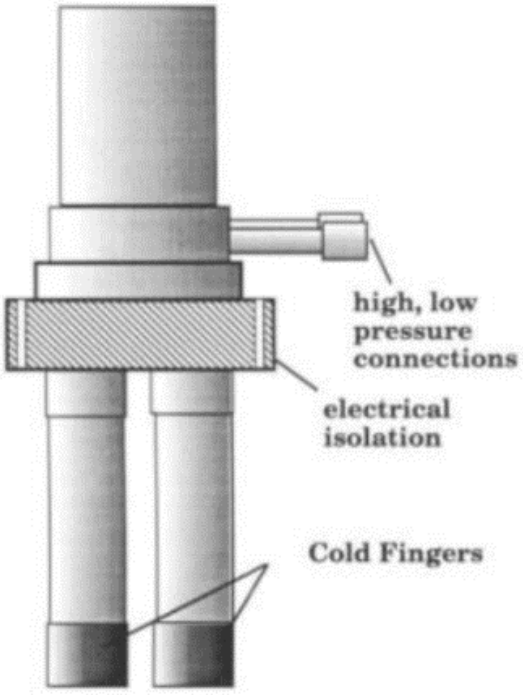

Figure 31: Twin finger GM cryocooler diagram [42]

Figure 32: Twin finger GM cryocooler used in the experiment

To cool the test fixture down to cryogenic temperatures, a single stage Gifford-McMahon twin finger cryocooler was used. The cold finger was designed and fabricated by the University of Wisconsin and Cryomech specifically to be used for the cooling of current leads possessing two electrically isolated cold fingers. With the capability of 60 Watts of cooling capacity at 70 K, the cryocooler was effective in achieving the temperatures needed to simulate those that would be encountered by the SMES current leads. Heat is carried from the cold finger to the warm end of the GM cooler by means of internal Helium gas to allow for electrical isolation of the two fingers. The cooler was design to avoid any electrical breakdown in the helium gas while eliminating the thermal resistance that would normal be associated with an electrical insulator [42]. For this experiment only one of the fingers is used, but for actual SMES current leads requiring electrical isolation, both cold fingers would be needed.

The cryocooler is powered by a 5 kW model CP640 compressor that supplies it with ultra-high purity helium gas through flex lines connected via Aeroquip low air inclusion quick disconnect plunger connectors. Prior to using the compressor and cryocooler, the system and lines were purged and then charged up to 200 psi with ultra-high purity helium via the service access valve for operation.

Figure 33: CP640 compressor used to power the Twin finer GM cryocooler for the experiment

The Cryocooler itself operates the Gifford-McMahon refrigerator cycle used to reject the heat in a four step cycle. The pressurized Helium working fluid rejects heat through an irreversible

process created by the isothermal expansion of the helium gas. This process works by utilizing the high and low side of the compressor in combination with a regenerator and displacer to compress and expand the helium gas in the compression expansion space.

3.4.2 Vacuum ruffing pump and turbo pump

To run the experiment properly and effective heat leak to the cold components, a residual gas pressure of 10^{-5} torr is desired. The primary purpose of evacuating the experiment below this pressure is to eliminate residual gas conduction as displayed earlier in the thesis and seen in figure 9. To achieve these pressures, KF fittings and flanges were used along with stainless steel bellow flexible hoses to connect the cryocooler chamber to a pumping station.

Figure 34: Leybold mechanical vane pump

Figure 35: Leybold Turbovac 151 pump

The pumping station includes a mechanical roughing pump and a turbo-molecular pump as seen in figures 34 and 35. The mechanical pump used was a Leybold rotary vane pump which was connected to the Leybold Turbovac 151 turbo pump via a gate valve. The roughing pump was used first to lower the system pressure and evacuate the cryostat vacuum space below 1 torr for the turbo pump. With the gate valve opened, the Turbovac pump was then turned on to achieve

the desired 10^{-5} torr. A combination of thermocouple and ionization pressure gauges were used to ensure accurate pressure measurements over the entire evacuation process. Ultimately a pressure of $1.5(10)^{-5}$ torr was achieved which is within the pressure range needed to minimize residual gas conduction heat transfer.

3.4.3 High Current Power Supply

A Hewlett Packard 6681A 8V/580A programmable DC power supply capable of 580 A DC and shown in figure 36 supplies current to the superconducting current leads via a terminal feed into the dewar.

Figure 36: Hewlett Packard 6681A 8V/580A programmable DC power supply used in the current lead experiment

To ensure accurate magnitudes of current are being supplied, the current is measured with two different methods, local voltage sensing, and with a resistor at the terminals of the supply to account for the voltage drop of the load. Current control was accomplished with two methods for constant and pulsed current conditions. For constant current data collection, the power was controlled via the front panel of the power supply. For pulsed current data collection, data acquisition equipment was connected to the back of the supply, and using the differential current programing input, the desired pulsed current requests were executed using a computer and

LabVIEW program separate from the data collection system. All connections were properly grounded, and over voltage protection was always activated prior to data collection [50].

3.4.4 Secondary low current sources

Additional power supplies used for the experiment included two Lake Shore 120 current supplies for sending 10 micro amps of current to the silicon diodes, and a Kepco low voltage low current power supply for testing the current leads at low current and at room temperature. These supplies are pictured in figures 37 and 38.

Figure 37: Lake Shore 120 current source used for silicon diode power

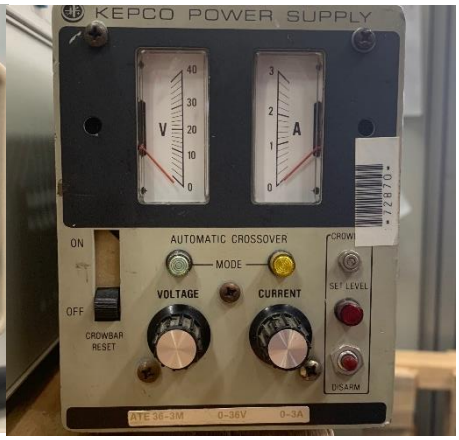

Figure 38: Kepco Power Supply used for testing

3.5 Current lead Test Fixture

3.5.1 Design

In order to investigate the thermal and electric behavior of the current leads in a pulsed current mode, a test fixture was designed and fabricated. To experimentally achieve time and position dependent voltage and temperature measurements, the test fixture was carefully designed to consider all foreseen challenges in an attempt to provide the most precise results. During the design process, several objectives were selected in order to produce reliable results.

- The current leads consist of copper tubing and 2G YBCO superconducting wire arranged in an electrically parallel configuration
- Connect the leads to the cryocooler cold finger minimizing thermal contact resistance.
- Connect the leads at the other end to the terminals leaving the dewar, without touching the dewar walls at any point.
- Spatially distribute the temperature and voltage measurements along the cold end of the leads without disturbing thermal properties.

SuperPower HTS tape was selected for the superconducting wire in the experiment given its mechanical and electrical properties when compared to other superconducting wires. The superconducting material sits on a substrate and is contained between a silver overlayer and copper stabilizer as seen in figure 39.

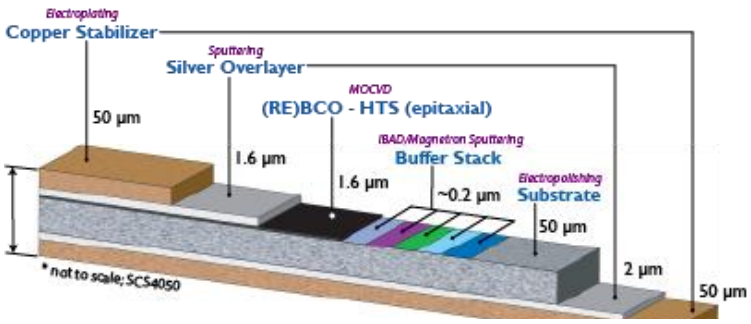

Figure 39: 2G HTS wire manufactured by SuperPower used in the experiment [56]

The copper tubing was selected was 3.2 mm with a thickness of 0.75 mm in order to minimize the thermal capacity while still maintaining a radius wide enough to interface with the 4mm wide superconducting tape. Hollow tubing was preferred because a smaller overall cross-sectional area was desired so that thermal propagation could be easily be measured above the instrumentation noise. The lead length was calculated based on the estimated initial conditions of the experiment using the numerical model.

The initial cold head temperature was estimated to be 30 K and the end of the lead connected to the terminals was estimated to be ambient temperature. Prior to building the model, conductivity integrals were used to determine the temperature distribution of the lead. The overall length of the lead is 0.765 m and includes two 180˚ bends dividing it into three vertical sections in order to fit the lead length into the available dewar volume. The first 25 cm of the lead including the superconducting section is approximately the distance from the cold finger to the bottom of the dewar. This distance was used to size the full lead length in order to place the initial transition temperature at a measurable position in the first third of the lead. The interface between the lead and the cryocooler cold finger, includes a copper plate and was designed using Solidworks. The copper plate includes holes for fastening to the cryocooler. It also includes a 4.5 mm wide channel with filleted corners greater than the 2G HTS critical bend diameter for the superconducting wire to wrap around the plate. The design provides a continuous loop of superconducting wire on both leads thereby avoiding any contact resistance in the superconducting wire sections. Two more holes on the inside of the channel allow the copper tubing to be soldered to the copper plate. An image including the geometrical dimensions of the machined copper plate can be seen in figure 40.

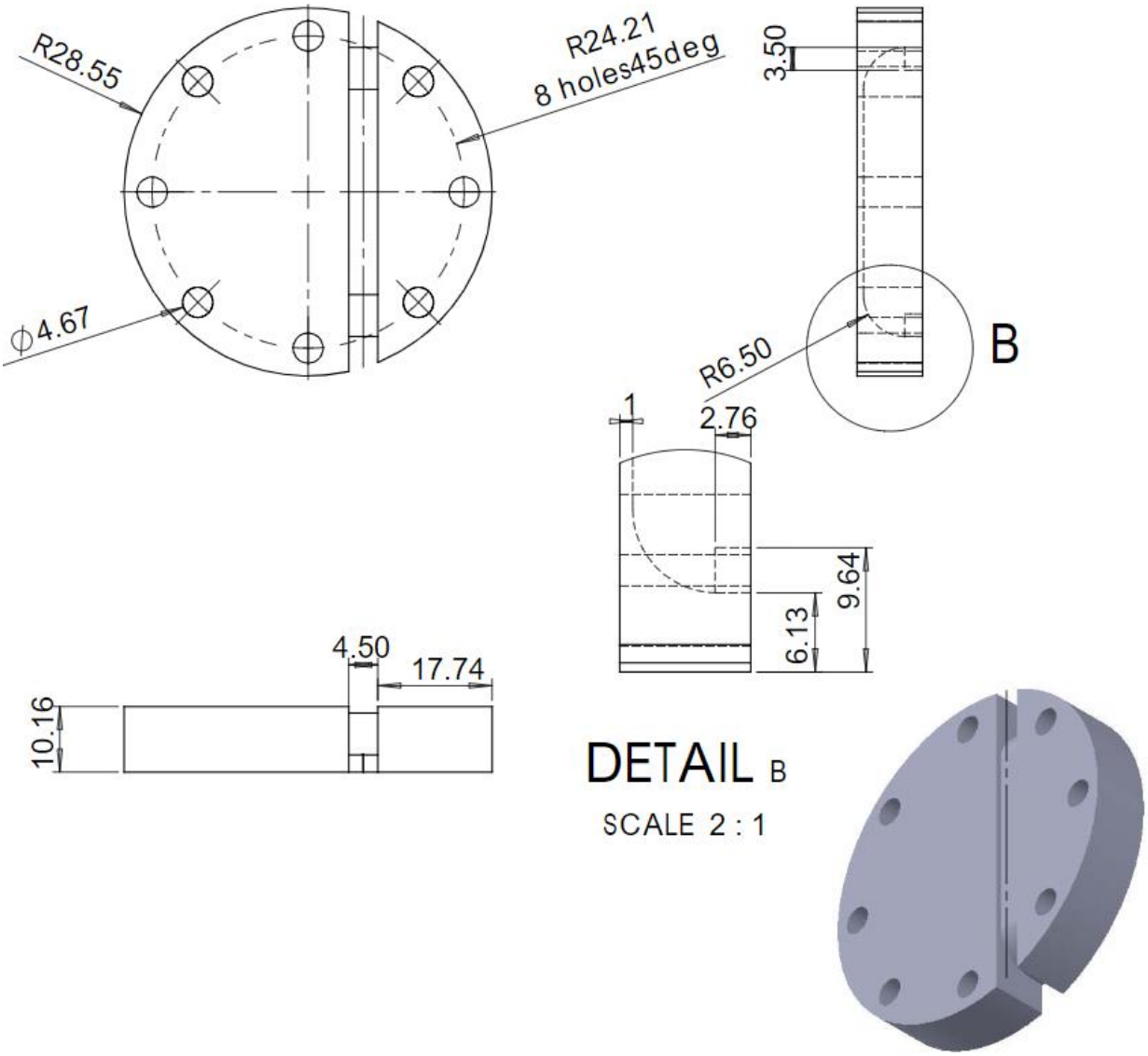

Figure 40: Geometry Dimensions for the copper plate machined to interface the current leads to the cryocooler cold head

In order to collect voltage measurements without disrupting the thermal capacitance of the wire, a measurement fixture was designed. The fixture accommodates expansion and contraction over the temperature range and avoids influencing the temperature profile of the leads. The fixture consists of a G10 plate that interfaces with the copper plate and connects to two G10 legs that are

fixed to the G10 plate using Stycast 2850FT epoxy. The legs consist of half cylinders with evenly spaced holes to allow screw-in voltage taps to make contact with the current leads without requiring any solder connection to the leads. Half cylinders enable visual inspection of the contact of each voltage tap and provide an opening for the thermal couples on the other side of the lead.

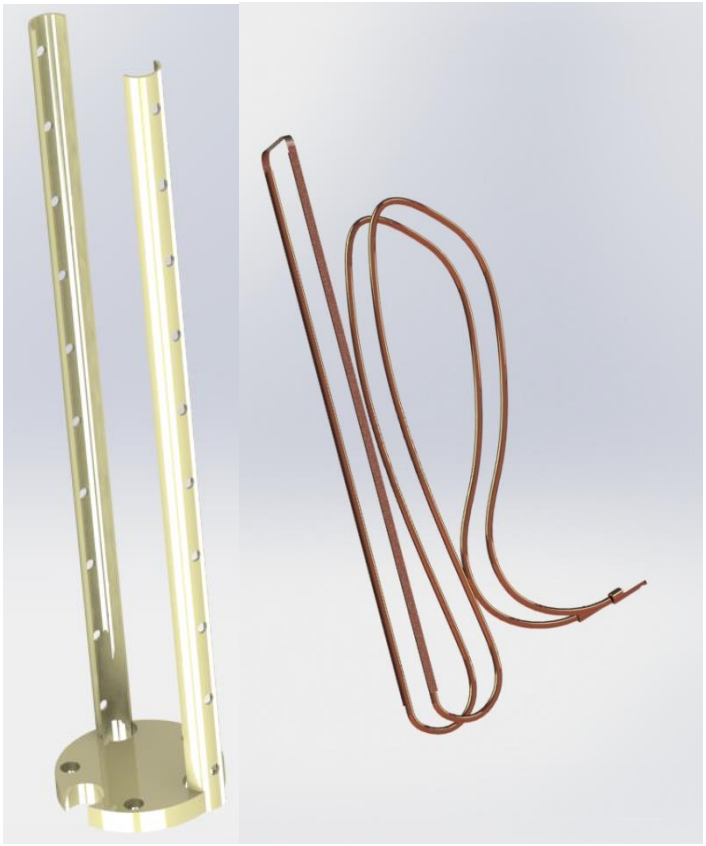

Figure 41: Computer render of the G10 fixture (left) and the superconducting current leads (right)

Spring loaded voltage contacts are utilized in order to maintain electrical contact with the leads and allow thermal contraction during cool down. The design utilizes spring contact probes in combination with hex socket button head bolts that are bored out to the outer diameter of the

contact probe assembly. The GSS conical tipped probes with crimp style receptacles [51] are depicted in figure 42.

The full design assembly integrates the leads to the cold finger of the cryocooler via the copper plate, and the G10 fixture sits on top of the plate and sits parallel to the superconducting portion

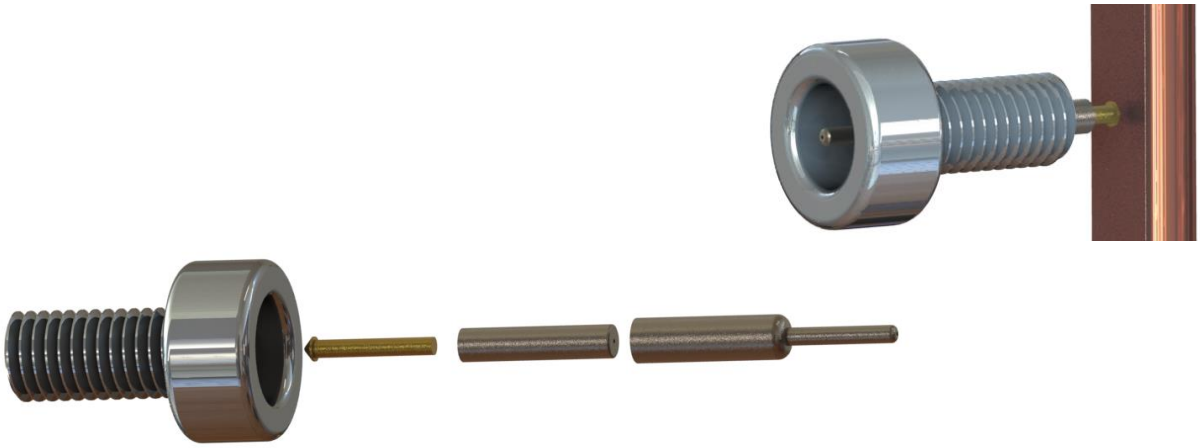

Figure 42: Exploded and assembled render of the spring loaded voltage contact design

of the lead. The voltage tap assemblies then are compressed to the HTS tape part of the lead. A rendering of this assembly can be seen in figure 43.

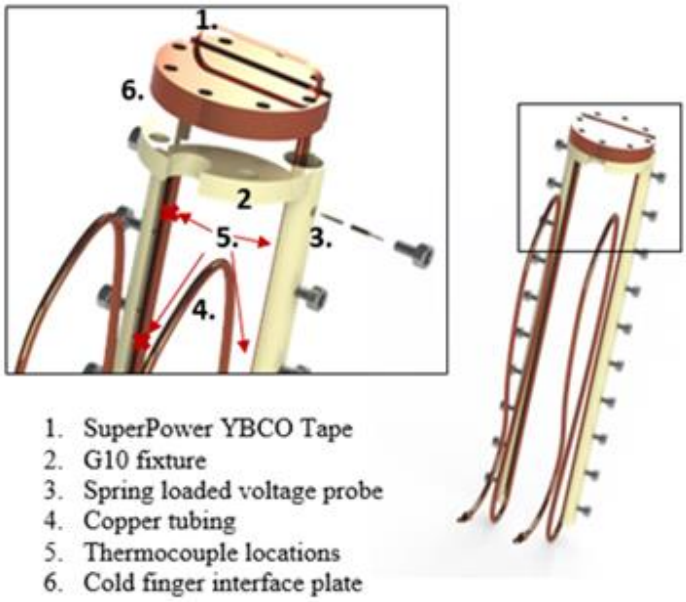

Figure 43: Solidworks Assembly render of the superconducting current leads, G10 fixture, and spring loaded voltage taps

3.5.2 Fabrication

During the fabrication process of the superconducting current leads, all precautions were taken as described by the manufacturer Superpower. The minimum bend radius of 5.5 mm [52] was not exceeded when interfacing with the copper plate and latex gloves were used when handling the HTS tape. The HTS side of the tape was determined using the manufacturer suggested method. It is important to solder to the HTS side to minimize the electrical resistance from the copper tubing to the superconductor layer. As little resin and flux were used as possible to minimize any oxidation that occurred in a previous lead design. Maximum soldering temperature of the superconducting tape was kept in mind. Superpower recommends that the soldering temperature be kept near 200 C and be in contact for no more than five minutes at a time. They also recommend that the soldering temperature not exceed 240 C [52]. The fabrication process required several steps. Copper was used for the connecting plate between the cryocooler and

leads because of its electrical and thermal conductivity. The dimensions were selected to fit with the cryocooler radius. The plate was first turned on a lathe and then machined using a 3-axis mill. The plate was manufactured with a filleted channel allowing the current leads to thermally interface with the cold finger of the cryocooler while maintaining one continuous superconductor for both sides of the lead. The channel was machined with a width slightly greater than the SC wire width, and the edges of the 90 degree turns were filleted to a radius slightly greater than the wire's critical bend radius. The copper plate can be seen in figures 44-46. The leads were carefully shaped and soldered using low melting temperature indium solder and flux. This careful process allowed the Superconducting wire to stay below 240˚C and avoided any damage to the superconducting properties of the wire. The thermal conductivity of the copper enabled the indium solder to remain liquid over most of the lead length during the entire process. For this reason the process started from the top and worked down using gravity to carry excess solder down the leads. An image of the soldering setup can be seen in figure 44 and 45.

Figure 44: The Superconducting current lead soldering setup

Figure 45: The Superconducting current lead after soldering

Proper cleaning and handling precautions of the wire were taken as recommended by the manufacturer. Manufacturing the G10 fixture was carried out carefully using proper ventilation for eye and lung protection. The raw G10 sheet and tubes were measured and cut using a band saw and drill press and then sanded down to the desired sizes. Finally the fixture was positioned and epoxied with Stycast 2850FT epoxy so that it was ready for assembly. The drilled holes in the G10 were then tapped by hand to fit the screw-in voltage taps. The G10 fixture can be seen in figures 46.

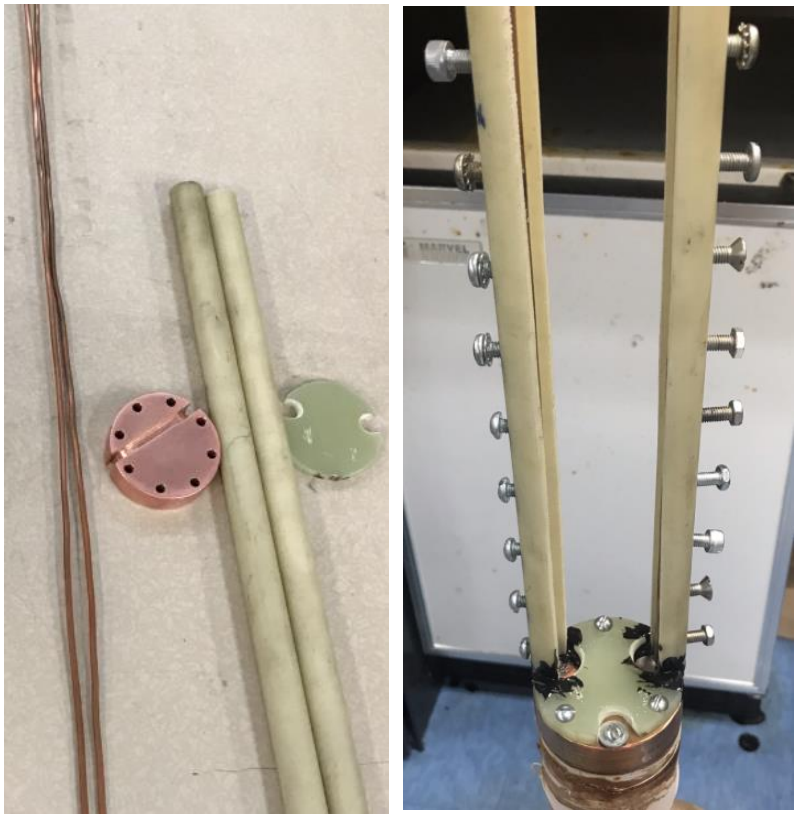

Figure 46: Components used for the test fixture (left) assembled G10 fixture (right)

Fabricating the 20 screw-in spring loaded voltage contacts proceeded as follows: Voltage taps purchased as two parts from Mouser Electronics included the GSS-100 conical tip spring contact probe with a spring force of 3.8 oz and the RSS-100-CR crimp receptacle that houses the probe. 2 mm diameter center holes were drilled through the socket-head bolts. The receptacles were then carefully placed in the bolt holes and epoxied in place using the Stycast epoxy. Conductive measurement wire was placed in the opposite end of the receptacles and crimped in place. An image of the twist-in spring loaded contact probe can be seen in figure 47.

Figure 47: Spring loaded voltage contact probe bolt assembly

3.5.3 Assembly

The experiment assembly process began by connecting the current lead assembly to the cold finger of the cryocooler. A thin sheet of indium was used at the interface to minimize thermal contact resistance between the copper plate and the cold finger of the cryocooler. Next the instrumentation fixture was fastened over the copper lead plate so that the leads were centered to the radius of the G10 half-cylinders. Each individual spring loaded voltage tap was screwed in and placed carefully on the center of the superconducting tape. Next the thermocouple sensors were epoxied to the leads using Stycast epoxy and spaced at approximately 5 cm increments on the copper tubing side of the leads opposite the voltage taps. All the instrumentation wires were bundled and attached to individual pins on the vacuum feed-through ports. The non-superconducting portions of the lead were bent in a geometry that was measured and calculated to fit inside the dewar without touching the walls. Copper terminals were soldered onto the end of the leads and connected to the high current feed through terminal. A 30 layer MLI blanket was fabricated to fit the geometry of the dewar and to maximize coverage of the experiment. Care was taken in the assembly of the MLI blanket to prevent parallel conduction between layers at the edges due to the high conductivity of MLI in the parallel direction. Kapton tape was used on the inner and outer layers as a safety precaution against any shorting from the leads to the dewar container. The Cryocooler and lead assembly was then carefully lowered into the vacuum dewar and sealed for testing. Some of the steps in the assembly process can be seen in figure 48.

Figure 48: Steps taken in the Assembly process of the Superconducting Current lead experiment

3.6 Preliminary test validation

3.6.1 Superconductivity test

Before experiment data collection could take place, several preliminary tests were carried out in order to confirm that all components were working properly. Once the HTS tape was soldered to the copper tubing, preliminary testing was required to ensure that the wire possessed superconducting characteristics and was not damaged during assembly. A simple series of experiments were conducted to validate superconductivity. The fabricated lead was placed in a liquid nitrogen bath so that the entire superconducting portion of the lead was submerged as seen in figure 49.

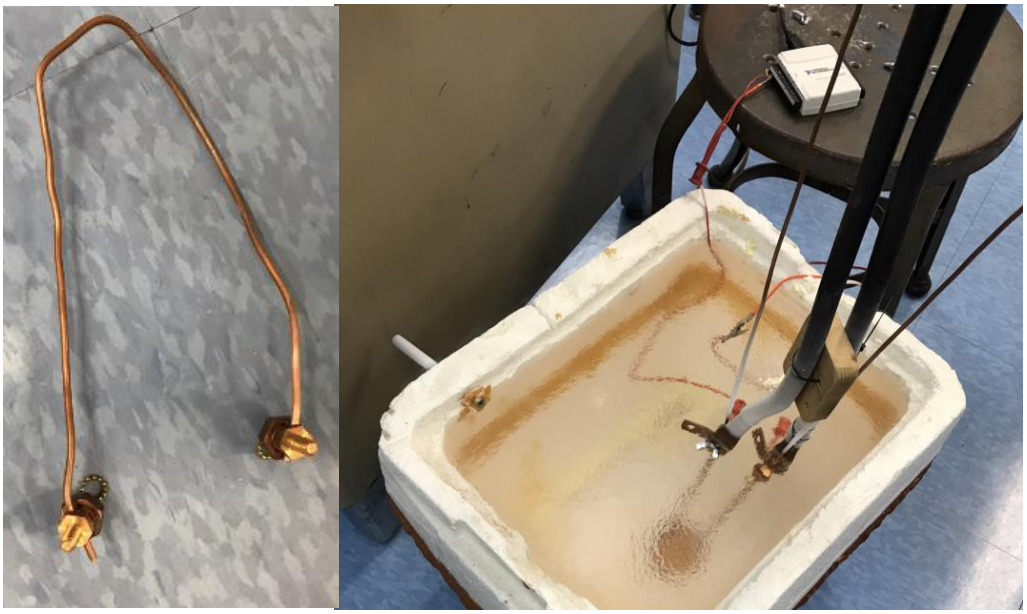

Figure 49: Copper tubing (left) and superconducting leads (right) used in the experiment

The power supply was connected to the terminals at the end of the lead. Voltage clips were placed across different sections of the lead. The power supply was increased in steps of 10 Amps and the voltage was measured for each step. This was accomplished using a Hewlett Packard 6681A programmable DC power supply. Data was collected with a USB mini-daq and recorded using LabVIEW. Several trials were conducted looking at multiple areas of the leads

and then across the entire leads. Current values up to 210 A were used and over-voltage protection was put in place. Next, a piece of the same copper tubing used in the fabrication of the current leads was submerged in the liquid nitrogen. The copper piece was subjected to the same conditions of current and voltage measurements were taken. A comparison of the results can be seen in figure 50.

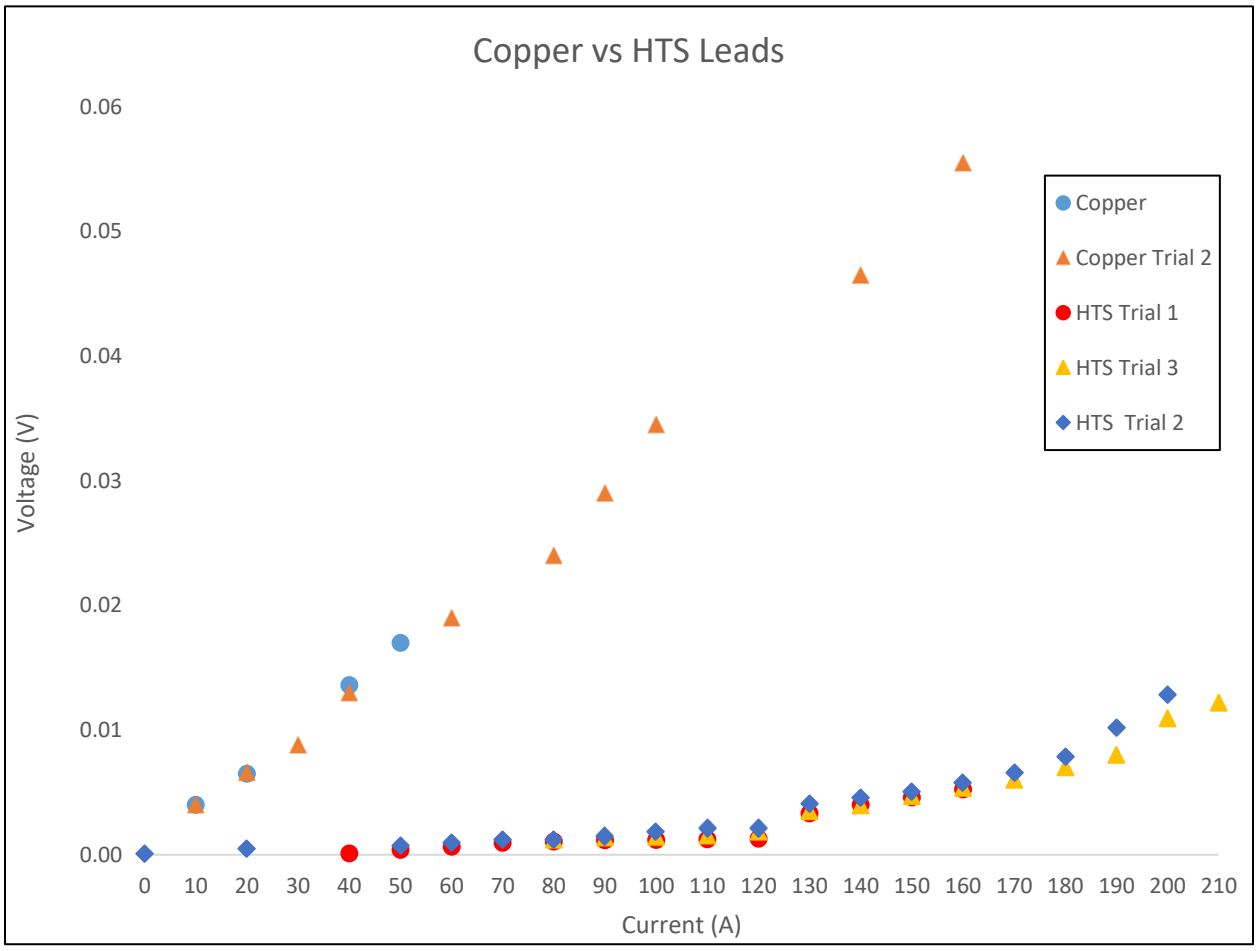

Figure 50: Data collected for the superconductivity validation test

Figure 50 reveals that the superconducting lead remains very close to zero voltage up to 120 A. At around 130 A, the voltage begins to increase. Calculations of the expected voltage for the copper tubing as well as the expected critical current for the superconducting wire at the liquid

nitrogen temperature of 77K agree with the experimental results. The voltage of the SC lead begins to increase once the applied current exceeds the critical current of the HTS tape for the given temperature. At this point the lead is current sharing. That is, the superconducting material continues to carry its critical current density while the remaining current is carried in the copper part of the lead thus producing the observed voltage. At 77 K the manufacturer's expected critical current for the 2G HTS tape in zero field is 139 A. Thus, the superconducting tape's critical current density measured at 77 K is in reasonable agreement with the manufacturer specifications. The superconducting properties of the leads were validated and it behaves as expected.

3.6.2 Evacuation testing.

To operate the cryocooler and maintain effective cooling, the experiment must operate at vacuum pressures. To confirm this system, the experiment was sealed and evacuated following the evacuation procedure highlighted earlier in the paper. The turbo pump was left on for several days and maintained a pressure of $1.5*10^{-5}$ torr.

3.6.3 Continuity and grounding Tests

Given the multiplicity of wires and complexity of multiple power sources, ensuring continuity and grounding was very important. After the instrumentation wires were all soldered and installed, each of the 60 wires were checked for continuity and grounding against the other wires. Effective labeling and wire routing simplifies troubleshooting for wiring shorts or open circuits. All wires and cables were also checked for proper grounding. Finally the digital multi-meter was used to ensure that all components of the vacuum dewar and cryocooler were electrically insulated from the high current power supply.

3.6.4 Low voltage lead testing and power supply control testing.

Following continuity tests, the voltage tap configuration was checked by sending low values of current through the leads while they were at room temperature using a 3A-30V Kepco power supply. This test provided a sanity check to ensure the measurements would produce realistic data. The power supply was used to send current through the leads at 1 amp increments between 1 and 3 amps. The measured voltage was then compared to the calculated values for the corresponding current and resistivity of copper at room temperature. The results of this test agreed with the calculated values for voltage validating the measurement method. Results can be seen in figure 51.

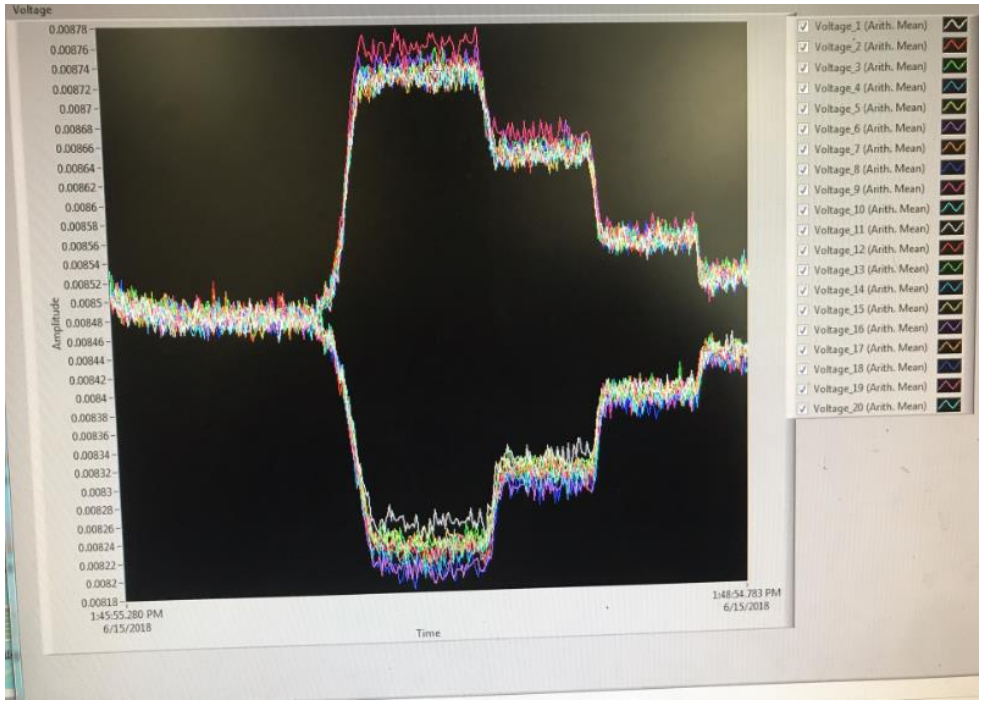

Figure 51: LabVIEW data from the room temperature low voltage validation test

To prepare for high current testing, the power supply control program was tested at a low current value, allowing the two current measurement methods to be compared. With the current control and all instrumentation working, the experiment was ready for low temperature testing.

3.6.5 Cool down test and heat leak calculation

A cool-down and operation test of the Cryomech GM Cryocooler was conducted to confirm expected performance. The cold finger of the cryocooler cooled to 50 K in roughly 6000 seconds or ~1.7 hours as shown in figure 52. The cooler continued to run overnight and achieved temperatures as cold as 23K. In addition to the cooling process, a heat leak calculation

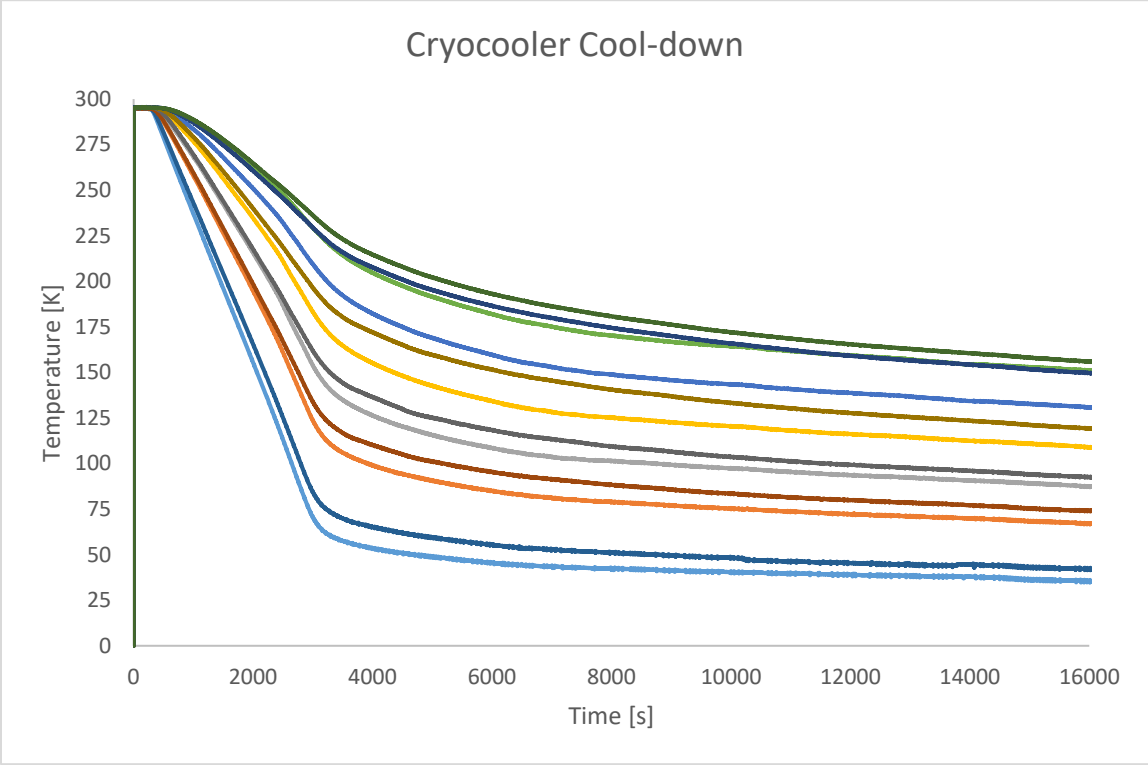

Figure 52: Plot of the first cool down of the Cryomech GM twin finger cryocooler displaying the temperature of various nodal positions.

was carried out based on material properties and geometry. The heat leak calculation included all methods of heat that could enter the cooler: conduction through the leads, the instrumentation wire, radiation through the MLI and non-MLI regions, and residual gas conduction. As expected, the dominant sources of heat leak consisted of the conduction through the leads, and the radiation through the surface areas unable to be covered by the MLI such as the cold fingers and terminal hole. An energy balance of the heat leak calculation placed the estimated

temperature of the cold finger at approximately 30 K in fair agreement with the experimental measurement.

4. Data collection and analysis

4.1 Pulsed Current Results

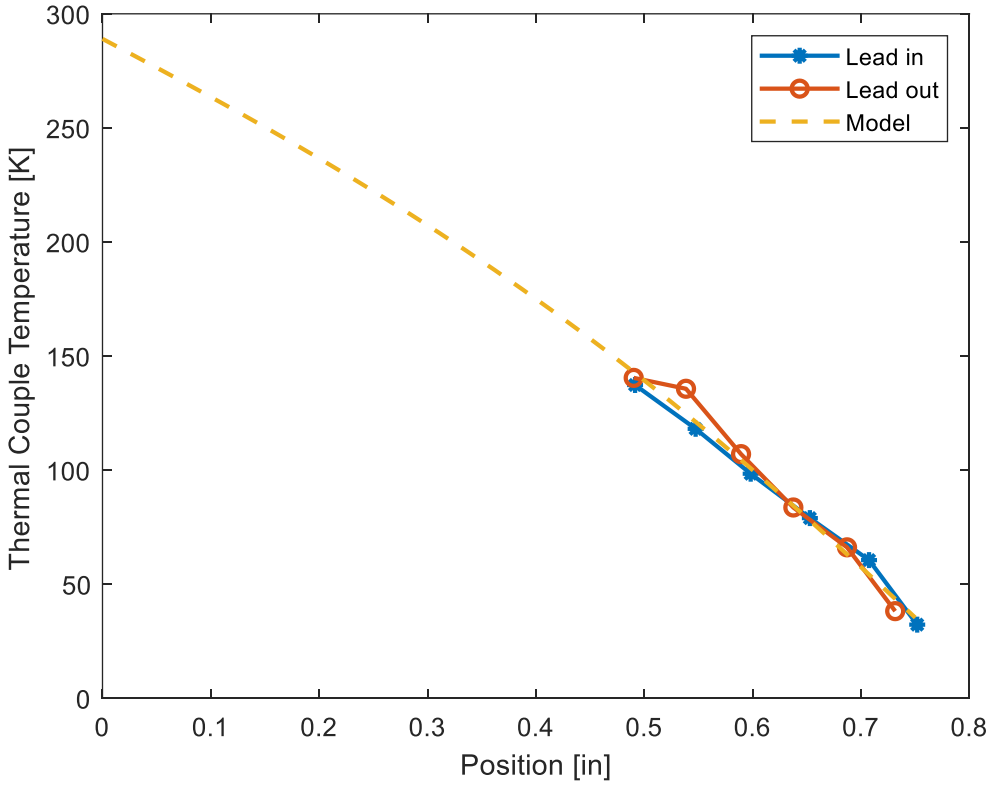

Figure 53: Initial temperature distribution of the numerical model (yellow) and experimental data (orange and blue

Initial steady state temperature values with zero current applied are displayed in figure 53. The initial experimental temperature distributions displayed in blue and orange (for the two different leads) reveal a very strong agreement with the model predictions overplayed in yellow.

Once steady state temperatures were reached, a pulsed current signal was sent using the LabVIEW program and the Hewlett Packard 6681A programmable DC power supply. The

current cycle pulses displayed in figure 54 demonstrate that the Hewlett Packard DC power supply and National Instruments data acquisition are able to maintain a well-defined wave form

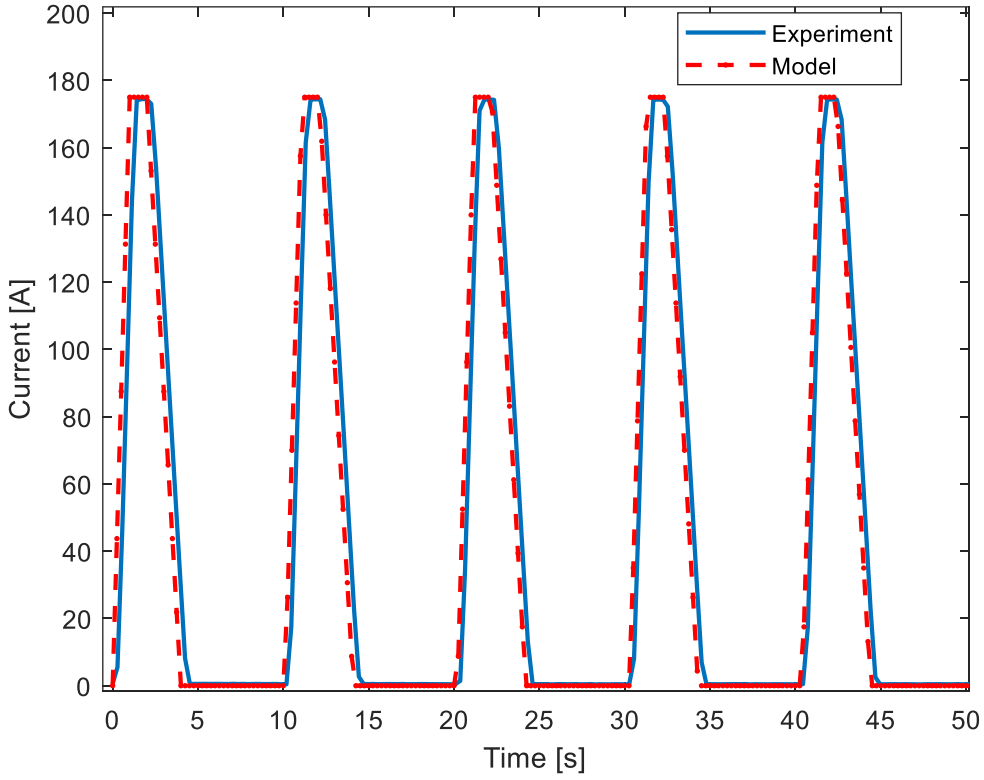

Figure 54: 10 second current Cycle of 175 A DC current with 1 second ramp, 1 second hold, 2 second ramp down, and 6 second relaxation time.

that agrees with the model even under high amplitudes and ramp rates of the current pulse.

The voltage of the current lead was measured at individual nodes and also across the terminals of the lead at the dewar entrance. The voltage across the leads can be compared to the sum of the model nodal voltages. The two voltages plotted in figure 55 evaluate different lengths of the current lead so the magnitudes are different, but the overall slope increases at the same rate suggesting consistency in the change of resistance over time for both the model and experiment.

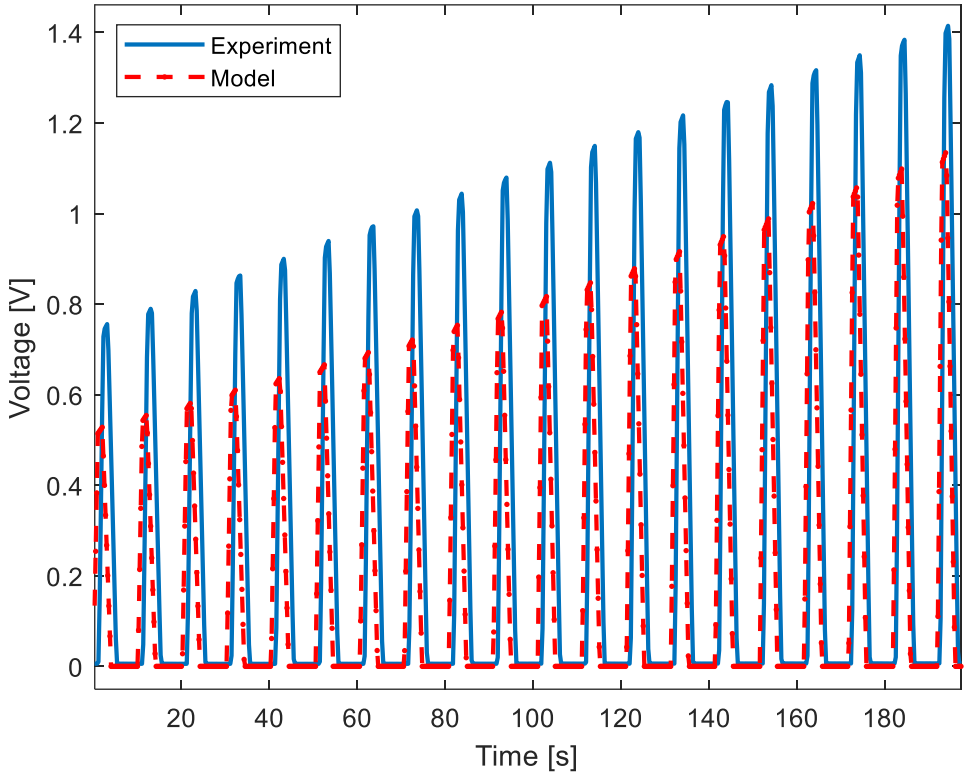

Figure 55: The sum of nodal voltages in the model overlade on the voltage across the lead terminals of the experiment

The temperature at the first node location where the voltage in figure 55 was being measured at the entrance to the vacuum vessel was also recorded and can be compared to the temperature of the first node in the model. Agreement between these two temperatures meant that the model was capturing the energy storage and heat leak of the warm end accurately. The warm end boundary condition for the model that best captures the transient short and long term measurements is defined by a finite conduction path of approximately 10 m representing the cables connected between the power supply and the first node of the lead. A natural convection term of 5 W/m-K to ambient temperature is also included. The power cable length and heat transfer coefficient were used as tuning parameters in the model. Figure 56 shows the temperature data measured at the warm terminal end of the leads for two different current duty

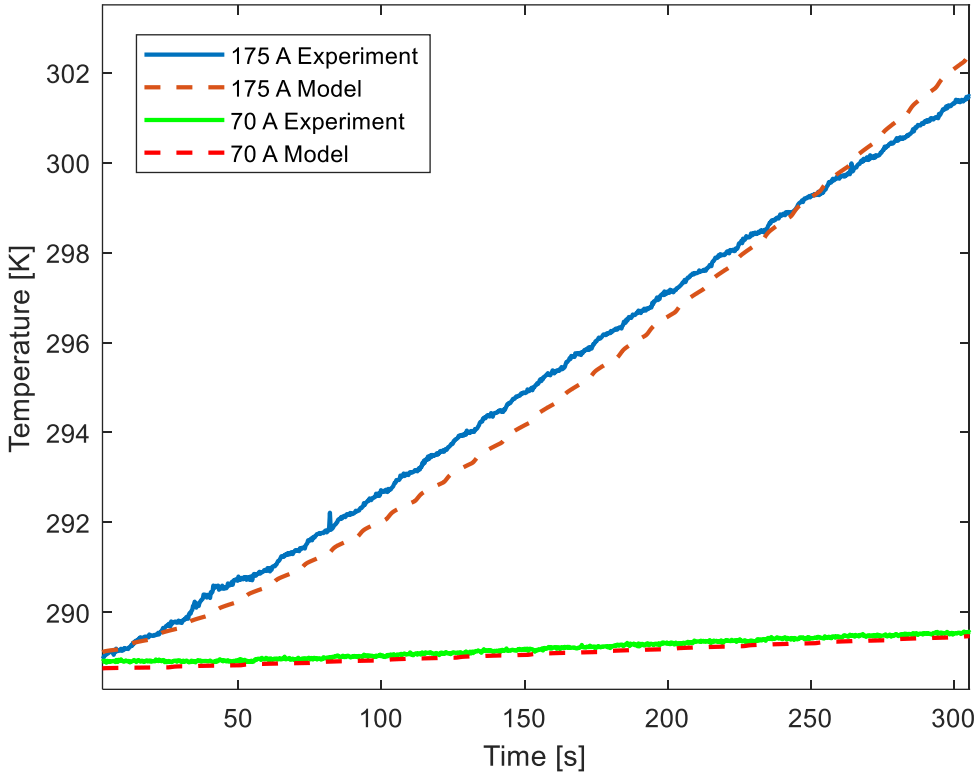

Figure 56: The computer model overlaid on the experimental data for both a 175 A pulse with a 6 second relaxation time and a 70 A pulse with a 21 second relaxation time

cycles with the temperature of the first node in the computer model overlaid. From this figure we can see that the model accurately captures the behavior in the two extremes of both a more frequent high current pulse and a less frequent lower current pulse.

Comparing the nodal temperatures of the experimental data to that of the numerical model ultimately determines how strong the agreement between the two is. Looking at a pulse signal of a 70 A cycle with a downtime of 21 seconds reveals how well the energy storage and heat flow is captured by the model. Figure 57 shows the change in temperature with respect to time for both the experimental data (solid lines) and transient numerical model (dashed lines) for 6 nodal positions near the cold end of the lead.

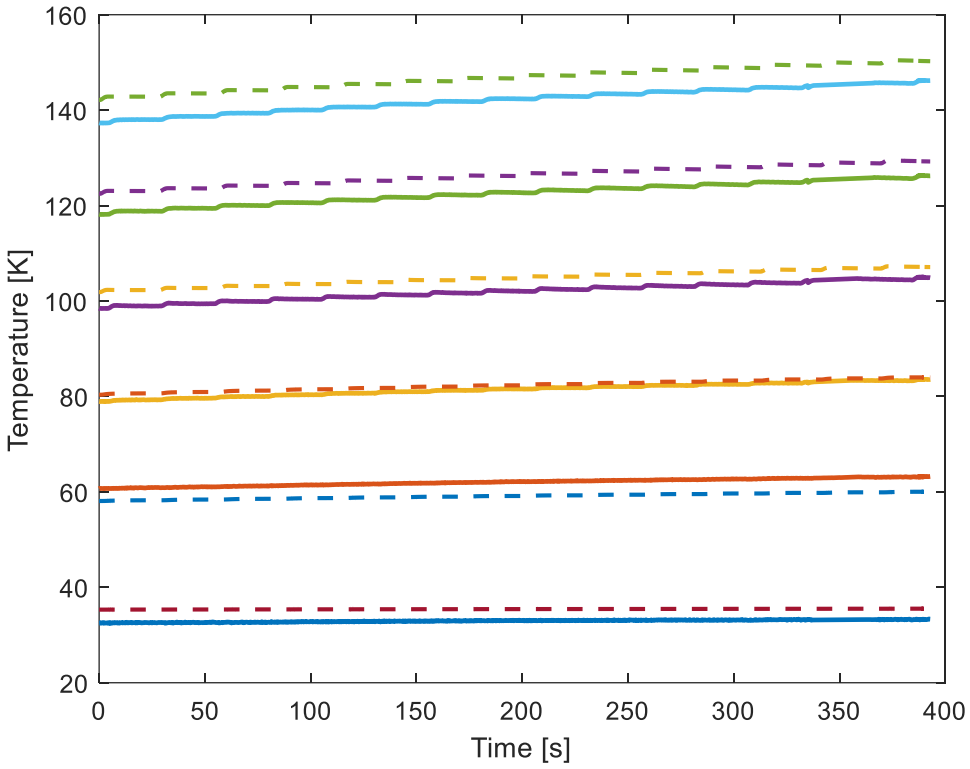

Figure 57: Temperature with respect to time for experimental data (solid lines) and numerical model (dashed lines) for a 70 A cycle with 1 second ramp up, 1 second hold, 2 second ramp down, and 21 second relaxation time

The agreement between the model and experimental data under this condition is very strong as there is very minimal deviation between the model and the experimental data over time.

Determining quasi-steady state operating conditions for various conditions with a computer model can be very useful to avoid having over or under sized leads. Both the experiment and model were used to determine this quasi-steady state. The steady state operating condition takes a significant amount of time to be achieved due to the diffusive time constant. Recall from figure 14 that it can take up to 300 seconds for the thermal wave of heat generated in the middle of the lead to each one of the boundaries. Figure 58 displays data collected over 3500 seconds (~1 hour) of a 70 A pulse cycle with 21 seconds of down time between pulses. Displayed are the same nodal temperatures with respect to time as figure 57.

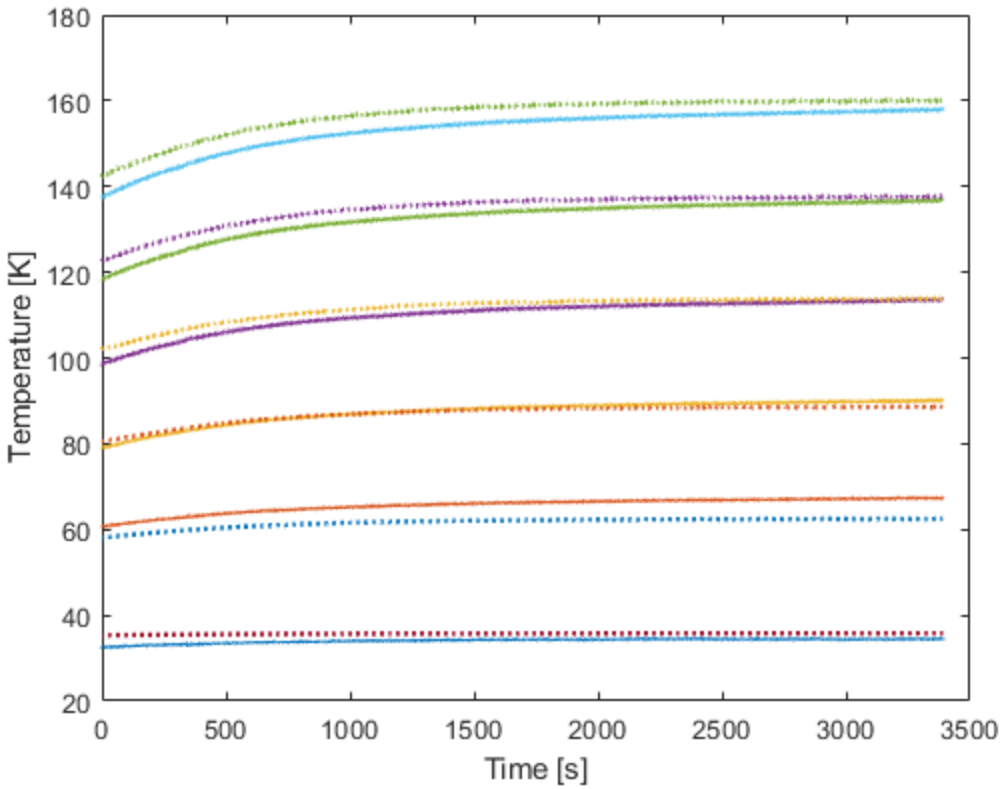

Figure 58: Experimental data(solid line) and numerical model (dotted line) of a 70 A current cycle of 1 second ramp up, 1 second hold, 2 second ramp down, and 21 second relaxation time approaching quasi-steady state

Figure 58 shows that the thermal behavior of the superconducting portion of the lead is in strong agreement with the model over a long period of time, but it is also very important to look at the behavior comparison under more extreme conditions that result a larger heat generation over a short time period. Figure 59 displays a 210 A current cycle with a 6 second relation time

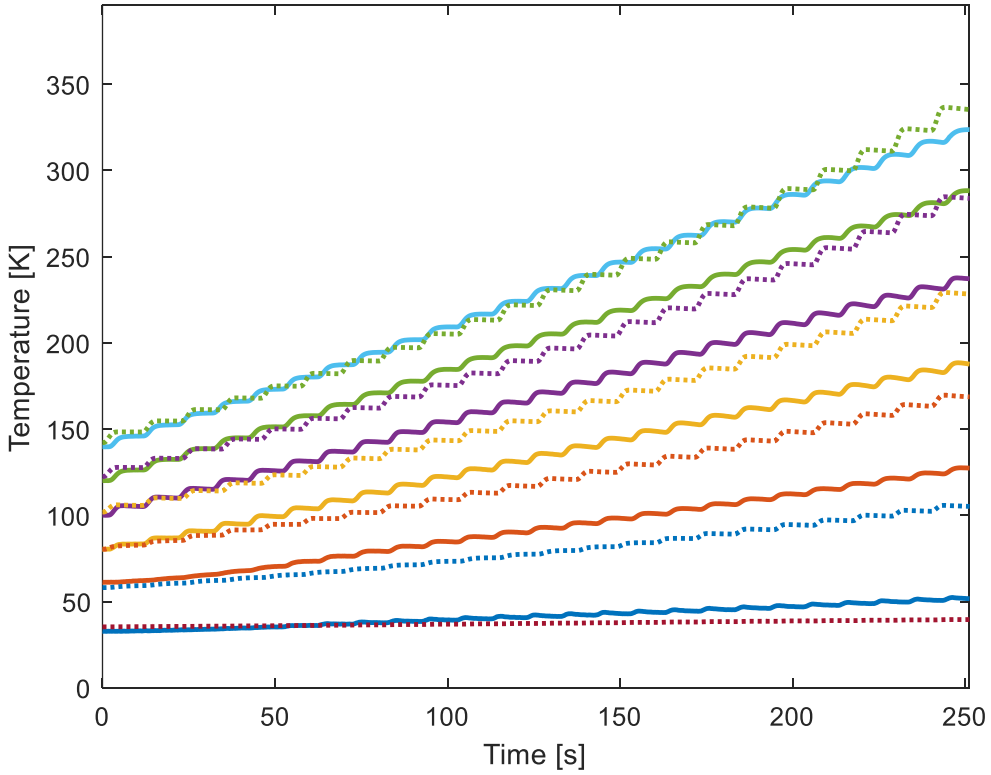

Figure 59: Nodal temperatures of the current lead with respect to time of the experimental data (solid line) and numerical model (dotted line) for a 210 A current cycle with a 1 second ramp up, 1 second hold, 2 second ramp down, and 6 second relaxation time

between pulses. In the case of high current operation (210 A), the data was collected over only a short time period to avoid the warmest points of the lead approaching dangerous temperatures. A current lead of this size is not able to sustain currents of this magnitude for long periods of time unless the relaxation times are much longer. Figure 59 reveals a stronger overall agreement between the model and measurements in the warmer three traces while the temperatures of the colder three sets of data increase faster than predicted by the model. One

reasonable hypothesis is that radiative coupling between the leads, not included in the model, causes it to slightly uder-predict the temperatuers near the cold end. Within the vacuum dewar the leads are contained inside radiative shielding as well as shaped into a geometry where warmer portions of the lead are only a few centimeters away from colder portions of the lead. It is reasonble to suggest that heat from the warmest parts of the lead under these current pulse conditions that are heating up to over 600 K are radiating heat directly to the colder portion of the leads either directly or by reflections off the radiation shielding. With a change in temperature of up to 550 K between the warmest and coldest regions this could have a visible impact.

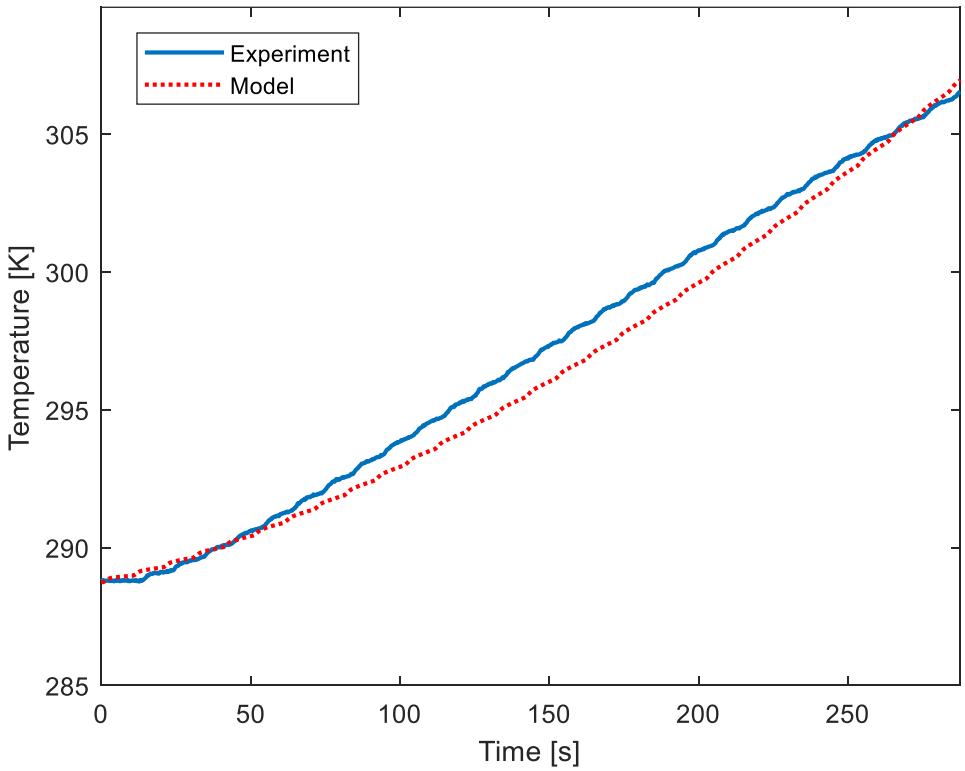

Figure 60: Temperature at the warm end for the experimental current leads and the numerical model for a 210 A current pulse with a 1 second ramp up, 1 second hold, 2 second ramp down, and 6 second relaxation time

Figure 60 displays the temperatue with respect to time for the warm end of the lead along with the temperature at node one of the numerical model under the same current conditions as figure 59. While experiencing a 210 A current pulse with a 6 second relaxation time, the numerical model captures the behavior of the experiment quite well for the 300 second data period. This evidence in combination with figure 59 validates the thermal behavior of the model under these extreme current conditions quite well.

With the model effectively capturing the behavior of the temperature distribution at both the warm end and all the nodes in the superconducting region it can be used to estimate the warmest temperatures of the lead that aren't being measured experimentally.

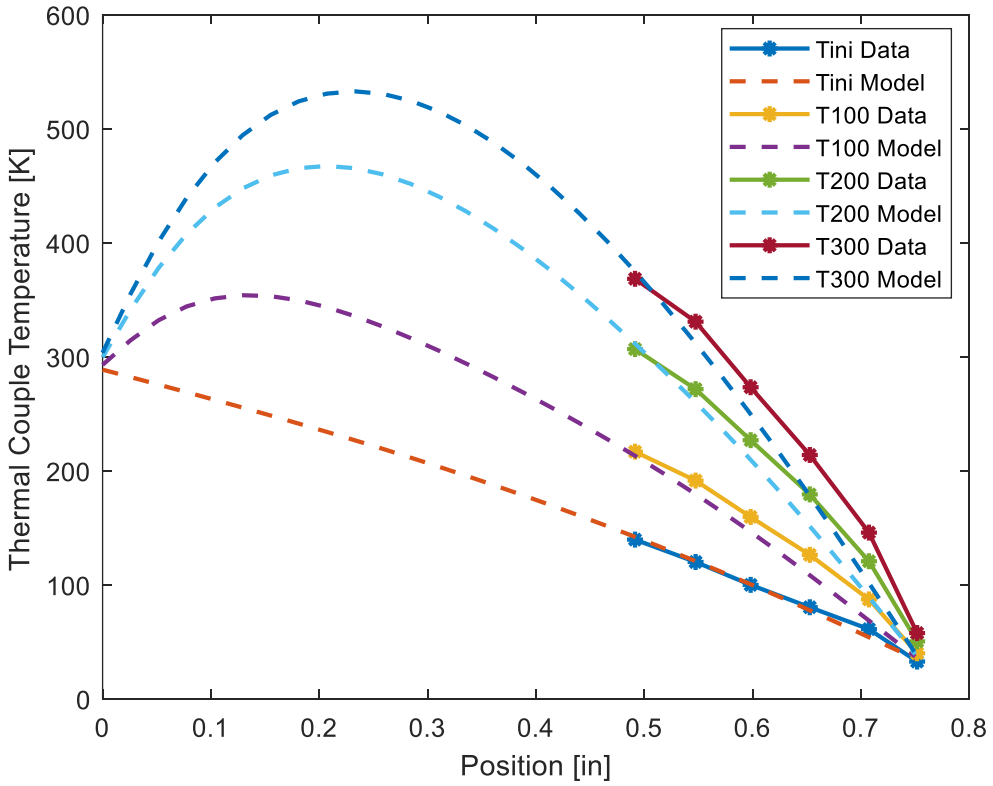

Figure 61: Lead temperature distribution for the model and experimental data at different points in time for the same current conditions as figures 60 and 59

As before, we can see the slight under prediction of temperature near the cold and that is suspected to be due to radiative coupling. Figure 61 allows us to predict that the warmest point in the lead after 300 seconds of this pulse cycle will be around 550 K. Also notice that even though the time steps are equal, the temperature increase between 100 to 200 seconds and between 200 to 300 seconds are not equal. This method can also be used to look at the temperature distribution for a lead operating condition that reaches steady state. For example, a 175 A pulse with a 26 second downtime (30 second duty cycle) results in the temperature profiles shown in figure 62. Here it can be seen that even though the time increments are the

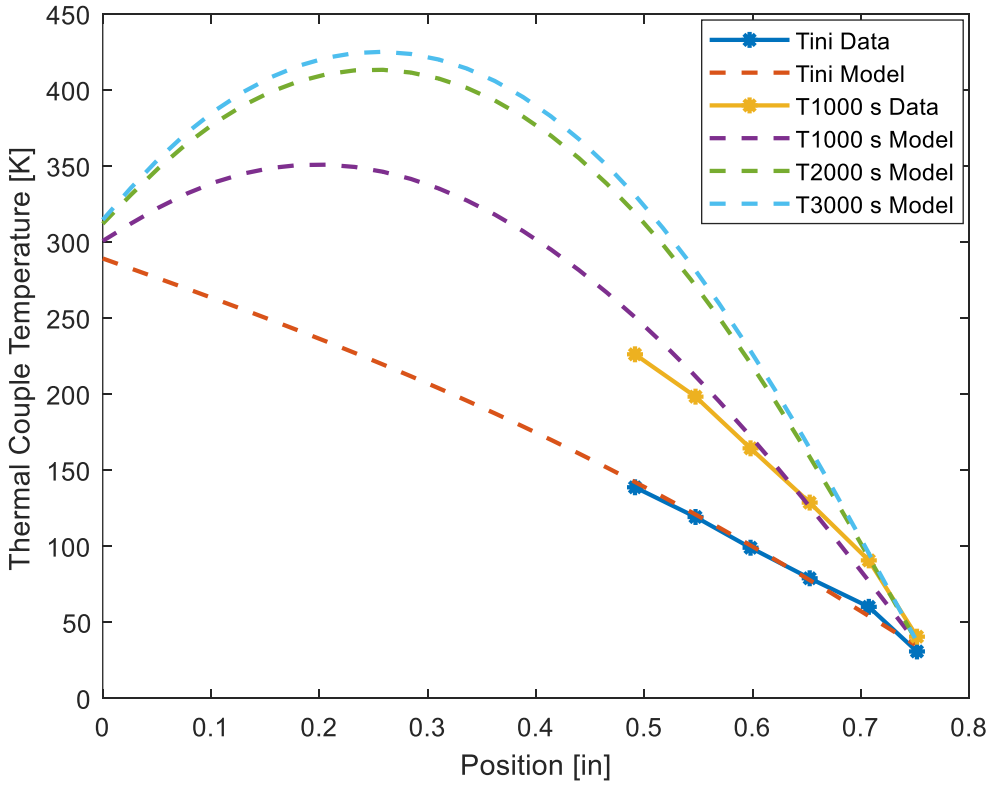

Figure 62: Nodal temperature distribution at different points in time of experimental data and the numerical model approaching quasi-steady state for a 175 A current cycle with a 1 second ramp up, 1 second hold, 2 second ramp down, and 26 second relaxation time

same for each data set, the change in temperature between the 3rd and 4th set clearly signals that the current lead is approaching a quasi-steady state, which would likely occur sometime shortly

after 3000 seconds. We can also predict based on the trend of the data that the experimental steady state temperatures will be slightly below the model predicted values.

4.2 Current Sharing Transition Zone

Using the model we can also observe the transition zone and compare it to the experimental results. Figure 63 displays the voltage and temperature for both the experimental data and the model at a location where the superconductor begins to transitions to its normal state. Consistent with the critical temperature of 73 K when operating at 175 A, both the experimental and numerical model temperature are near 73 K (right axis of figure 63) when a non-zero voltage

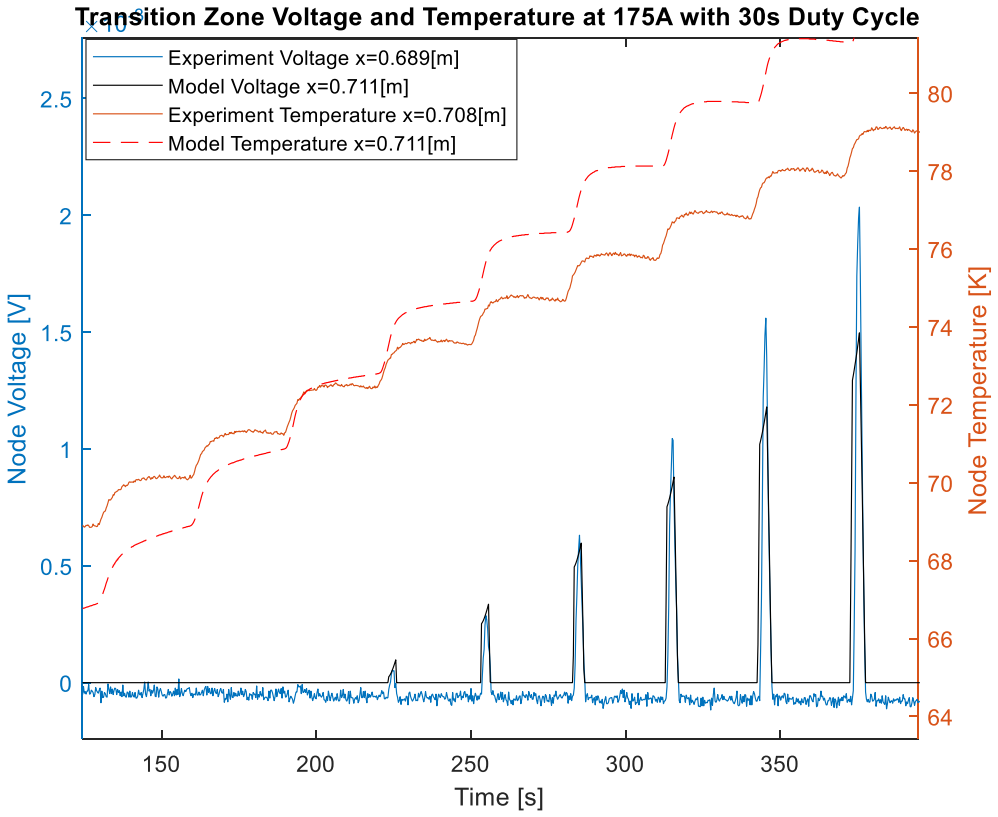

Figure 63: Voltage and temperature with respect to time for both the model and experimental data during a normal zone transition under 175 A pulse with 1 second ramp up, 1 second hold, 2 second ramp down, and 26 second relaxation time

spike is first seen. It is interesting to observe the thermal response after each current pulse. It is

clear that the thermal time constant prohibits the system from returning to its initial state after the current ramp down. With each subsequent current ramp, the resulting peak voltage increases, even for the 30-second duty cycle which provides 26 seconds of down time between ramps. To enhance the understanding of figure 63, figure 64 shows the critical current of the superconducting material plotted with respect to temperature. The lead current of 175 A is also plotted. Quadrant 1 is a rectangle that represents the fully superconducting region. The green dashed line between quadrant 1 and 2 is defined by the current sharing temperature for 175 A. This is the temperature at which the lead must stay below in order to remain fully superconducting. Quadrant 2 is a triangle that represents the superconducting part of the current sharing region, while quadrant 3 is a triangle that represents the normal part of the current

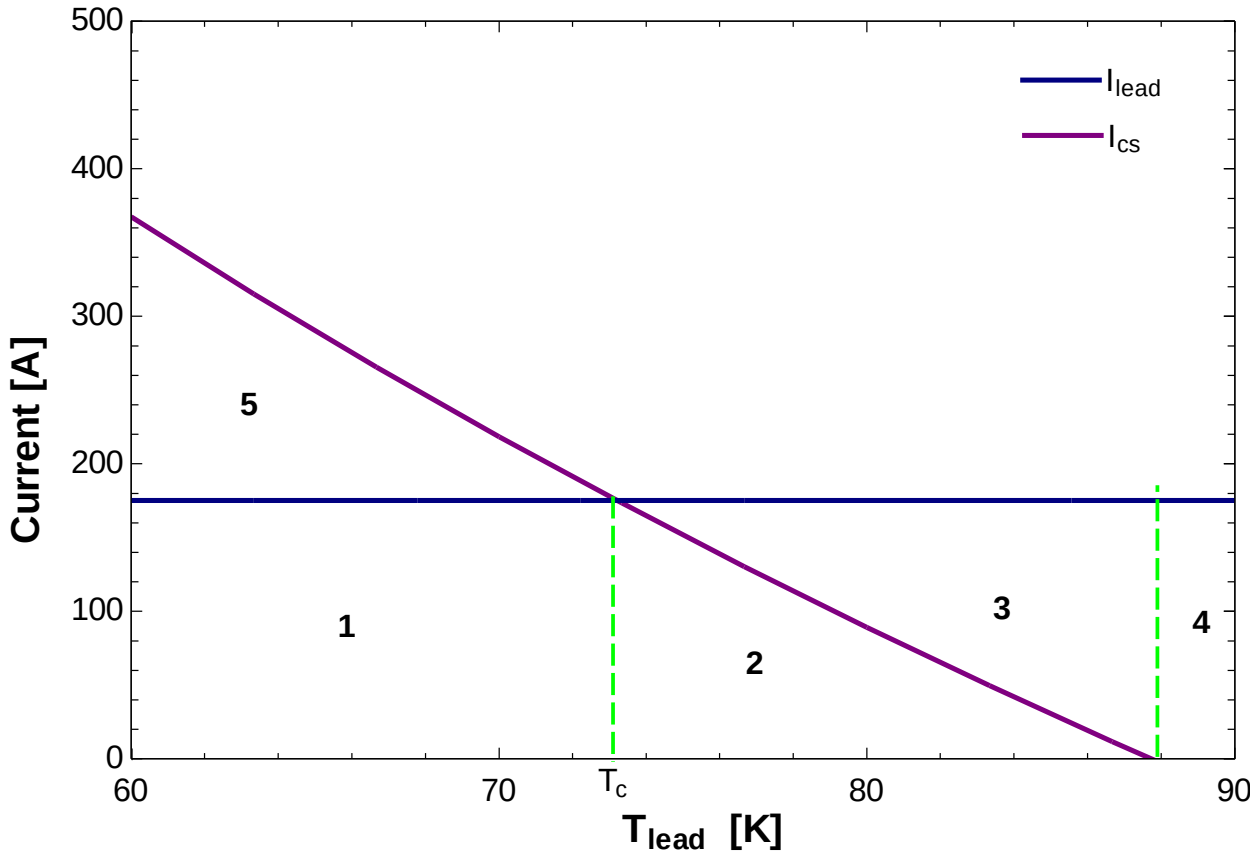

Figure 64: Critical current and lead current for 175 A plotted with respect to temperature to display the superconducting and current sharing regions

sharing region. The dashed line between quadrants 3 and 4 is defined by the critical temperature of the superconductor. Between these two temperatures the superconductor carries its critical current defined by the purple line and maintains zero resistance, while any of the operating current in excess of the critical current line is carried by the normal (copper) conductor with its temperature dependent resistance. For any positions that are warmer than the second green dashed line and are in quadrant 4 the copper carries all the current. Finally it is also useful to understand that in quadrant 5, to left of the current sharing temperature, the operating current (175 A) is less than the critical current and therefore in this temperature range, all of the current is carried by the superconductor with zero resistance.

4.3 Constant Current Comparison

The current lead experiment was also used to explore the behavior of constant current operation in order to compare the results of an RMS equivalent current to that of a pulsed current duty cycle. Figure 65 shows the experimental temperature at the warm end with respect to time for a 210 A pulse cycle with an RMS equivalent of 93.9 A in comparison to the experimental temperature with respect to time of a 96 A current draw. Both conditions are extreme current draws for the leads and would not be able to reach a quasi-steady state operation before destroying the leads. The results from this comparison gives evidence to confirm the results gained earlier in the paper with the model relating a constant current to a pulsed RMS value. A more extensive comparison between the pulsed and constant current conditions is shown in

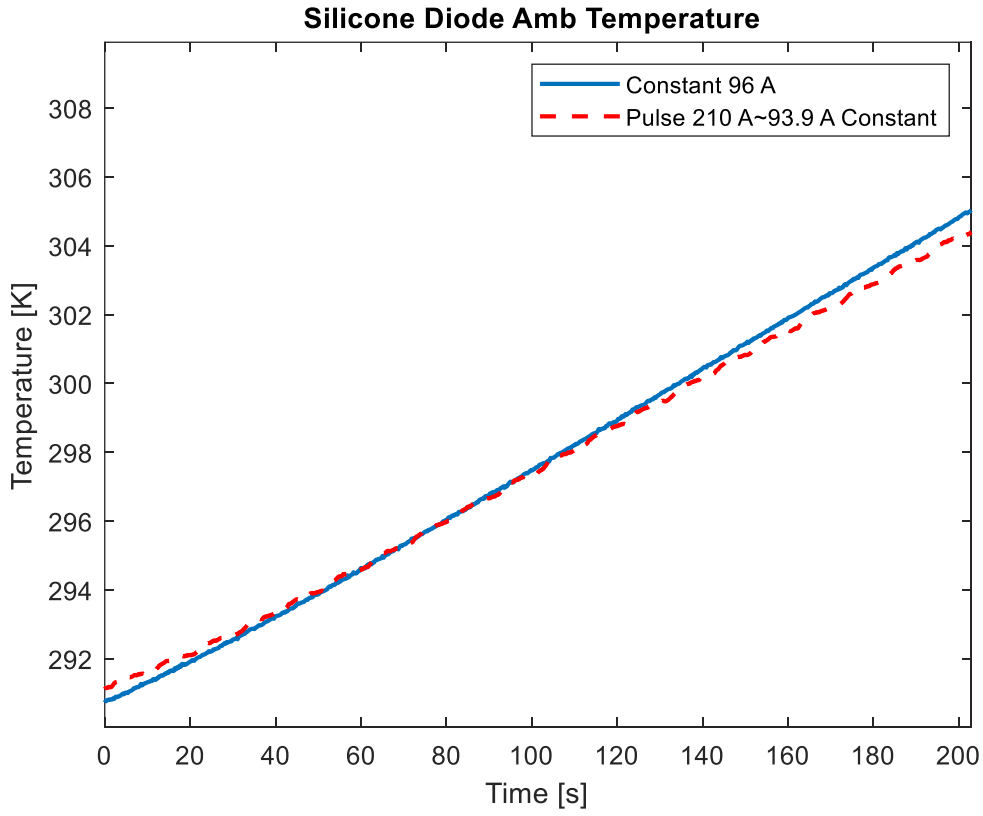

Figure 65: Comparison of the warm end temperature for 96 A constant current and a 210 A pulse with 6 seconds of relaxation time with a equivalent to 93.9 A RMS

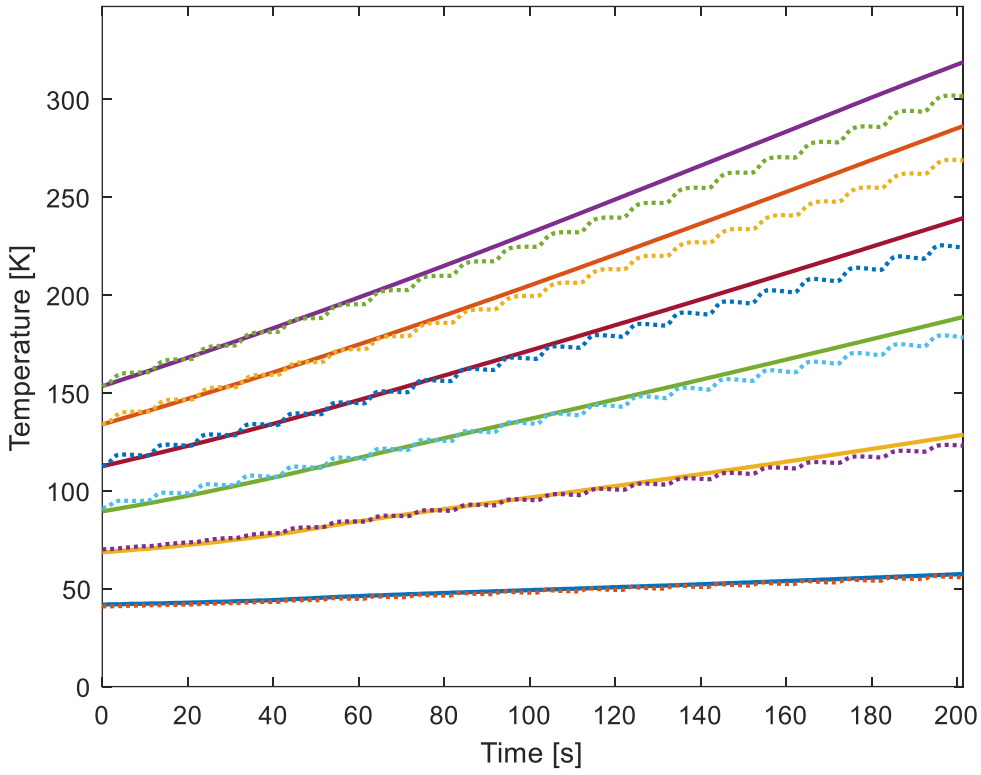

Figure 66: Comparison of the lead nodal temperature for 96 A constant current (solid lines) and a 210 A pulse with 6 seconds of relaxation time with an equivalent to 93.9 A RMS (pulsed lines)

figure 66, where the nodal temperatures of both experimental conditions are displayed. Figure 66 reflects the same agreement as shown in figure 65. Notice that both figures display a slightly larger temperature rise for the constant current case as compared to the pulsed RMS case. This would likely be due to the difference in current by approximately 2 A. Unfortunately the precision of the power supply did not allow a closer match of current at the high current levels. Looking at a lower current level where the change in temperature is not as large allows us to look at the comparison over a longer period of time. Figure 67 displays the warm end temperature for a constant current of 55 A and a 175 A pulse with an RMS equivalent current of 55.3 A. This data set reveals a very close agreement between the two conditions at the warm end for over a 15 minute period to within 1 degree. The nodal temperatures under the same condition are displayed in figure 68.

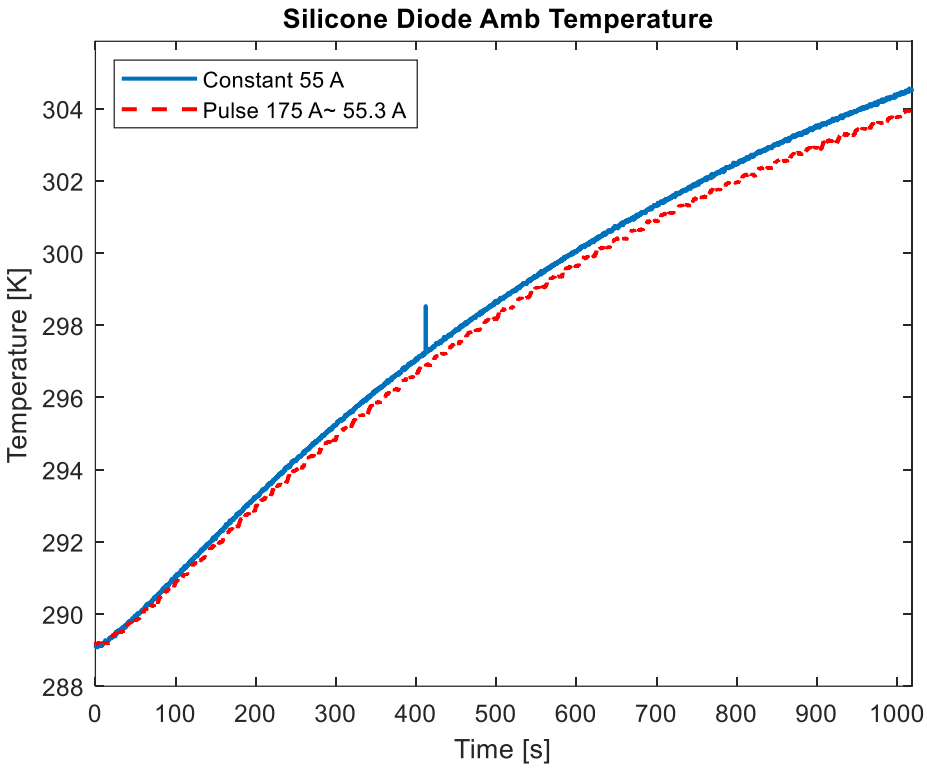

Figure 67: Warm end temperature with respect to time for 55 A constant current and a 175 A pulse with 16 seconds of relation time between pulses equivalent to 55.3 A RMS

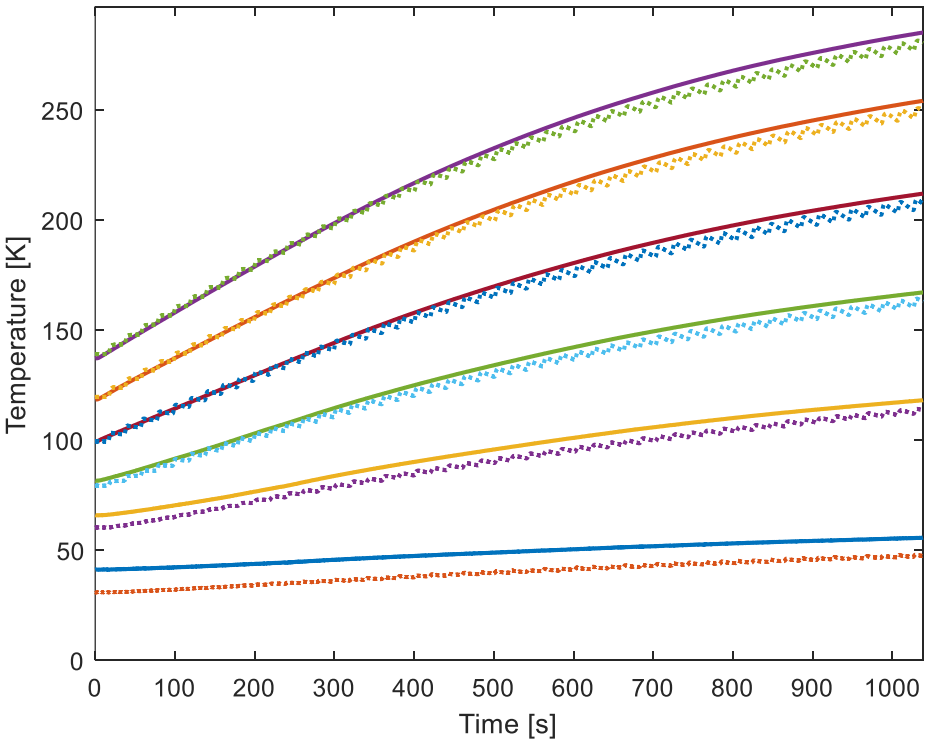

Figure 68: Current lead nodal temperature with respect to time for 55 A constant current (solid lines) and a 175 A pulse with 16 seconds of relation time between pulses equivalent to 55.3 A RMS (dotted lines)

The comparison of the nodal temperatures is in similar agreement to the warm end but the initial temperatures near the cold end differ by several degrees. In figure 69 the same nodal temperatures are seen with consistent initial temperature distribution for both data sets. The comparison shows both 31.3 A and a 70 A pulse of 31.3 A RMS approaching thermal quasi-steady state with very strong agreement after nearly 45 minutes of data collection.

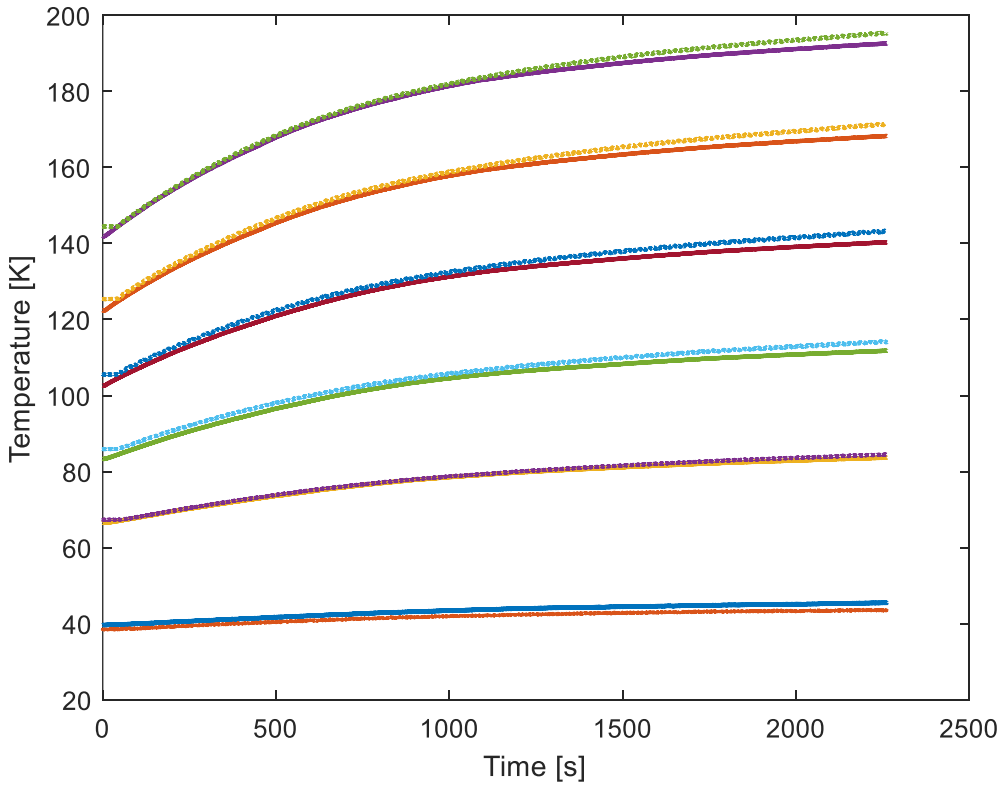

Figure 69: Current lead nodal temperature with respect to time for 31.3 A constant current (solid lines) and a 70 A pulse with 6 seconds of relation time between pulses equivalent to 31.3 A RMS (dotted lines)

4.4 Normal Zone Propagation

The voltage measurements taken at each node are useful for observing how quickly the transition zone is moving along the lead. Figure 70 displays the 5 nodal voltages on each lead (10 total) closest to the cold finger plotted with respect to time. When the constant current of 115 A is initially applied, 8 of the nodal voltage positions are superconducting. However, after only 140 seconds, all 8 nodes transition out of the superconducting state. The nodes on each lead are approximately in the same positions, and although they are on the opposite polarities of the current leads, the pair of corresponding nodes roughly transition at the same time. Also notice that there are consistent overshoots in voltage as the nodes are turning normal, a suspected cause for this phenomenon will be commented on in the future work section. Figure 71 displays a nodal voltage plot with a lower current (55 A) and reveals that the transition out of the

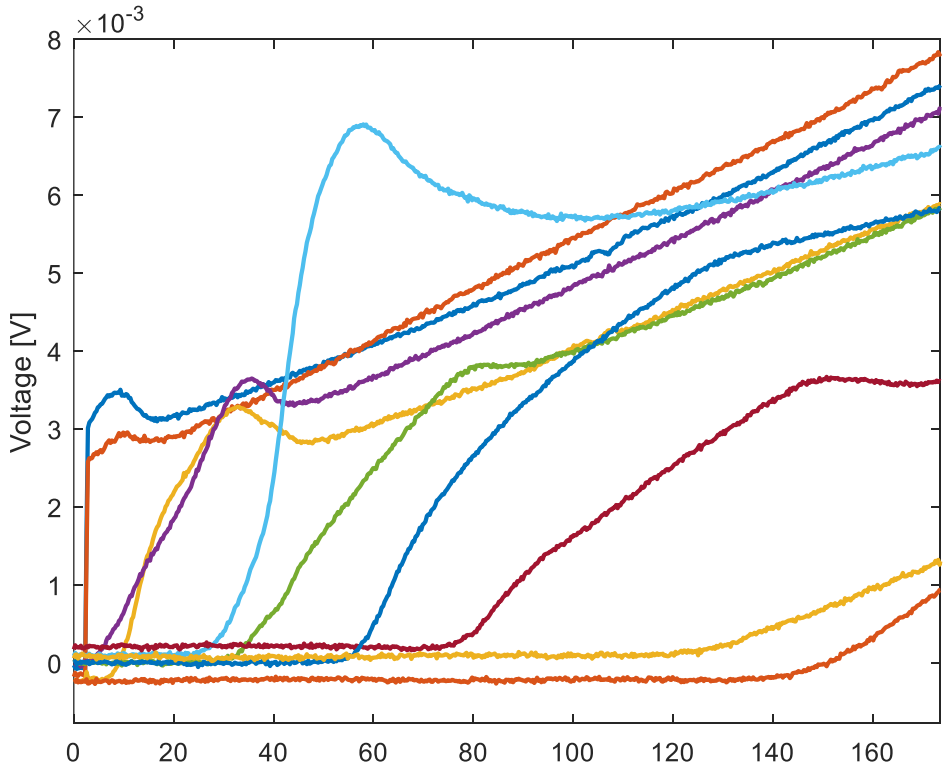

Figure 70: Nodal voltage of the current leads under a 115 A constant current condition

superconducting state takes much longer. Some nodes remain superconducting even after the quasi-steady state is reached.

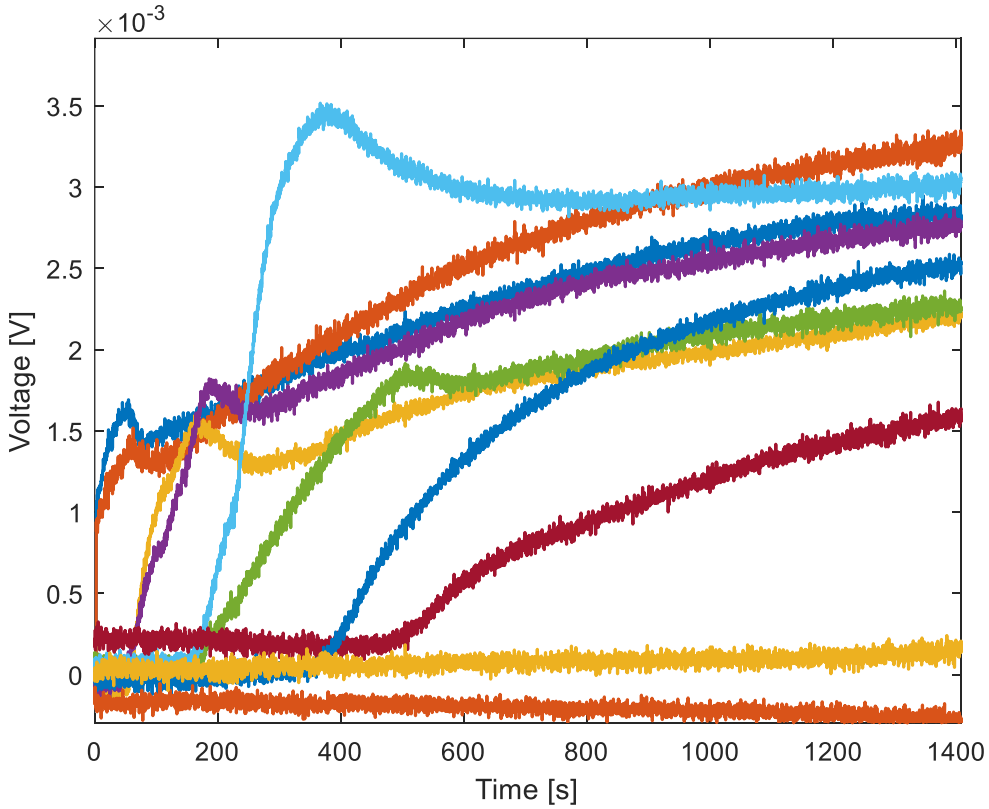

Figure 71: Nodal voltage of the current leads under a 55 A constant current condition

Here we see that only the first 6 nodes (3 on each lead) transition out of the superconducting state and two nodes (1 on each lead) appear to remain superconducting as the leads approach quasi-steady state operation. Using this information from different data sets, the length of time to reach quasi-steady state as well as the percentage of the lead that will remain superconducting for a given current condition can be determined.

4.5 Quasi-Steady State

Both the model and experiment have demonstrated that the overall thermal quasi-steady state is independent of current ramp and can be captured by an RMS equivalent. It is interesting to investigate if this time to quasi-steady state depends at all on current amplitude. A plot of nodes 16, 18, and 20 for three constant current amplitudes of 30, 50, and 60 A reveals that the thermal quasi-steady state appears to be independent of current amplitude as all data sets appear to reach approach this state after approximately 3000 seconds. The longest period of experimental data collection taken can be seen in figure 69 where the nodal positions appear they will approach thermal quasi-steady state sometime after the recorded 2300 seconds, generally agreeing with the model.

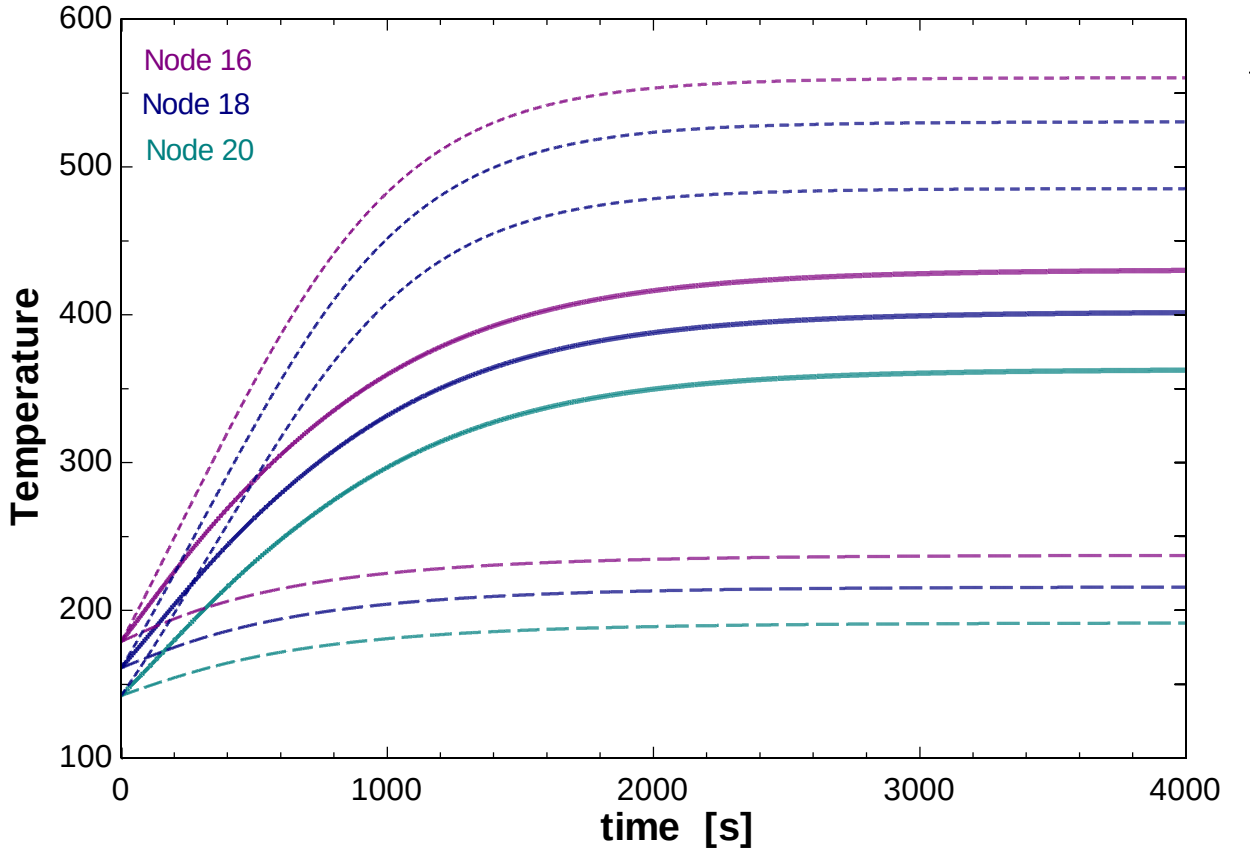

Figure 72: Model temperature with respect to time for nodes 18, 18, and 20 for 30, 50, and 60 A of constant current

4.6 RMS vs Pulse

The model on its own can be used to determine the voltage and temperature characteristics under pulsed conditions and evidence has shown that under most conditions, pulsed current cycles can be captured by a simpler RMS equivalent. However, there are operating conditions when the peak temperatures generated under the pulsed conditions far exceed the peak constant current temperatures despite capturing the quasi-steady state behavior. Figure 72 displays the data of a 55 A constant current node with the modeled temperatures associated with an rms equivalent of a 350 A cycle overlaid. Notice that despite capturing the thermal behavior, the model is unable to capture the peak temperatures due to the high current pulses. This is an example of a condition where the rms equivalent current would not be effective in representing a pulsed current

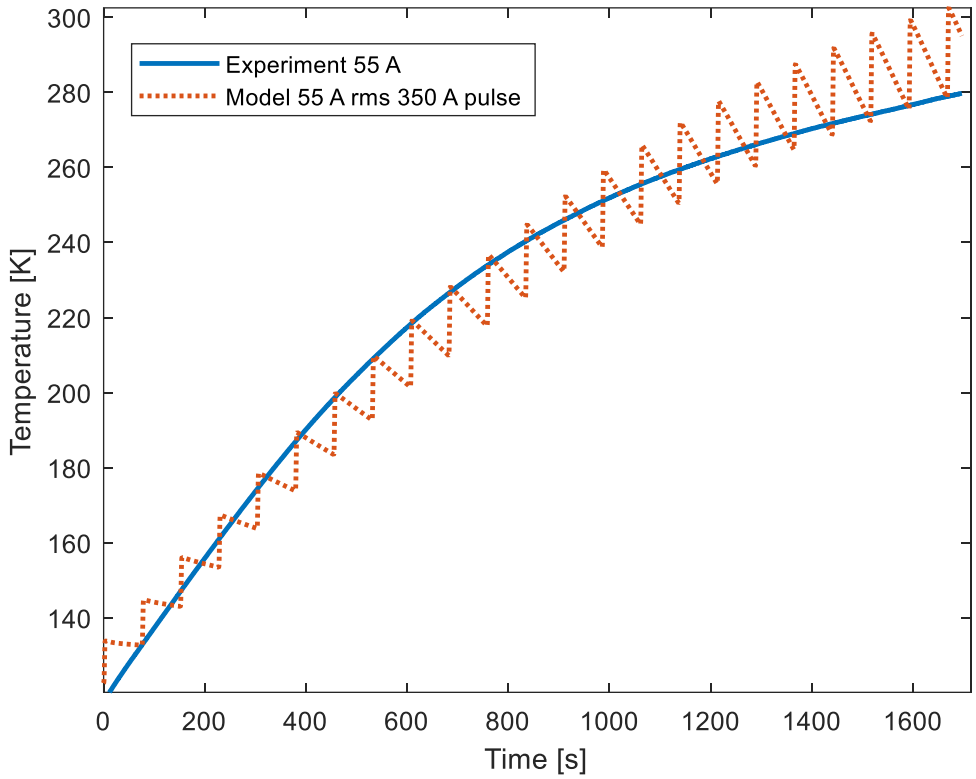

Figure 73: Constant current experimental data of one voltage node at 55 A with a 350 A pulse RMS equivalent with a 65 second relaxation time

operation. The model can be used to determine what pulse cycles are no longer within a reasonable value for capturing the peak temperatures with an rms equivalent. For example, the model can determine what percent of current downtime produces a peak temperature overshoot greater than 10%, with less than this 10 % value being called reasonable characterization.

A 1 second ramp up, 1 second hold, 1 second ramp down pulse will be defined as 2 seconds of full current. The down time can be extended and peak temperatures can be compared to the given rms equivalent at quasi-steady state. Using the we will look at a 400 A pulse with 57 second down time, giving us a 96.6% time spend at zero of maximum current following the rule above. The result of this ramp cycle plotted against the rms equivalent of 68.4 A can be seen in figure 74. The peak temperature for the rms current is 645 K while the peak temperature for the pulsed signal is 70 K. These temperatures result in an almost 8% or 55 degree under prediction

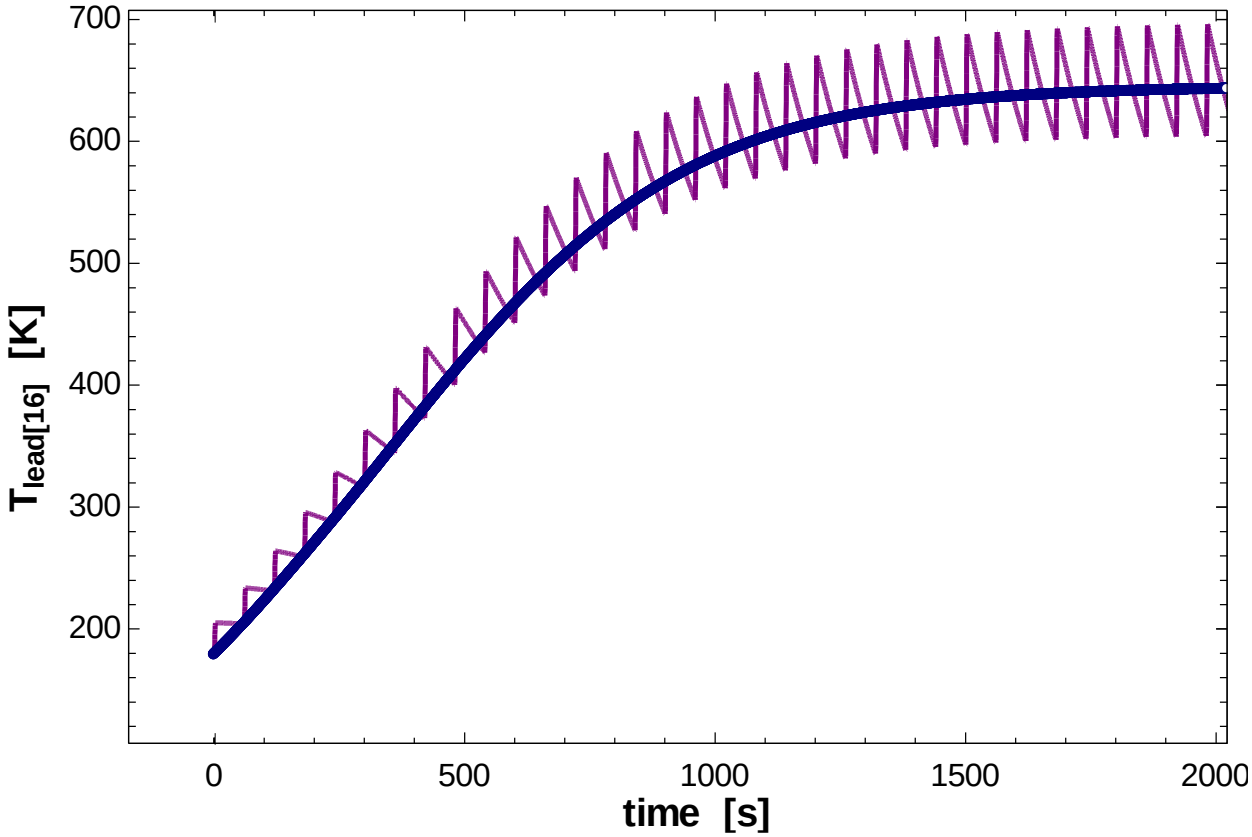

Figure 74: a 400 A pulse with 57 second down time and a 68.4 A rms equivalent

of peak temperature using the rms method. For this case the rms method was able to predict the peak temperature with 10% given 96.6% of the time spent with no current applied. The model could be used to make similar calculations and determine if an operating condition is reasonable to model as a constant current rms equivalent.

It is interesting to note that when comparing the temperature of an RMS equivalent temperature to the polynomial curve fit of the pulsed temperature that the RMS equivalent under predicts even the average temperature. This is because the RMS is a representation of power and thus the heat, but not the temperature. The existence of thermal material properties effect on the movement of heat through a material contribute to this observation. Figure 75 shows the plot of 300 A pulses with 60 second down time compared to the corresponding rms equivalent of 50 A.

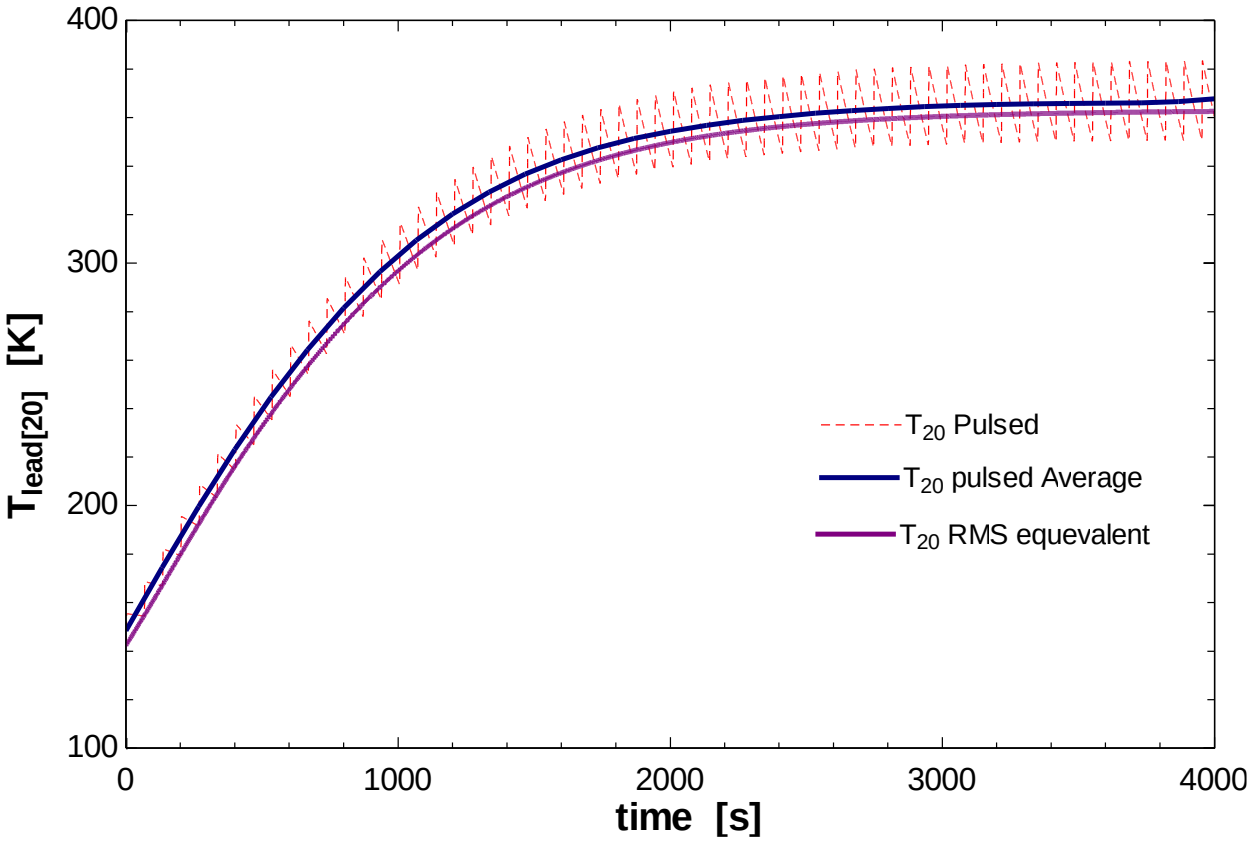

Figure 75: Temperature with respect to time for node 20 of the model for 300 A pulse with 60 second down time, a polynomial cure fit of the pulse, and an RMS equivalent of 50 A

Because peak temperatures are the biggest concern for superconducting lead damage, It is useful to correlate a relationship for the % overshoot temperature between the pulse downtime and rms equivalent. It is likely this may be dependent on more than just % downtime and current magnitude such as lead position, so two examples of current values can be looked at for one position to develop an understanding of the relationships.

5. Conclusion

The goals to develop a computer model to simulate Unique SMES operating conditions and design and build an experiment to validate the model were executed and the resulting model produced very strong agreement. Effective measurements of the nodal voltages and temperatures were taken to validate the model, and useful insight was gained in characterizations of the operating conditions with this new design including when is it reasonable to model the pulsed current lead as an rns equivalent, how long to reach thermal steady state for a given operating condition, and what characteristics does duration depend on.

The parallel superconducting current lead under the unique operating conditions was successfully modeled to capture long and short term behavior effectively. An experiment to deliver the precise measurements of the unique operation conditions was successfully developed and validated the numerical model.

Conditions where rms is a reasonable method for capturing thermal behavior or not were determined, and insight to the quasi-steady state operating conditions was gained. The normal zone propagation was observed allowing the superconducting length to be maximized. Ultimately it was found that this method for lead design could be implemented for a SMES device to allow a wider range of operating conditions, and reasonable predictions of voltage and temperature behavior can be made using a transient numerical model to aid in lead design.

6. Future Work

Further development of the model along with new data collection of the existing experiment could be done to make the transient numerical model more generalized to fit other experiments. For example, the experiment could be used to investigate a different superconducting lead capable of higher current amplitudes. A second experimental scenario would be very useful in testing the versatility of the model. Ultimately the model could be altered to fit different boundary conditions, cooling conditions current levels, materials used, and power operations.

An investigation to the significance of AC loss due to both frequency dependent eddy current losses and the effects of self-fields lowering the superconductivity could be done. Given that the change is current is at a frequency of less than 1 Hz, AC loss was not included in the model but because the experiment operates a change in current with respect to time there are going to be small losses associated with the frequency and induced field. An investigation of determining what frequency of pulse results in AC loss to be significant along with a literature review of AC current lead loss with respect to frequency could be useful.

Characterization of the RMS NZPV (Normal Zone Propagation Velocity) could be done. The NZPV is measurement of distance per unit time that can be measured experimentally by observing the movement of the normal zone. Because of the unique design of this experiment, it has the capability to capture these measurements. The expectation would be that the velocity would be dependent on current magnitude and then decrease with cycle time until approaching zero once thermal quasi-steady operation is achieved. This would be useful in comparing to existing NZPV work to see if there is correlation. Given that the copper is the primary thermal

capacitance of the cross-sectional area of the superconducting lead, the copper diffusive time constant would have an impact.

The current lead investigation presented has introduced some new questions that if answered could further enhance the model accuracy. During data collecting, an interesting recurring voltage behavior was observed in the transition zone of the leads. As each node's temperature was raised to exceed the critical temperature of the superconducting tape, as expected, the voltage measured across the node would begin to appear during a pulse of current as the node was no longer fully superconducting. The interesting observation was that during this transition period, the voltage continued to increase with each proceeding pulse and overshoot the expected voltage for the node given the temperature until a certain point after which the voltage would decrease back down before returning to the expected temperature dependent voltage. This occurrence was consistently seen in all transitioning nodes when the current was high enough and can be seen in figures 70 and 71. It was also noticed that the event was more prominent with higher amplitudes of current as well as early in the data collection when the thermal transients were most significant.

One suggested cause for this observation is current diffusion. Due to the experimental design, further investigation of current diffusion as a possible reason for this phenomena could be conducted.

Bibliography

[1] EIA, "Electricity Explained," U.S. Energy Information Administration, 30 April 2018. [Online]. Available: https://www.eia.gov/energyexplained/index.php?page=electricity_use. [Accessed March 2019].

[2] SuperPower, "Superconducting Magnetic Energy Storage (SMES)," SuperPower Inc. A Furukawa Company, 2010. [Online]. Available: http://www.superpower-inc.com/content/superconducting-magnetic-energy-storage-smes. [Accessed November 2018].

[3] W. Buckles and W. Hassenzahl, "Superconducting Magnet Energy Storage," *IEEE Power Engineering Review*, vol. 20, no. 5, pp. 16-20, 2000.

[4] A. Rose-Innes and E. Rhoderick, Introduction to Superconductivity, Oxford: Pergamon Press, 1977.

[5] Y. Iwasa, Case Studies in Superconducting Magnets, Second Edition, New York: Springer, 2009.

[6] V. Dawson, "History of Cryogenics," Cryogenic Society of America, Inc, 18 April 2008. [Online]. Available: https://cryogenicsociety.org/resources/cryo_central/history_of_cryogenics/. [Accessed October 2018].

[7] R. Barron, Cryogenic Heat Transfer, Ann Arbor, MI: Edwards Brothers, 1999.

[8] J. Weisend, "Current Leads," Cryogenic Society of America, Inc., 26 September 2011. [Online]. Available: https://cryogenicsociety.org/resources/defining_cryogenics/current_leads/. [Accessed November 2018].

[9] J. Pfotenhauer and R. Boom, "Superconductive Magnetic Energy Storage (SMES) for Electric Utilities," *Advances in Superconductivity*, pp. 33-38, 1989.

[10] R. Boom, "Superconductive Magnetic Energy Storage for Electric Utilities - A review of the 20 Year Wisconsin Program," *Proceedings of the 34th International Power Source Symposium*, vol. 34, pp. 1-4, 1990.

[11] O. Christianson, M. Mielnik, D. Hackworth, J. Pfotenhauer, F. Miller, E. Sheehan and T. Hordubav, "Pulsed HTS coil Performance," *IEEE Transactions on Applied Superconductivity*, vol. 27, no. no. 4, p. seq. no. 4603004, June 2017.

[12] E. Sheehan, J. Pfotenhauer, F. Miller and O. Christianson, "Quench Detection and Protection of an HTS Coil," *IOP Conference Series: Materials Science and Engineering,* no. 278, p. 012182, 2017.

[13] R. McFee, "Optimum Input Leads for Cryogenic Apparatus," *The Review of Scientific Instruments,* vol. 30, no. 2, pp. 98-102, 1959.

[14] K. Efferson, "Helium Vapor Cooled Current Leads," *Review of Scientific Instruments,* vol. 38, no. 12, pp. 1776-1779, 1967.

[15] Y. Buyanov and Y. Shebalin, "Current Leads to a Cryostat Working Under Short-term Load Conditions," *Cryogenics,* vol. 11, pp. 611-613, 1975.

[16] Y. Buyanov, A. Fradkov and I. Shebalin, "A Review of Current Leads for Cryogenic Devices," *Cryogenics,* vol. 4, pp. 193-200, 1975.

[17] E. Tada, Y. Takahashi, T. Ando and S. Shimamoto, "Experiences on high Current Leads for Superconducting Magnets; Seven Types from 1 kA to 30 kA," *Cryogenics,* vol. 11, p. 200, 1984.

[18] M. Wilson, Superconducting Magnets, Oxford: Clarendon Press, 1983.

[19] A. Ballarino, "High Temperature Superconducting Current Leads for the Large Hadron Collider," *IEEE Transactions on Applied Superconductivity,* vol. 9, no. 2, pp. 523-526, 1999.

[20] A. Ballarino, "HTS Current Leads: Performance Overview in Different Operating Modes," *IEEE Tansactions on Applied Superconductivity,* vol. 17, no. 2, pp. 2282-2285, 2007.

[21] A. Perin, J. Casas-Cubillos, S. Claudet, C. Darve, G. Ferlin, F. Millet and C. Parente, "Commissioning of the Cryogenics of the LHC Long Straight Sections," *AIP Conference Proceedings: Accelerator Physics,* vol. 1218, no. 1, pp. 1309-1316, 2010.

[22] D. Spiller, C. Beduz, M. Al-Mosawi, C. Friend, P. Thacker and A. Ballarino, "Design Optimization of 600A - 13kA Current Leads for the Large Hadron Collider Project at CERN," *Superconductor Science and Technology,* vol. 14, pp. 168-172, 2001.

[23] J. Hull, "High-Temperature Superconducting Current Leads," *IEEE Transactions on Applied Superconductivity,* vol. 3, no. 1, pp. 869-875, 1993.

[24] H. Chang and S. Van Sciver, "Thermodynamic Optimization of Conduction Cooled HTS Current Leads," *Cryogenics,* vol. 38, no. 7, pp. 729-736, 1998.

[25] X. Chen, J. Jin and J. Liu, "Development and Techniques of High Current Leads for HTS Device Applications," in *IEEE International Conference on Applied Superconductivity and Electromagnetic Devices,* Chengdu, 2009.

[26] L. Bromberg, P. Michael, J. Minervini and C. Miles, "Current Lead Optimization for Cryogenic Operation at Intermediate Temperaitures," *AIP Conference Proceedings, Advances in Cryogenic Engineering,* vol. 55, pp. 577-584, 2010.

[27] Y. Choi, L. Kim and H. Yang, "Development of Cryocooled Binary Current Lead in Low Temperature Superconducting Magnet System," *AIP Conference Proceedings,* vol. 55, pp. 553-560, 2010.

[28] S. Yang and J. Pfotenhauer, "Optimization of the Intercept Temperature for High Temperature Superconducting Current Lead," *Advances in Cryogenic Engineering,* vol. 41, pp. 567-572, 1996.

[29] J. Hull, "High-Temperature Superconducting Current Leads For Cryogenic Apparatus," *Proceedings of the 24th Intersociety Energy Conversion Engineering Conference,* vol. 24, pp. 459-464, 1989.

[30] J. Wu, J. Dederer, P. Eckels and S. Singh, "Design and Testing of a High Temperature Superconducting Current Lead," *IEEE Transactions on Magnetics,* vol. 27, no. 2, pp. 1861-1865, 1991.

[31] Q. Wang, D. Jeong, S. Oh and H. Kim, "Design of Bi-based Superconducting Current leads for SMES," *IEEE Transactions on Applied SUperconductivity,* vol. 9, no. 2, pp. 499-502, 1999.

[32] A. Gavrilin, V. Keilin and I. Kovalev, "Optimized HTS Current Leads," *IEEE Transactions on Applied Superconductivity,* vol. 9, no. 2, pp. 531-534, 1999.

[33] T. Isono, K. Kawano, K. Hamada, K. Matsui, Y. Nunoya, E. Hara, T. Kato, T. Ando and K. Okuno, "Test Results of 60 - kA HTS Current Lead for Fusion Application," *Elsevier,* pp. 1219-1224, 2003.

[34] Y. Iwasa and H. Lee, "High-Temperature Superconducting Current Lead Incorporating Operation in the Current-Sharing Mode," *Elsevier: Cryogenics,* vol. 40, pp. 209-219, 2000.

[35] T. Fujii, S. Fukuda and T. Kawahara, "Evaluation of Thermoelectric Properties of Bite Alloys for the Optimization of Gas-Cooled Peltier Current Leads," *AIP Conference Proceedings,* vol. 1218, no. 1, pp. 561-568, 2010.

[36] A. Ballarino, "Large-Capacity Current Leads," *Elsevier: Physica C,* vol. 468, pp. 2143-2148, 2008.

[37] Y. Park, W. Lee, H. Kim, Y. Chung, Y. Yoon and T. Ko, "Evaluation of Electrical and Thermal Properties of Stacked YBCO Coated Conductors for Current Lead Application," *IEEE Transactions on Applied Superconductivity,* vol. 25, no. 3, p. 4802604, 2015.

[38] B. Glowacki, A. Gilewski, K. Rogacki and A. Kursumovic, "Characterisation of an Optimised High Current MgO/Bi2Sr2CaCu2O8.21 Composite Conductor Using Pulsed Transport Currents with Pulsed Magnetic Fields," *Elsevier Science: Physica C,* pp. 205-210, 2003.

[39] S. Jeong and S. In, "Investigation on Vapor-Cooled Current Leads Operating in a Pulse Mode," *Elsevier: Cryogenics,* vol. 44, pp. 241-248, 2004.

[40] R. Wesche, "Design of High-Temperature Superconducting Current Leads for ITER," *ELSEVIER: Fusion Engineering and Design,* vol. 82, pp. 1385-1390, 2007.

[41] S. Klein, "EES - Engineering Equation Solver, Version 10.570," F-Chart Software, 7 January 2019. [Online]. Available: http://fchart.com.

[42] J. Pfotenhauer, O. Lokken and P. Gifford, "Performance of a Twin Cold Finger Gifford-McMahon Cryocooler," *Proceedings of the Sixteenth International Cryogenic Engineering Conference / International Cryogenic Materials Conference,* vol. 16, pp. 363-366, 1997.

[43] SuperPower-Furukawa, *2G HTS Wire Specifications,* SuperPower inc.: http://www.superpowerinc.com, 2017.

[44] G. Nellis and S. Klein, Heat Transfer, New York, NY: Cambridge University Press, 2009.

[45] N. Instruments, *SCXI Chassis User Manual,* Austin: National Instruments Corporation, 2006.

[46] N. Instruments, *SCXI-1100 User Manual : 32-Channel Differential Multiplexer/Amplifier Module for Signal Conditioning,* Austin: National Instruments Corperation , 1994.

[47] N. Instruments, *SCXI-1300/1301 Terminal Block Installation Guide,* Austin: National Instruments Corperation, 2000.

[48] Omega, *Revised Thermocouple Reference Tables: Type E,* Stamford: www.Omega.com.

[49] Lakeshore, *Sensors: Silicond Diodes: DT-400 Series Silicon Diodes,* www.Lakeshore.com: Lake Shore Cryotronics Inc.

[50] K. Technologies, *Keysight model 6681A GPIB DC Power Supply: Operating Guide,* New Jersey: Keysight Technologies, 2014.

[51] S. Interconnect, "Smith Interconnect Board Test Fixture Probes," Spiths Interconnect, 2019. [Online]. Available: https://www.smithsinterconnect.com/products/board-test-fixture-probes/. [Accessed 2019].

[52] SuperPower, "SuperPower 2G HTS Wire Specifications," SuperPower Inc. A Furukawa Company, 2012. [Online]. Available: http://www.superpower-

inc.com/system/files/SP_2G+Wire+Spec+Sheet_for+web_2012FEC_v2_1.pdf. [Accessed 2019].

[53] J. Hull, "High-Temperature Superconducting Current Leads," *IEEE Transactions on Applied Superconductivity*, vol. 3, no. 1, pp. 869-875, 1993.

[54] D. Prananto, "Simpliphy: Superconductivity," 6 May 2012. [Online]. Available: https://simpliphy.org/tag/superconductivity/. [Accessed 10 January 2019].

[55] M. Industries, "Mosaic Documentation Web: Type E Thermocouple Calibration," Mosaic Industries, 23 April 2019. [Online]. Available: http://www.mosaic-industries.com/embedded-systems/microcontroller-projects/temperature-measurement/thermocouple/type-e-calibration-table.

[56] S. Power, "SuperPower 2G HTS Wire," Furukawa Electric Group, 2018. [Online]. Available: http://www.superpower-inc.com/. [Accessed 2018].

Appendix

EES MODEL CODE

```
"Tyler Hanzlik and Evan Sheehan"

"Numerical Model of Pulsed, Superconducting Current Lead"
//_____
_____
//---------- Electrical Section ----------
//_____
_____
//Current Cycle Fuction
Function
currentcycle(CycleLocation,A,B,C,RampUpTime,RampDownTime,I_min,I_rise)
        "Function looks at where in the duty cycle a given time is, and assigns the proper current to
that time"
    If (CycleLocation<=A)
Then
        "If the ramp is going up"
    Current:=I_min+(CycleLocation/RampUpTime)*I_rise
        "Resulting current is linearly proportional to elapsed ramp up time, up to the max current"

    Else
    If (A<CycleLocation) AND (CycleLocation<=B)
Then
        "If the ramp is being held constant"
    Current:=I_min+I_rise
        "Current is held at its max value"

    Else
    If (B<CycleLocation) AND (CycleLocation<=C)
Then
        "If the ramp is going down"
    Current:=I_min+I_rise-((CycleLocation-
B)/RampDownTime)*I_rise                    "Resulting current is linearly proportional
to elapsed ramp down time, back to zero current"

    Else
    Current:=I_min
        "Current is zero between pulses"
    Endif
    Endif
    Endif
currentcycle=Current;
        "Function outputs the current value for each time to be used by the main program"
End
//_____
_____
//Resistance Function
```

```
Function
resistancevalue(i,I_cs,I_value,rho_e_lead,DELTAx_lead,A_c_lead)
        "Function determines effective resistance of each element"
    If (I_cs=0)
Then
        "If critical current = 0: Fully normal"
    Resistance:=rho_e_lead*DELTAx_lead/A_c_lead
        "Resistance is that of a regular normal material"

    Else
    If (I_cs>I_value)
Then
        "If critical current is greater than supplied current: All current carried in superconductor"
    Resistance:=0
        "Resistance is 0"

    Else
    If (0<I_cs) AND (I_cs<I_value)
Then
        "If critical current is nonzero (partially superconducting) but less than supplied current, excess is carried in normal material"
    Resistance:=rho_e_lead*DELTAx_lead/A_c_lead*(I_value-
I_cs)/I_value                                   "Resistance has a scaling factor. As I_value ---> I_cs, R ---> 0. As I_value >>> I_cs, scaling factor goes to 1. Note that I_cs will never be zero due to logic, so R never goes to infinity, and it never exceeds I_value so it also never goes negative"
    Endif
    Endif
    Endif
resistancevalue=Resistance;
End
//_____________________________________________________________________________
_____________
//Cycle Characteristics (Use these values to vary the current duty cycle and amplitude)
RampUpTime=1
        "Duration of ramp up"
HoldOnTime=1
        "Duration of hold time at max current"
RampDownTime=2
        "Duration of ramp down"
HoldOffTime=6
        "Time between ramps"
I_min=0
        "Minimum current, usually zero"
I_rise=210
        "Current increase during ramp. Usually maximum current if minimum current is zero"
I_value=currentcycle(CycleLocation,A,B,C,RampUpTime,RampDownTime,I_min,I_rise)
        "Value of current for a given point in ramp cycle, output by function CurrentCycle"
//_____________________________________________________________________________
_____________
"Times of Cycle Transitions"
A=RampUpTime
        "End of ramp up"
B=RampUpTime+HoldOnTime
        "End of hold"
C=RampUpTime+HoldOnTime+RampDownTime
        "End of ramp down"
```

```
CycleDuration=RampUpTime+HoldOnTime+RampDownTime+HoldOffTime
        "Total time to complete one ramp cycle"
CycleNumber=1+trunc(time/CycleDuration)
        "Assigns a number to each ramp cycle, starting from 1"
CycleLocation=CycleDuration+time-
CycleNumber*CycleDuration                    "Determines what time it is each current
cycle, from 0 sec to the cycle duration. Fed back into CurrentCycle Function. time is the integration
variable"

"Equivalent RMS current of cycle"
I_1_squared_RMS=RampUpTime/(3*CycleDuration)*I_rise^2
        "The 3 comes from a time integration of (1/Period)*I_rise^2*(time/ramptime)^2"
I_2_squared_RMS=HoldOnTime/CycleDuration*I_rise^2
I_3_squared_RMS=RampDownTime/(3*CycleDuration)*I_rise^2
        "The 3 comes from a time integration of (1/Period)*I_rise^2*(time/ramptime)^2"
I_RMS=sqrt(I_1_squared_RMS+I_2_squared_RMS+I_3_squared_RMS)
        "http://masteringelectronicsdesign.com/how-to-derive-the-rms-value-of-a-trapezoidal-
waveform/ Equivalent constant current (RMS value) of trapezoidal
waveform"
//_____________________________________________________________________________
_____________
"Critical Surface"
"Logarithmic Equation Coefficients"
aa=-967.4
bb=4328.3

"Current Sharing"
Duplicate i=1,N
    I_cs_curve[i]=aa*ln(T_lead[i]/(1
[K]))+bb
        "Current for a given node temperature at which current sharing begins. Divided by 1 [K] for
dimensionless log arguement"
    I_cs[i]=IF
(I_cs_curve[i],0,0,0,I_cs_curve[i])
        "IF statement returns a current sharing current of 0 if I_cs is negative or 0. Otherwise, returns
whatever current the critical surface defines"
    I_norm[i]=IF (I_value,I_cs[i],0,(I_value-I_cs[i]),(I_value-
I_cs[i]))                    "IF statement sets normal current either
equal to zero if below the current sharing temperature or equal to the excess current above or equal to Ic"
End
//_____________________________________________________________________________
_____________
//Time and Space Distribution (Use these values to vary the simulation space and time variables)
t_sim=400
        "Simulation time"
Interval=0.25
        "Integration time interval"
"Parameters"
N=30
        "Number of nodes"
L_lead=.7647
[m]                                    "Current lead length"
//_____________________________________________________________________________
_____________
//Lead Dimensions
```

```
D_o=0.125*convert(in,m)
            "Outer tube diameter"
th=0.03*convert(in,m)
            "Tube wall thickness"
D_i=D_o-
2*th
            "Inner tube diameter"
A_c_lead=pi/4*(D_o^2-
D_i^2)
            "Cross sectional area of tube"
{A_s_lead_i=pi*D_o*DELTAx_lead
            "External surface area of tube"}
A_c_lead=pi*D_equiv^2/4
            "Calculates equivalent diameter of tube if it were solid rod instead"
d_steel = .6*convert(in,m)
A_c_steel = pi*d_steel^2/4
//_____________________________________________________________________________
_____________
"Space Grid"
Duplicate i=1,N
    x[i]=(i-1)*L_lead/(N-
1)                                                  "Position of each node"
End
DELTAx_lead=L_lead/(N-
1)                                                  "Distance between each node"
//_____________________________________________________________________________
_____________
//------------------------------------------------------------------- Thermal Section ----------------------------------------
-------------------------
//_____________________________________________________________________________
_____________
T_H=295
[K]                                                 "Hot end temperature"

"Material Properties"
Duplicate i=1,N
    rho_e_lead[i]=electricalresistivity(Copper,
T=T_lead[i])
    k_lead[i]=conductivity(Copper, T=T_lead[i])
    rho_lead[i]=density(Copper, T=T_lead[i])
    c_lead[i]=cp(Copper, T=T_lead[i])
    alpha[i]=k_lead[i]/(rho_lead[i]*c_lead[i])

    rho_e_steel[i]=electricalresistivity(Stainless_AISI304,
T=T_lead[i])
    k_steel[i]=conductivity(Stainless_AISI304, T=T_lead[i])
    rho_steel[i]=density(Stainless_AISI304, T=T_lead[i])
    c_steel[i]=cp(Stainless_AISI304, T=T_lead[i])
End

//_____________________________________________________________________________
_____________
//Conduction through cables
M = 10
Duplicate i=1,M
    rho_e_c[i]=electricalresistivity(Copper, T=Tc[i])
```

```
    k_c[i]=conductivity(Copper, T=Tc[i])
    rho_c[i]=density(Copper, T=Tc[i])
    c_c[i]=cp(Copper, T=Tc[i])
    {alpha_c[i]=k_c[i]/(rho_c[i]*c_c[i])}
End
x_c[1] = 0
Duplicate i = 2,M
    X_c[i] = x_c[i-1] + DeltX_c
End
C_D = .0045 [m]
C_D_O = .015 [m]
Ac_c = pi*(C_D/2)^2
DELTX_c = .65 [m]
Cab_SA = DELTX_c*pi*C_D_O
//_____
_____
//Radiation Term
e1 =.09
e2 =.09
e3 =  .017
N_layers = 30
CF_D = 6.8 [in]
Vo_A = 10[in^2]
R_vac = (5.834/2)*convert(in,m)
L_vac = 19*convert(in,m)
SA_dewer = L_vac*2*pi*R_vac+2*pi*R_vac^2
SA_no_MLI = ((2*pi*(CF_D/2)^2)+Vo_A)*convert(in^2,m^2)
epsilon_mli = 1/((1/e1)+(1/e2)-1+N_layers*((2/e3)-1))
epsilon_noMLI = 1
ratio = SA_no_MLI/SA_dewer
epsilon = ratio*epsilon_noMLI + (1-ratio)*epsilon_mli
//_____
_____
//Boundary Conditions
//Twin finger cryocooler cooling capacity curve polynomial coefficients
aaa=9*10^(-5)
bbb=0.0406
ccc=6.419
ddd=165.23
Q_dot_ini=aaa*T_lead_ini[N]^3-bbb*T_lead_ini[N]^2+ccc*T_lead_ini[N]-ddd
Q_dot=aaa*T_lead[N]^3-bbb*T_lead[N]^2+ccc*T_lead[N]-
ddd                                                    "Twin finger cryocooler cooling capacity
curve"
A_C_cf = pi*(.04[m]/2)^2
DELTAx_CF = .001 [m]
//_____
_____
//Steady State Energy Balance
//-----------------------------------------------------------------------------------------------------------------------
-------------------------
//Power cable BC
T_H= Tc[1]
Tc_ini[1] = Tc[1]

Duplicate i=2,(M-1)
    0 = k_c[i]*Ac_c/DELTX_c*(Tc_ini[i-1]-2*Tc_ini[i]+Tc_ini[i+1])+((T_H-Tc_ini[i])*h_bar_term*cab_SA)
```

```
End
0 = k_c[10]*Ac_c/DELTX_c*(Tc_ini[9]-2*Tc_ini[10]+T_lead_ini[1])+((T_H-Tc_ini[10])*h_bar_term*cab_SA)
0 = k_lead[1]*A_C_lead/DELTAx_lead*(Tc_ini[10]-2*T_lead_ini[1]+T_lead_ini[2])+((T_H-
T_lead_ini[1])*h_bar_term*term_SA)
//Tc_ini[5] = T_lead_ini[1]
//_____________________________________________________________________________________
_________
//S.S. Energy Balance first Node: 0 = conductionRHS + infinite fin convection + radaition (storage = 0)
{0 = ((((K_lead[1]+K_lead[2])/2)*A_c_lead*2)/DELTAx_lead)*(-
T_lead_ini[1]+T_lead_ini[2])+(epsilon*sigma#*pi*D_o*(DELTAx_lead/2)*(T_H^4-
T_lead_ini[1]^4))+((sqrt(K_lead[1]*h_bar_term*A_c_term*per_term))*(-T_lead_ini[1]+T_H))}

//S.S. Energy Balance middle nodes: 0 = conductionLHS + conductionRHS + radiation (storage = 0)
Duplicate i=2,(N-1)
    0=(k_lead[i]*A_c_lead*(T_lead_ini[i-1]-
2*T_lead_ini[i]+T_lead_ini[i+1])/DELTAx_lead)+(epsilon*sigma#*pi*D_o*DELTAx_lead*(T_H^4-
T_lead_ini[i]^4))
End
//S.S. Energy Balance Last Node: Q_dot_ini = ConductionLHS + Radiation (storage = 0)
 Q_dot_ini = 2*(((((K_lead[N]+K_lead[N-1])/2)*A_c_lead*2)/DELTAx_lead)*(T_lead_ini[N-1]-T_lead_ini[N])
+ (epsilon*sigma#*pi*D_o*(DELTAx_lead/2)*(T_H^4-T_lead_ini[N]^4)))
//_____________________________________________________________________________________
_______
//Transient Equations of State Using EES integral function
//-------------------------------------------------------------------------------------------------------------------
--------------------
//Transient power cable
Duplicate i=2,(M-1)
    DT_c\dt[i] = (1/(rho_c[i]*c_c[i]*DELTx_c*Ac_c))*(k_c[i]*Ac_c/DELTX_c*(Tc[i-1]-
2*Tc[i]+Tc[i+1]){+((T_H-Tc[i])*h_bar_term*cab_SA)})
End
DT_c\dt[10] = (1/(rho_c[10]*c_c[10]*DELTx_c*Ac_c))*(k_c[10]*Ac_c/DELTX_c*(Tc[9]-
2*Tc[10]+T_lead[1])+((T_H-Tc[10])*h_bar_term*cab_SA))
DT_lead\dt[1] = (1/(DELTAx_lead*(rho_lead[1]*A_c_term*c_lead[1]+rho_steel[1]*c_steel[1]*a_c_steel)))*(
k_lead[1]*A_C_lead/DELTAx_lead*(Tc[10]-
2*T_lead[1]+T_lead[2])+((I_norm[1]^2*rho_e_lead[1]*DELTAx_lead)/A_c_lead)+((T_H-
T_lead[1])*h_bar_term*term_SA))

//Transient Energy Balance first Node: DT/dt = 1/storage(ConductionRHS + infinite fin convection +
radiation + generation)
{dT_lead\dt[1] =
(1/(rho_lead[1]*DELTAx_lead*A_c_term*c_lead[1]))*((((I_norm[1]^2*rho_e_lead[1]*DELTAx_lead)/(2*A_c_
term))+((((K_lead[1]+K_lead[2])/2)*A_c_lead*2)/DELTAx_lead*(-
T_lead[1]+T_lead[2]))+(epsilon*sigma#*pi*D_o*(DELTAx_lead/2)*(T_H^4-
T_lead[1]^4))+(sqrt(K_lead[1]*h_bar_term*A_c_term*per_term)*(-T_lead[1]+T_H)))}

//_____________________________________________________________________________________
_____
//Transient Energy Balance middle nodes: DT/dt = 1/storage(ConductionLHS + ConductionRHS +
radiation + generation)
Duplicate i=2,(N-1)
    dT_lead\dt[i]=(1/(rho_lead[i]*DELTAx_lead*A_c_lead*c_lead[i]))*(((I_norm[i]^2*rho_e_lead[i]*DELTAx_
lead)/A_c_lead)+(k_lead[i]*A_c_lead*(T_lead[i-1]-
2*T_lead[i]+T_lead[i+1])/DELTAx_lead)+(epsilon*sigma#*pi*D_o*DELTAx_lead*(T_H^4-T_lead[i]^4)))
End
```

```
//Transient Energy Balance Last Node: DT/dt = 1/storage(-q_dot + conductionLHS + radiation +
generation)
dT_lead\dt[N]= (1/(rho_lead[N]*DELTAx_cf*A_c_cf*c_lead[N]))*((-
Q_dot/2)+(I_norm[N]^2*rho_e_lead[N]*DELTAx_lead)/(2*A_c_lead)+((((K_lead[N]+K_lead[N-
1])/2)*A_c_lead*2)/DELTAx_lead)*(T_lead[N-1]-T_lead[N]) +
(epsilon*sigma#*pi*D_o*(DELTAx_lead/2)*(T_H^4-T_lead[N]^4)))

//_____
_______
{T_lead_ini[N]=T_lead[N]}
"Heat load"
{Q_dot=2*k_lead[N-1]*A_c_lead*(T_lead[N-1]-
T_lead[N])/DELTAx_lead}                                    "NOTE: multiplied by a factor of 2 for
having both a positive and negative current lead"
//_____
_______
"Integration to determine subsequet temperatures for each node"
Duplicate i=1,(N)
    T_lead[i]=T_lead_ini[i]+integral(dT_lead\dt[i],time,0,t_sim,Interval)
End
Duplicate i=2,(M)
    Tc[i]=Tc_ini[i]+integral(dT_c\dt[i],time,0,t_sim,Interval)
End
//_____
_______
"Diffusive time constant estimate based on each node thermal diffusivity"
Duplicate i=1,N
    tau_diff[i]=(L_lead/2)^2/(4*alpha[i])
End

"Resistance of each element"
Duplicate i=1,N
    Resistance[i]=resistancevalue(i,I_cs[i],I_value,rho_e_lead[i],DELTAx_lead,A_c_lead)
End
R_total=2*sum(Resistance[i],
i=1,N)
            "Sum of element resistances gives total resistance. Note factor of 2 for two leads"
{Voltage=I_value*R_total
            "Voltage required to drive current profile through resistance. NOTE: does not include inductive
voltages"
 }
Duplicate i=1,N

Voltage[i]=I_value*Resistance[i]
            "Voltage required to drive current profile through resistance. NOTE: does not include inductive
voltages"
    End
    Volt_total = 2*sum(Voltage[i], i=1,N)


"Biot number to rule out Residual gas conduction"
RGC = .001471 [w/m-k]
L_rad = 1*convert(in,m)
RGC_ini = (RGC*pi*D_o*DELTAx_lead*(T_H-T_lead_ini[30]))/L_rad
rad_ini = (.7*sigma#*pi*D_o*DELTAx_lead*(T_H^4-T_lead_ini[30]^4))
Biot_RGC = RGC_ini/Rad_ini
```

```
"Biot number to rule out instrumentation wire conduction"
D_vtaps = .011*convert(inch,m)
A_c_vtaps = pi/4*(D_Vtaps^2)
L_vtaps = .5 [m]
cond_inst = (T_H-T_lead_ini[30])*A_c_vtaps*k_lead[30]/L_vtaps
cond_leads= (T_lead_ini[29]-T_lead_ini[30])*A_c_lead*k_lead[30]/DELTAx_lead
biot_inst = cond_inst/cond_leads

//_____
_____
//Convection Term (Terminal outside the
vacuum)
            Infinite Fin Boundry Variables
h_bar_term = 5 [W/m^2-
k]
"https://www.engineeringtoolbox.com/convective-heat-transfer-d_430.html"
term_H = 0.0125 [m]
term_L = .04 [m]
term_w = .03 [m]
term_SA = (term_H*term_L*2)+(term_w*term_H*2)
A_c_term = (term_w*term_H)
//per_term = 2*(term_w+term_H)
                                                "Assumed warm end temp constant at ambient"

//_____
_____
//Note AC loss effects from the pulse are neglected



$Arrays On
$IntegralTable time:
Interval,CycleNumber,CycleLocation,I_value,I_norm[1..N],I_cs[1..N],T_lead[1..N],Tc[1..M],Q_dot,tau_diff[
1..N],Resistance[1..N],R_total,Voltage[1..N],Volt_total

$Savetable 'Integral Table' 'I:\data\EES\table.lvm'



//
```

Code for Matlab plots and analysis

```
%%%%%%%%%%%%%%%%%%%%%%%%%%%%%%%%%%%%%%%%%%%%%%%%%%%%%%%%%%%%%%%%%%%%%%%%%%%%
%%%%%%%% Current Lead Analysis EES overlay With Constant Current  %%%%%%%%
%%%%%%%%%%%%%%%%%%%%%%%%%%%%%%%%%%%%%%%%%%%%%%%%%%%%%%%%%%%%%%%%%%%%%%%%%%%%

%% Measured values
TempPos = [.4,2.3,4.3,6.2,8.15,9.9,.45,2.65,4.65,6.8,8.95,10.7];   %[in]
Position of each thermocouple probe

IntoM = .0254;
TempPosM = TempPos*IntoM ;
TempM = fliplr(TempPosM);
TempMm = .48+TempM;
VoltPosCentr =
[10.035,9.05,8.06,7.065,6.0625,5.0525,4.06,3.0625,2.06,1.045,8.9025,7.925,6.9
325,5.96,4.975,3.9675,2.975,1.9675,.975];   %center position of each voltage
tap pair
VoltPosM = .48 + (VoltPosCentr*IntoM);
VoltDelta =
[1.01,.96,1.02,.97,1.035,.985,1,.995,1.01,1.02,.985,.97,1.015,.93,1.04,.975,1
.01,1.005,.98];    %delta X of each voltage pair
p1 = 11;
%% Data Time Alignment

%Pulsed Data
z = 6000;
w = 260 ;
v = z+w-1;
trialNumber = [45];
stringTrial = {''};

%Constant Current Data
z2 = 6000;
w2 = 1;
v2 = z2+w2-1;
trialNumber2 = [45];
stringTrial2 = {''};

%% Data File References

%trialNumber = [10,18,12,13,15,16,17,19,22,26,27,28,29,30,35];
%stringTrial = {'45','70','95','115','140', '175', '210','70 15 duty','70
pulse','70 20 duty','70 25 duty','175 pulse','175','175 20 duty','175 30
duty'};

%10:z=4500  45 Amp
%18:z=8000  70 Amp w = 158
%12:z=7500  95 Amp w = 610
%13:z=11000 115 Amp w = 188
%15:z=12000 140 Amp w = 147
%29:z=1800  175 Amp  w = 179
%17:z=10000 210 Amp w = 190
```

```
%change duty cycle (70 Amp)
%19:z=9000  15 duty w = 40
%26:z=45000 20 second duty
%27:z=20000 25 second duty

%change duty cycle (175 Amp)
%30:z=19000     20 second duty w = 132
%35:z=57000     30 second duty w = 250
%22:z=1200  single pulse 70
%25:z=2000  single pulse 70
%28:z=4200  single pulse 175

%%%%Constant Current%%%%%%%%%%

%39  amps constant current   38 z = 3900 w = 160 ~ Trial 18 GOOD
%31.3 amps constant current  47 z = w =  ~ Trial 19 GOOD
%96  Amps constant current   43 z = w =  ~ Trial 29 GOOD
%55  amps constant current   45 z = w =  ~ Trial 35 GOOD
%115 amps constant current   46 z = w =  ~ Trial 17 OKAY
%68  amps constant current   44 z = w =  ~ Trial 30 OKAY

%63  amps constant current   39 z = w =
%78  amps constant current   40 z = w =

%68  amps constant current   42 BAD 30
%96  Amps constant current   37  BAD 29

%% create filename
%     string1a = 'I:\data\SDT\SDT_';
    string1b = 'I:\data\PsupCurrent\PsupCurrent_';
    string1c = 'I:\data\Tdat\Tdat_';
    string1d = 'I:\data\Vdat\Vdat_';
    string1e = 'I:\data\SD2\SDo_';
    string1f = 'I:\data\Vtot\Vtot_';

    string1g = 'I:\data\EES\TABLE';
    string1g2 = 'I:\data\EES\TABLE2';

      string2 = num2str(trialNumber);
      string22 = num2str(trialNumber2);

      string3 = '.lvm';

    % Data set 1

    fileb = strcat(string1b,string2,string3);       %current
    filec = strcat(string1c,string2,string3);       %Tdat
    filed = strcat(string1d,string2,string3);       %Vdat
    filee = strcat(string1e,string2,string3);       %Warm end
    filef = strcat(string1f,string2,string3);       %V total

    fileg = strcat(string1g,string3);               %EES data

    % Data set 2
```

```
    fileb2 = strcat(string1b,string22,string3);          %current
    filec2 = strcat(string1c,string22,string3);          %Tdat
    filed2 = strcat(string1d,string22,string3);          %Vdat
    filee2 = strcat(string1e,string22,string3);          %Warm end
    filef2 = strcat(string1f,string22,string3);          %V total

     fileg2 = strcat(string1g2,string3);                %EES data

   % read data from text file
    %data set 1
    %     Ta = dlmread(filea,'\t');
    Tb = dlmread(fileb,'\t');            %current
    Tc = dlmread(filec,'\t');            %Tdat
    Td = dlmread(filed,'\t');            %Vdat
    Te = dlmread(filee,'\t');            %Warm end
    Tf = dlmread(filef,'\t');            %V total

    Tg = dlmread(fileg,'\t');            %EES data

    %data set 2
    %     Ta = dlmread(filea,'\t');
    Tb2 = dlmread(fileb2,'\t');            %current
    Tc2 = dlmread(filec2,'\t');            %Tdat
    Td2 = dlmread(filed2,'\t');            %Vdat
    Te2 = dlmread(filee2,'\t');            %Warm end
    Tf2 = dlmread(filef2,'\t');            %V total

     Tg2 =Tg
     %dlmread(fileg2,'\t');            %EES data
%% %%%%%%%%%%%%%%%%%%%%%%%%%%%%%%%%%%%%%%%%%%%%%%%%%%%%%%%%%%%%%%%%%%%%%%%%%%%
%%%%%%%%%%%%%%%%%%%%%%%%  Data Analysis Figures  %%%%%%%%%%%%%%%%%%%%%%%%%%%%
%%%%%%%%%%%%%%%%%%%%%%%%%%%%%%%%%%%%%%%%%%%%%%%%%%%%%%%%%%%%%%%%%%%%%%%%%%%

%% Warm end Temp
%Plot 1.1     T_warm - model vs data | Pulsed
    figure(1)
    x = Te(1:z,1);
    y = Te(w:v,2);
    x2 = Tg(1:z2,1);
    y2 = Tg(1:z2,65);
    plot(x,y,x2,y2,':r','linewidth',1.6)

    % label plot
    xlabel('Time [s]')
    ylabel('Temperature [K]')
   % title(strcat('Silicone Diode Amb Temperature',{' '},stringTrial(j)))
    % title(strcat('Silicone Diode Amb Temperature',{' '}))

%Plot 1.2     T_warm - model vs data | RMS
    figure(2)
    x = Te2(1:z2,1);
    y = Te2(w2:v2,2);
    x2 = Tg2(1:z2,1);
    y2 = Tg2(1:z2,65);
```

```
    plot(x,y,x2,y2,'linewidth',1.6)

    % label plot
    xlabel('Time [s]')
    ylabel('Temperature [K]')
   % title(strcat('Silicone Diode Amb Temperature',{' '},stringTrial(j)))
        title(strcat('Silicone Diode Amb Temperature',{' '}))


    figure(3)
    x = Te(1:z,1);
    y = Te(w:v,2);
    x2 = Tg(1:z2,1);
    y2 = Tg(1:z2,65);
    x3 = Te2(1:z2,1);
    y3 = Te2(w2:v2,2);
    x4 = Tg2(1:z2,1);
    y4 = Tg2(1:z2,65);
    plot(x,y,x2,y2,'--',x3,y3,'g',x4,y4,'--r','linewidth',1.6)
    xlabel('Time [s]')
    ylabel('Temperature [K]')

  %Plot 1.3     T_warm - data pulsed vs data RMS
%     figure(3)
%     x = Te(1:z,1);
%     y = Te(w:v,2);
%     x2 = Te2(1:z,1);
%     y2 = Te2(w2:v2,2);
%     plot(x,y,x2,y2)
%
%     % label plot
%     xlabel('Time [s]')
%     ylabel('Temperature [K]')
%    % title(strcat('Silicone Diode Amb Temperature',{' '},stringTrial(j)))
%         title(strcat('Silicone Diode Amb Temperature',{' '}))

  %% Total Voltagge

%Plot 2.1     V_tot - model vs data | Pulsed
    figure(4)
    x = Tf(1:z,1);
    y = Tf(w:v,2);
    x2 = Tg(1:z2,1);
    y2 = Tg(1:z2,197);

    plot(x,y,x2,y2,'--r.','linewidth',1.6)

    % label plot
    xlabel('Time [s]')
    ylabel('Voltage [V]')
    %title(strcat('Total Lead Voltage',{' '},stringTrial(j)))

%Plot 2.2     V_tot - model vs data | Constant
    figure(5)
    x = Tf2(1:z2,1);
```

```
    y = Tf2(w2:v2,2);
    x2 = Tg2(1:z2,1);
    y2 = Tg2(1:z2,192);

    plot(x,y,x2,y2,'linewidth',1.6)

    % label plot
    xlabel('Time [s]')
    ylabel('Voltage [V]')
    %title(strcat('Total Lead Voltage',{' '},stringTrial(j)))

    %Plot 2.3     V_tot - pulsed data  vs RMS data | Constant
%     figure(6)
%     x = Tf(1:z,1);
%     y = Tf(w:v,2);
%     x2 = Tf2(1:z2,1);
%     y2 = Tf2(w2:v2,2);
%
%     plot(x,y,x2,y2)
%
%     % label plot
%     xlabel('Time [s]')
%     ylabel('Voltage [V]')
    %title(strcat('Total Lead Voltage',{' '},stringTrial(j)))
%%
%figure(3.1)    Lead temp distribution exp vs model
    figure(7)
    pos = 0:(.75/29):.75;

    plot(TempMm(1:6),Tc(1,2:7),'-*',TempMm(7:12),Tc(1,8:13),'-
o',pos(1:30),Tg(1,65:94),'--','linewidth',1.6)

    % label plot
    xlabel('Position [in]')
    ylabel('Thermal Couple Temperature [K]')
    %title(strcat('Lead Temp vs Position',{' '},stringTrial(j)))

    %Do same for set 2 then compare set 1 and 2
%%
%figure(4.1)
     figure(8)


    [~,col] = size(Tc);
    for i = 6
        plot(Tc(1:z2,1),Tc(w2:v2,i),'linewidth',1.8)
        hold on
    end
    for i = [86];
        plot(Tc(1:z2,1),Tg(1:z2,i),':','linewidth',1.8)
        hold on
    end
    %,Tg(1:z,1),Tg(1:z,j)
    xlabel('Time [s]')
    ylabel('Temperature [K]')
```

```
    %title(strcat('Thermocouple Temperature',{' '},stringTrial(j)))

         figure(9)


    [~,col] = size(Tc2);
    for i = 2:7
        plot(Tc2(1:z2,1),Tc2(w2:v2,i),'linewidth',1.8);
        hold on
    end
    for i = [94,92,90,88,86,84];
        plot(Tc2(1:z2,1),Tg2(1:z2,i),':','linewidth',1.6)
        hold on
    end
    %,Tg(1:z,1),Tg(1:z,j)
    xlabel('Time [s]')
    ylabel('Temperature [K]')
    %title(strcat('Thermocouple Temperature',{' '},stringTrial(j)))

    %DO SAME FOR SET 2 and then compare set 1 to 2

%%

         figure(10)

     x = Tb(1:z,1);
     y = Tb(w:v,2);
     % EES model
     x2 = Tg(1:z2,1);
     y2 = Tg(1:z2,4);
     plot(x,y,x2,y2,'--r.','linewidth',1.6)

     % label plot
     xlabel('Time [s]')
     ylabel('Current [A]')
%     title(strcat('Power Supply Current',{' '},stringTrial(j)))
%
         figure(11)

     x = Tb2(1:z2,1);
     y = Tb2(w2:v2,2);
     % EES model
     x2 = Tg2(1:z2,1);
     y2 = Tg2(1:z2,4);
     plot(x,y,x2,y2,'--r.','linewidth',1.6)

     % label plot
     xlabel('Time [s]')
     ylabel('Current [A]')
%     title(strcat('Power Supply Current',{' '},stringTrial(j)))

%%
     figure(12)
     [~,col] = size(Td);
     for i = 2:7
```

```
        plot(Td(1:z,1),Td(w:v,i)-.0017,Td(1:z,1),Tg(1:z,191-
i),':','linewidth',1.2)

        hold on
    end

    xlabel('Time [s]')
    ylabel('Voltage [V]')
%     title(strcat('Current lead Voltage',{' '},stringTrial(j)))

   figure(13)
    [~,col] = size(Td2);
    for i = 2:col
        plot(Td2(1:z2,1),Td2(w2:v2,i)-.0087,Td2(1:z2,1),Tg2(1:z2,191-
i),':','linewidth',1.2)

        hold on
    end

    xlabel('Time [s]')
    ylabel('Voltage [V]')
%     title(strcat('Current lead Voltage',{' '},stringTrial(j)))


figure(14)
    pos = 0:(.75/29):.75;

    plot(TempMm(1:6),Tc(1,2:7),'-*',TempMm(7:12),Tc(1,8:13),'-
o',pos(1:30),Tg(1,65:94),'--','linewidth',1.6)

    % label plot
    xlabel('Position [in]')
    ylabel('Thermal Couple Temperature [K]')

    figure(15)
        pos = 0:(.75/29):.75;

    plot(TempMm(1:6),Tc(1,2:7),'-*',pos(1:30),Tg(1,65:94),'--
',TempMm(1:6),Tc(590,2:7),'-*',pos(1:30),Tg(400,65:94),'--
',TempMm(1:6),Tc(990,2:7),'-*',pos(1:30),Tg(800,65:94),'--
',TempMm(1:6),Tc(1290,2:7),'-*',pos(1:30),Tg(1000,65:94),'--
','linewidth',1.6)

    % label plot
    xlabel('Position [in]')
    ylabel('Thermal Couple Temperature [K]')

    figure(16)
        pos = 0:(.75/29):.75;

   plot(TempMm(1:6),Tc(1,2:7),'-*',pos(1:30),Tg(1,65:94),'--
',TempMm(1:6),Tc(4000,2:7),'-*',pos(1:30),Tg(4000,65:94),'--
',pos(1:30),Tg(12000,65:94),'--',pos(1:30),Tg(12000,65:94),'--
','linewidth',1.6)
```

```
    % label plot
    xlabel('Position [in]')
    ylabel('Thermal Couple Temperature [K]')

     figure(17)

    pos = 0:(.75/29):.75;

    plot(TempMm(1:6),Tc(1,2:7),'-*',TempMm(7:12),Tc(1,8:13),'-
o',pos(1:30),Tg(1,65:94),'--','linewidth',1.6)

    % label plot
    xlabel('Position [in]')
    ylabel('Thermal Couple Temperature [K]')

     figure(18)
pos = 0:(.75/29):.75;
contour(pos(1:30),Tg(65:94),Tg(1:100,65:94))
```

Labview diagram and panel 1 and 2

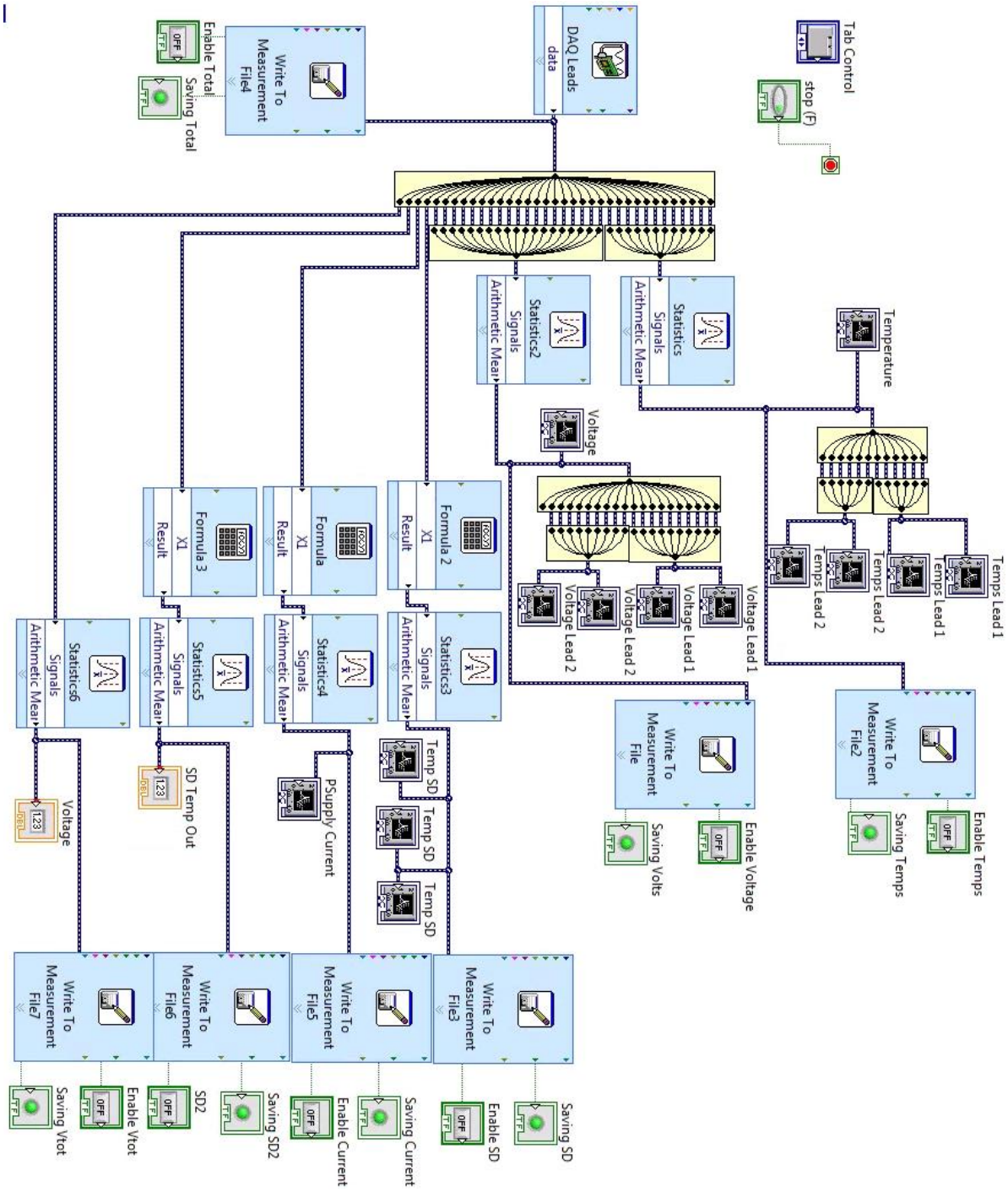

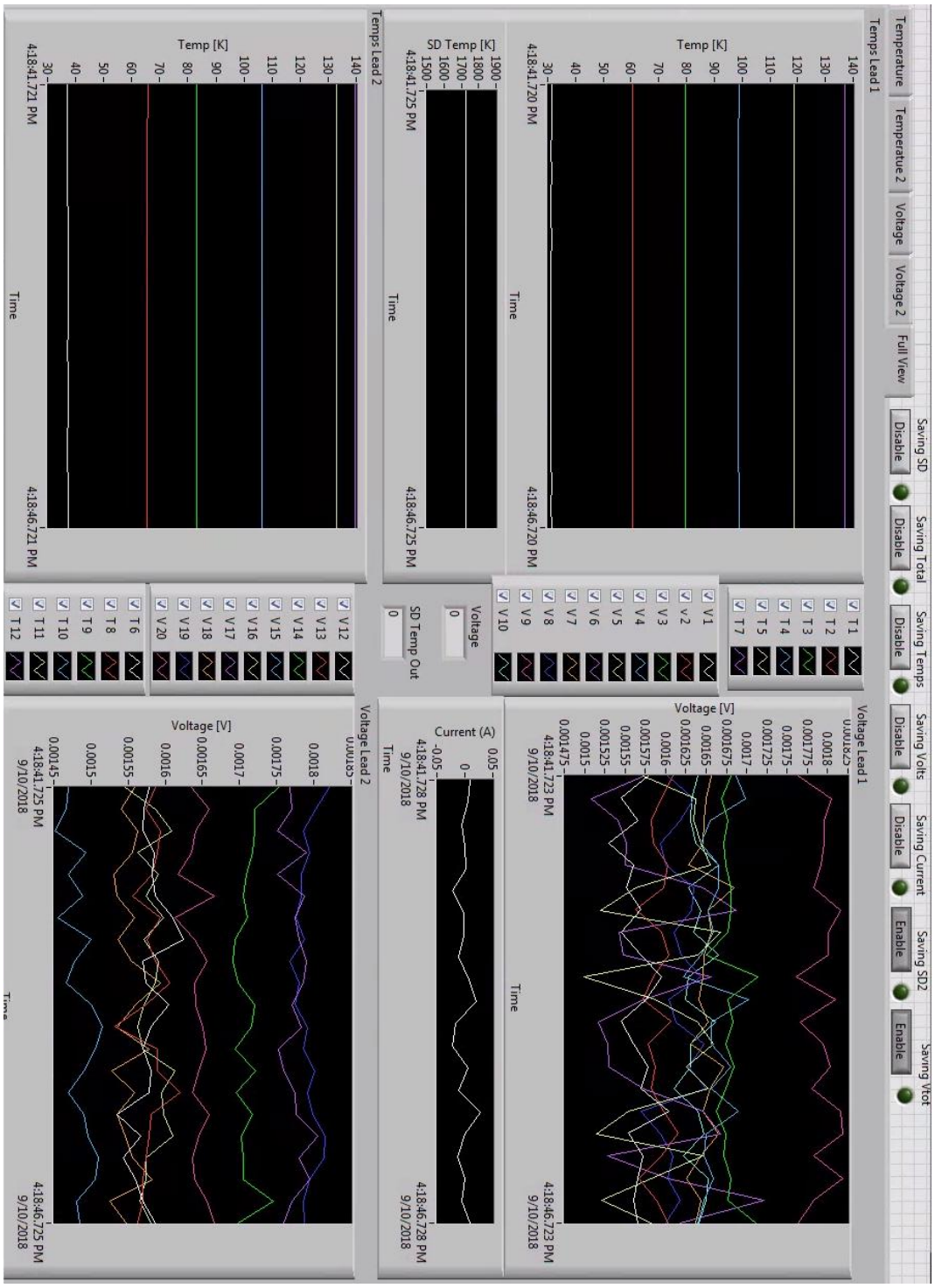
Temperature
Temperatue 2
Voltage
Voltage 2
Full View
Saving SD
Disable
Saving Total
Disable
Saving Temps
Disable
Saving Volts
Disable
Saving Current
Disable
Saving SD2
Enable
Saving Vtot
Enable
Temps Lead 1
Temp [K]
Time
4:18:41.720 PM
4:18:46.720 PM
T1
T2
T3
T4
T5
T7
V1
v 2
V3
V4
V5
V6
V7
V8
V9
V10
Voltage Lead 1
Voltage [V]
4:18:41.723 PM
4:18:46.723 PM
9/10/2018
Temps Lead 2
SD Temp [K]
4:18:41.725 PM
4:18:46.725 PM
Voltage
SD Temp Out
V12
V13
V14
V15
V16
V17
V18
V19
V20
T6
T8
T9
T10
T11
T12
Current (A)
4:18:41.728 PM
4:18:46.728 PM
Voltage Lead 2
4:18:41.725 PM
4:18:46.725 PM

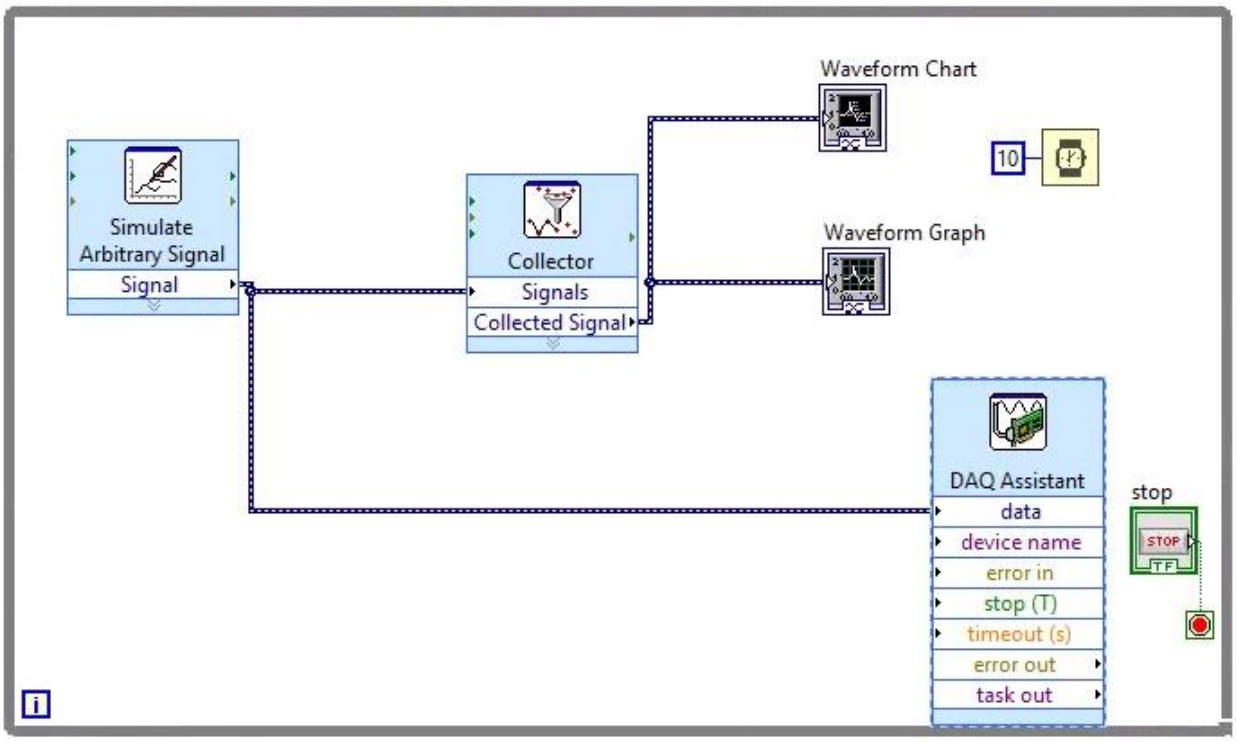
Waveform Chart
10
Simulate
Arbitrary Signal
Signal
Collector
Signals
Collected Signal
Waveform Graph
DAQ Assistant
data
device name
error in
stop (T)
timeout (s)
error out
task out
stop
STOP
TF